Precision Calculations in New Physics Models

Zur Erlangung des akademischen Grades eines

DOKTORS DER NATURWISSENSCHAFTEN

von der KIT-Fakultät für Physik des

Karlsruher Instituts für Technologie (KIT)

genehmigte

DISSERTATION

von

M.Sc. Alexander Wlotzka

aus Karlsruhe

Tag der mündlichen Prüfung: 19. Mai 2017

Referentin: Prof. Dr. Margarete Mühlleitner

Korreferent: PD Dr. Stefan Gieseke

Abstract

Even after the discovery of a Higgs boson fundamental questions of particle physics remain unanswered. Neither the origin of the baryon-antibaryon asymmetry of the universe, nor the nature of Dark Matter is understood. Two models of New Physics capable of addressing these problems are investigated here. In the first part of the thesis branching ratios for the decays of the lightest up-type squark in the Minimal Supersymmetric Extension of the Standard Model (MSSM) are calculated to high precision for scenarios with compressed supersymmetric spectra by including the finite width of the W boson. These branching ratios affect the limits on the model which can be set by experiments. The second part concentrates on predictions of cross sections for squark gluino production in the MSSM. Spin correlations between the production and the decay of the gluino as well as next-to-leading order corrections are taken into account and a framework consistently treating both the production and the decay of the squark and the gluino in an event generator is elaborated. First results show that the impact of spin correlations on differential cross sections is considerable. In the last part the electroweak phase transition is investigated in the Two-Higgs-Doublet Model by analyzing the loop-corrected effective potential at finite temperature. Based on the development of a new renormalization prescription an effective scan over the parameter space of the model is performed. The results show that demanding a strong first order phase transition, as required for baryogenesis, leads to strong constraints on collider observables.

Zusammenfassung

Selbst nach der Entdeckung eines Higgsbosons bleiben fundamentale Fragen der Teilchenphysik unbeantwortet. Weder der Ursprung der Baryon-Antibaryonasymmetrie des Universums, noch die Natur Dunkler Materie sind verstanden. Zwei Modelle Neuer Physik, welche diese Probleme behandeln können, werden hier untersucht. Im ersten Teil der Doktorarbeit werden Verzweigungsverhältnisse des leichtesten Up-Type Squarks in der Minimalen Supersymmetrischen Erweiterung des Standardmodells (MSSM) für Szenarien mit komprimiertem Teilchenspektrum verbessert, indem die endliche Breite des W-Bosons berücksichtigt wird. Diese Verzweigungsverhältnisse beeinflussen die Beschränkungen des Modells, welche durch Experimente auferlegt werden können. Der zweite Teil konzentriert sich auf Vorhersagen von Wirkungsquerschnitten für die Squark-Gluino-Produktion im MSSM. Spinkorrelationen zwischen Produktion und Zerfall des Gluinos, ebenso wie Korrekturen höherer Ordnung werden berücksichtigt, und ein Programm, in welchem Produktion und Zerfall des Squarks und des Gluinos konsistent in einem Ereignisgenerator beschrieben werden können, wird entwickelt. Erste Ergebnisse zeigen einen beachtlichen Einfluss der Spinkorrelationen auf differentielle Wirkungsquerschnitte. Im letzten Teil wird der elektroschwache Phasenübergang im Zwei-Higgs-Doublett Modell untersucht, indem das schleifenkorrigierte effektive Potential bei endlicher Temperatur analysiert wird. Basierend auf der Entwicklung eines neuen Renormierungsschemas, wird ein effektiver Scan über den Parameterraum des Modells ausgeführt. Die Ergebnisse zeigen, dass die Forderung nach einem Phasenübergang stark erster Ordnung, wie er für Baryogenese notwendig ist, zu wichtigen Einschränkungen von Observablen an Teilchenbeschleunigern führt.

Contents

1. Introduction

Seht Ihr den Mond dort stehen?
Er ist nur halb zu sehen,
Und ist doch rund und schön!
So sind wohl manche Sachen,
Die wir getrost belachen,
Weil uns're Augen sie nicht seh'n.

Matthias Claudius, Abendlied, 1779

The discovery of a Higgs boson [1, 2] by the experiments ATLAS and CMS in 2012 is a major achievement of high energy physics. The determination of the mass of the Higgs boson fixed the last free parameter of the Standard Model (SM) of particle physics, which can now be regarded as a complete, self-contained model describing elementary particles and their interactions at the energy scale of current particle accelerators. However, at the same time the SM is not able to solve significant problems: it has been measured that only a small fraction of the energy of the universe exists as ordinary matter [3]. A much larger portion consists of Dark Matter (DM), whose nature is hitherto unknown. Another open question is the origin of the baryon-antibaryon asymmetry of the universe (BAU) [4]. The SM can neither provide a viable candidate for DM, nor explain the BAU, and as a consequence both observations call for physics beyond the SM (BSM). In conclusion it is quite possible, that only a small part of the whole has been observed so far and there may be much more to discover.

In order to investigate solutions to these and other open questions and to distinguish possible extensions of the SM, predictions for observables have to be derived in the new models, which can be tested by experiments. This work focuses on two such extensions: the Minimal Supersymmetric Standard Model (MSSM) [5–11] and the Two-Higgs-Doublet Model (2HDM) [12–14].
Supersymmetry (SUSY) is an intensely studied extension of the SM. In supersymmetric theories, a symmetry relating fermions and bosons to each other is introduced. By this symmetry all SM particles acquire superpartners sharing the same gauge quantum numbers and mass but with a different spin. In addition, the Higgs sector is extended and features new

Higgs bosons. Since no superpartner has been observed so far, SUSY must be broken, which allows for the masses of SUSY particles to be different from the mass of their SM equivalents.

The top-quark receives two scalar superpartners, one for the left- and one for the right-chiral component, called left- and right-handed stop $\tilde{t}_L$ and $\tilde{t}_R$. As they share identical gauge quantum numbers the two stops can mix and form a light mass eigenstate called $\tilde{t}_1$ and a heavy one called $\tilde{t}_2$. A large mixing is of particular interest in the MSSM, since it can lift the mass of the light CP-even Higgs boson, whose upper bound at tree-level is given by the mass of the Z boson, to the value observed by experiments through radiative corrections. Due to the large mixing the light stop can be light enough to be copiously produced at the Large Hadron Collider (LHC) at the European Organization for Nuclear Research (CERN), although other SUSY particles can be heavy. Accordingly, important searches of ATLAS and CMS focus on a light stop and require predictions for different decay channels and their branching ratios (BR). Assuming conservation of the so-called R-parity, which is a multiplicative quantum number with value -1 for all superpartners and value $+1$ for all SM particles, the lightest supersymmetric particle (LSP) is stable. In this work, the lightest neutralino $\tilde{\chi}_1^0$, which is a mixture of the superpartners of the photon, the Z boson and neutral Higgs bosons, is chosen to be the LSP, forming an ideal candidate for DM, and the light stop is the next-to-lightest supersymmetric particle (NLSP). Hence, the mass difference between the light stop and the lightest neutralino determines which decay channels of the light stop are kinematically open. In previous works [15–17], it has been shown that if the mass difference is smaller than the mass of the top-quark, flavor-changing neutral current decays can become important, which are possible at tree-level, if in addition to the left-right mixing also mixing between different generations of up-type squarks is allowed. In this case, the stops also mix with the superpartners of the up- and charm-quarks and the lightest up-type squark mass eigenstate is then denoted by $\tilde{u}_1$. The $\tilde{u}_1$, which is then chosen as NLSP, is dominated by the light stop due to the large mixing, but has small up and charm flavor admixtures. If the mass difference of this lightest up-type squark to the LSP is lower than the mass of the W boson, either a two-body decay into a charm-quark and the neutralino can take place, or a four-body decay into a down-type quark, the lightest neutralino and two SM fermions stemming from an off-shell W-decay. On the other hand, if the phase space available in the decay of the lightest up-type squark allows for an on-shell W boson, the four-body decay turns into a three-body decay, where the W boson is on-shell. This transition region together with the general flavor mixing is not covered by previous calculations [18–20]. The first part of this work focuses on a consistent description of the threshold region, including the general flavor mixing of the lightest up-type squark and finite width effects for the W boson [21].

In order to interpret observed limits on cross sections measured at the LHC in terms of the MSSM and to derive exclusion bounds on the parameters of the model, in addition to the BRs also predictions for the production cross sections of SUSY particles are necessary. The second part of this work focuses on the production of a squark $\tilde{q}$ and a gluino $\tilde{g}$, where the squark is one of the superpartners of quarks of the first two generations, and the gluino is the superpartner of the gluon. The lifetimes of both squarks and gluinos are usually very small, such that the decays of the particles are important for computing differential cross sections. Since the gluino is a spin half particle and decays before it hadronizes in the scenarios considered here, the spin information is transferred to the decay products, which are a quark and a squark of same flavor. These spin correlations affect distributions of kinematic observables. Differential distributions for squark gluino production combining next-to-leading order (NLO) corrections, the decays of the particles and the spin correlations have not been given in the literature so far [22–33]. This is taken up here and a framework

where spin correlations and NLO corrections are combined is elaborated. An important step in this context is the calculation of the real corrections to the squark gluino production which feature on-shell singularities that have to be cured in a gauge-invariant way [34, 35]. For instance the radiation of a massless quark from the squark gluino production can also be regarded as squark pair production with the subsequent decay of one of the squarks. This contribution is already covered by the explicit calculation of squark pair production and hence has to be subtracted from the cross section for squark gluino production in order to avoid double counting. To this end, a calculation of the amplitudes squared for the real corrections to squark gluino production including the spin dependence is performed by hand. This is a necessary ingredient for the gauge-invariant subtraction of the on-shell singularities. The framework comprising the production and the decays including spin correlations together with the NLO corrections to squark gluino production is then implemented in the event generator `POWHEG − BOX` [36–38].

A well-studied approach to explain the BAU is Electroweak Baryogenesis (EWBG), based on the baryon number non-conservation by anomalies at high temperatures [39–41] in the breakdown from the $SU(2)_L \times U(1)_Y$ to the $U(1)_{em}$ in the early universe. In EWBG the three Sakharov criteria for baryogenesis [42] can be fulfilled by a departure from the thermal equilibrium in the transition from the unbroken to the broken phase of the electroweak symmetry and by sphaleron [43] transitions in presence of C- and CP-violating interactions. Although these conditions are met by the SM in principle, EWBG is still not possible: for successful EWBG the phase transition additionally has to be of strong first order [41]. This requirement results in an upper bound on the Higgs mass in the SM m_h of about [44–46]

$$m_h \lesssim 70 \text{ GeV} . \tag{1.1}$$

This bound is obviously violated by the measured value of 125.09 GeV [47]. Moreover, the amount of CP violation induced by the Cabibbo-Kobayashi-Maskawa (CKM) matrix [48, 49] is not sufficient to lead to the observed BAU [50–52]. Hence, in terms of EWBG, the BAU necessitates New Physics.
In the MSSM, it has been shown that EWBG is possible, if the SUSY spectrum provides a light stop with a mass [53]

$$m_{\tilde{t}_1} \lesssim 120 \text{ GeV} . \tag{1.2}$$

By now, this possibility is excluded by the direct searches for a stop by ATLAS [54]. In consequence, a different extension of the SM is investigated with respect to the electroweak phase transition (EWPT) in this work: the 2HDM. In the 2HDM the Higgs sector of the SM is extended by a second Higgs doublet[1], leading to five Higgs bosons instead of only one. The upper bound Eq. (1.1) does not hold in this case. Additionally, the Higgs potential allows for new sources of CP violation and thereby addresses both shortcomings of the SM. Regarding the Higgs sector, the 2HDM offers more flexibility than the MSSM since the quartic couplings of the Higgs potential are not governed by gauge couplings, but are independent input parameters.

In Ch. 2 basic concepts required for the three topics are introduced. After that, the W boson threshold in the decay of the lightest up-type squark is investigated in Ch. 3. The subsequent Ch. 4 focuses on the squark gluino production with spin correlations at NLO, before the EWPT is studied in Ch. 5. The findings are summarized in the conclusion in Ch. 6.

[1] In contrast to the MSSM, in the 2HDM both Higgs doublets carry the same hypercharge.

2. Prerequisites

In this chapter principles of SUSY, the field content and examples for experimental exclusion bounds are presented in Sec. 2.1. In Sec. 2.2 the foundations of the NLO calculation performed at fixed order are presented, before closing with explanations regarding the EWPT in Sec. 2.3.

2.1. Supersymmetry

Profound introductions to SUSY are given for instance in [55, 56]. In this section only major aspects are discussed.

2.1.1. General Features

Similar to the SM, the beauty of SUSY is the guiding principle of symmetries. According to the Coleman-Mandula no-go theorem [57] the Poincaré symmetry of the $\mathcal{S}$ matrix cannot be combined with any other continuous symmetry of the $\mathcal{S}$ matrix in a non-trivial way. Hence, the maximum symmetry group is given by the direct product of the Poincaré group with the symmetry group defining internal symmetries. However, the theorem does not cover the possibility of a fermionic generator Q in the $(\frac{1}{2}, 0)$ representation of the Lorentz group and its hermitian conjugate $\bar{Q}$ in the $(0, \frac{1}{2})$ representation enhancing the space-time symmetry. As stated in the Haag-Łopuszański-Sohnius theorem [58] the most general form of incorporating the spinorial generators Q and $\bar{Q}$ consistent with the assumptions of the Coleman-Mandula theorem is given by extending the Poincaré algebra to the Super-Poincaré algebra defined by the additional (anti-)commutators [55]

$$\{Q_A, \bar{Q}_{\dot{B}}\} = 2\sigma^{\mu}_{A\dot{B}} P_\mu \ , \qquad \{\bar{Q}^{\dot{A}}, Q^B\} = 2\bar{\sigma}^{\mu\dot{A}B} P_\mu \ , \tag{2.1}$$

$$\{Q_A, Q_B\} = 0 \ , \qquad \{\bar{Q}^{\dot{A}}, \bar{Q}^{\dot{B}}\} = 0 \ , \tag{2.2}$$

$$[Q_A, P^\mu] = 0 \ , \qquad [\bar{Q}^{\dot{A}}, P^\mu] = 0 \ , \tag{2.3}$$

$$[M_{\mu\nu}, Q_A] = -(\sigma_{\mu\nu})_A{}^B Q_B \ , \qquad [M_{\mu\nu}, \bar{Q}^{\dot{A}}] = -(\bar{\sigma}_{\mu\nu})^{\dot{A}}{}_{\dot{B}} \bar{Q}^{\dot{B}} \ , \tag{2.4}$$

where P^μ are the generators of translations and $M^{\mu\nu}$ the generators of Lorentz transformations, and the spinorial generators are understood to be in the Weyl representation with

spinor indices A and B. In these relations we used

$$\sigma^\mu = (\mathbb{1}_2, \vec{\sigma}) \ , \tag{2.5}$$

$$\bar{\sigma}^\mu = (\mathbb{1}_2, -\vec{\sigma}) \ , \tag{2.6}$$

$$\sigma^{\mu\nu} = \frac{\mathrm{i}}{4} \left(\sigma^\mu \bar{\sigma}^\nu - \sigma^\nu \bar{\sigma}^\mu\right) \ , \tag{2.7}$$

$$\bar{\sigma}^{\mu\nu} = \frac{\mathrm{i}}{4} \left(\bar{\sigma}^\mu \sigma^\nu - \bar{\sigma}^\nu \sigma^\mu\right) \ , \tag{2.8}$$

where $\mathbb{1}_2$ denotes the 2×2 identity matrix and $\vec{\sigma}$ is the vector of 2×2 Pauli matrices. For a detailed introduction to the Weyl component notation with dotted and undotted spinor indices we refer to [55, 59]. Introducing only one set of fermionic generators is referred to as $N = 1$ SUSY. The fermionic operator defines a transformation between bosons and fermions schematically given by

$$Q\,|\text{boson}\rangle = |\text{fermion}\rangle \quad \text{and} \quad Q\,|\text{fermion}\rangle = |\text{boson}\rangle \ . \tag{2.9}$$

This transformation relates every boson of the SM to a fermionic superpartner and every fermion of the SM to a bosonic superpartner, which are both part of irreducible representations of the SUSY algebra called supermultiplets. Due to Eq. (2.3) P^2 commutes with the generator Q and hence all particles within a supermultiplet have a common mass. Moreover, since the gauge symmetries are untouched, they also share the same gauge quantum numbers with respect to the SM gauge group $SU(3)_C \times SU(2)_L \times U(1)_Y$. This way, a quark q receives two scalar superpartners $\tilde{q}_L$ and $\tilde{q}_R$ called left- and right-handed squarks. The subscripts L and R and the corresponding names refer to the chirality of the quark in the supermultiplet. Similarly, each lepton l obtains two scalar superpartners $\tilde{l}_L$ and $\tilde{l}_R$ called sleptons, and gauge bosons acquire fermionic superpartners, called gauginos. In order to give mass to both up- and down-type fermions in SUSY theories the Higgs sector has to be furnished with two $SU(2)$ Higgs doublets, $H_u = (H_u^+, H_u^0)$ with hypercharge $Y = +1/2$ and $H_d = (H_d^0, H_d^-)$ with hypercharge $Y = -1/2$. These scalar Higgs fields get fermionic superpartners $\tilde{H}_u^+, \tilde{H}_u^0, \tilde{H}_d^0$ and $\tilde{H}_d^-$ called higgsinos. Left- and right-handed fermions of the SM together with their scalar superpartners, as well as the Higgs bosons with their fermionic superpartners form chiral superfields summarized in Tab. 2.1, the gauge bosons of the SM with their fermionic superpartners form gauge superfields collected in Tab. 2.2. In each superfield, the number of bosonic degrees of freedom is equal to the number of fermionic ones. Denoting the baryon number of particles by B, the lepton number by L and the spin by S the R-parity mentioned in Ch. 1 is defined as

$$R = (-1)^{3B-L+2S} \ . \tag{2.10}$$

For all SM particles holds $R = +1$, whereas for all SUSY particles $R = -1$. Requiring R-parity conservation in a model implies that in a decay of a SUSY particle there must be an odd number of SUSY particles in the final state, enforcing stability of the lightest SUSY particle. Furthermore, in a production process starting with SM particles, SUSY particles are always produced in even numbers. Using the notation of [60], in terms of the superfields the superpotential of the MSSM W_{MSSM} with conserved R-parity is given by [55, 56]

$$W_{\text{MSSM}} = \epsilon_{ab} \left[(Y_E)_{ij} \hat{H}_d^a \hat{L}_i^b \hat{E}_j^c + (Y_D)_{ij} \hat{H}_d^a \hat{Q}_i^b \hat{D}_j^c + (Y_U)_{ij} \hat{H}_u^b \hat{Q}_i^a \hat{U}_j^c - \mu \hat{H}_d^a \hat{H}_u^b\right] \ , \tag{2.11}$$

where ϵ_{ab} is the totally antisymmetric tensor with $\epsilon_{12} = \epsilon^{12} = 1$, $(Y_{E,D,U})_{ij}$ are the components i, j of 3×3 Yukawa matrices in generation space for (s)leptons, down-type (s)quarks and up-type (s)quarks, respectively, and μ is the higgsino mass parameter[2].

[2] A discussion of the μ-problem can be found for instance in [55].

Superfield	Spin 0	Spin 1/2	$SU(3)_C \times SU(2)_L \times U(1)_Y$
$\hat{Q}$	$\tilde{Q} = (\tilde{u}_L, \tilde{d}_L)$	(u_L, d_L)	$(3, 2, 1/6)$
$\hat{U}^c$	$\tilde{u}_R^*$	$u_R^\dagger$	$(\bar{3}, 1, -2/3)$
$\hat{D}^c$	$\tilde{d}_R^*$	$d_R^\dagger$	$(\bar{3}, 1, 1/3)$
$\hat{L}$	$\tilde{L} = (\tilde{\nu}_L, \tilde{e}_L)$	(ν_L, e_L)	$(1, 2, -1/2)$
$\hat{E}^c$	$\tilde{e}_R^*$	$e_R^\dagger$	$(1, 1, 1)$
$\hat{H}_u$	$H_u = (H_u^+, H_u^0)$	$(\tilde{H}_u^+, \tilde{H}_u^0)$	$(1, 2, 1/2)$
$\hat{H}_d$	$H_d = (H_d^0, H_d^-)$	$(\tilde{H}_d^0, \tilde{H}_d^-)$	$(1, 2, -1/2)$

Table 2.1: Chiral superfields and their elementary particles together with the representation/charge with respect to the gauge group [55, 56] in the notation of [60]. The properties shown hold for all three generations and the superscript c denotes charge conjugation.

Superfield	Spin 1/2	Spin 1	$SU(3)_C \times SU(2)_L \times U(1)_Y$
$\hat{W}$	$\tilde{W}_i$	W_i	$(1, 3, 0)$
$\hat{B}$	$\tilde{B}$	B	$(1, 1, 0)$
$\hat{G}$	$\tilde{g}_f$	g_f	$(8, 1, 0)$

Table 2.2: Gauge superfields and their elementary particles together with the representation/charge with respect to the gauge group [55, 56] in the notation of [60]. The index i ranges from 1 to 3 and $f = 1...8$.

As argued above, in conserved SUSY the masses of the superpartners are the same as the masses of the SM particles. Up to now, no superpartner has been observed and in conclusion SUSY must be broken. Irrespective of any breaking mechanism, the breaking can be parametrized by soft SUSY-breaking terms, which break SUSY explicitly and are either pure mass terms or interactions with dimensionful couplings. Summing over repeated indices with $a, b = 1, 2$, $i, j = 1...3$ and $f = 1...8$ they are given by [55, 56, 60]

$$\begin{aligned}
\mathcal{L}_{\text{soft}} = &- m_{H_d}^2 H_{d\,a}^* H_d^a - m_{H_u}^2 H_{u a}^* H_u^a - \tilde{Q}_{ia}^* (m_{\tilde{Q}}^2)_{ij} \tilde{Q}_j^a - \tilde{L}_{ia}^* (m_{\tilde{L}}^2)_{ij} \tilde{L}_j^a \\
&- \tilde{u}_{iR} (m_{\tilde{U}}^2)_{ij} \tilde{u}_{jR}^* - \tilde{d}_{iR} (m_{\tilde{D}}^2)_{ij} \tilde{d}_{jR}^* - \tilde{e}_{iR} (m_{\tilde{E}}^2)_{ij} \tilde{e}_{jR}^* \\
&- \frac{1}{2} \left(M_1 \tilde{B}\tilde{B} + M_2 \tilde{W}_i \tilde{W}_i + M_3 \tilde{g}_f \tilde{g}_f + \text{h.c.} \right) \\
&+ \epsilon_{ab} \Big(m_3^2 H_d^a H_u^b - (T_E)_{ij} H_d^a \tilde{L}_i^b \tilde{e}_{jR}^* \\
&\qquad - (T_D)_{ij} H_d^a \tilde{Q}_i^b \tilde{d}_{jR}^* - (T_U)_{ij} H_u^b \tilde{Q}_i^a \tilde{u}_{jR}^* + \text{h.c.} \Big) \ ,
\end{aligned} \tag{2.12}$$

with the soft SUSY-breaking masses $m_{H_d}^2$, $m_{H_u}^2$, M_1, M_2, M_3 and m_3^2, the soft SUSY-breaking mass matrices in generation space $m_{\tilde{Q}}^2$, $m_{\tilde{L}}^2$, $m_{\tilde{U}}^2$, $m_{\tilde{D}}^2$, $m_{\tilde{E}}^2$, and trilinear coupling matrices T_E, T_D and T_U defined by

$$(T_P)_{ij} = (Y_P)_{ij} (A_P)_{ij} \ , \quad P = E, D, U \ , \tag{2.13}$$

for each element i, j (no sum over the indices). The matrices A_P are soft SUSY-breaking trilinear coupling matrices in generation space. The soft SUSY-breaking parameters can be

defined as inputs at the weak scale, or they can be derived by renormalization group equation (RGE) running from a high scale down to the weak scale under the assumption of a certain mechanism to transfer the breaking of SUSY in the hidden sector to the MSSM fields. In this thesis, the first approach is followed in Ch. 3, whereas in Ch. 4 the mSUGRA [61–67] mechanism is used[3]. In the latter, only five parameters have to be set at the unification scale m_{GUT}. These are a common scalar mass parameter m_0, a common fermion mass parameter $m_{1/2}$, a single trilinear coupling A_0, the sign of μ and $\tan\beta$ which is explained below.
From the two Higgs doublets defined above only five degrees of freedom lead to physical Higgs particles, namely a light and a heavy CP-even Higgs boson h and H, respectively, a CP-odd Higgs boson A and a charged Higgs pair $H^{\pm}$. The three remaining degrees of freedom give mass to the weak gauge bosons as in the SM. At tree-level, the Higgs sector of the MSSM can be specified by only two parameters: $\tan\beta = v_u/v_d$, where $v_{u,d}$ are the vacuum expectation values of the two neutral Higgs fields, and the mass of the pseudoscalar Higgs boson m_A.
The SUSY fields explained above are defined in the gauge basis and can mix to form physical mass eigenstates. Such a mixing defines the neutralino mass eigenstates $\tilde{\chi}_l^0$, $l = 1...4$ as a mixture of the bino $\tilde{B}$, the wino $\tilde{W}_3$ and the two neutral higgsinos $\tilde{H}_u^0$ and $\tilde{H}_d^0$. Similarly, the charged higgsinos $\tilde{H}_u^+$ and $\tilde{H}_d^-$ and the winos $\tilde{W}_1$ and $\tilde{W}_2$ mix and form mass eigenstates $\tilde{\chi}_k^{\pm}$, $k = 1, 2$, called charginos. The mixing in the squark and slepton sector is explained in the following section.

2.1.2. Sfermion Mixing

Similarly to the higgsinos and gauginos, also the sfermions, i.e. squarks and sleptons, can mix. Adopting the notation of [68] the mass terms for up-type and down-type squarks are given by

$$\mathcal{L}_{\tilde{q}} = -\tilde{u}^{\dagger}\mathcal{M}_{\tilde{u}}^2\tilde{u} - \tilde{d}^{\dagger}\mathcal{M}_{\tilde{d}}^2\tilde{d}\ , \tag{2.14}$$

where $\tilde{u} = (\tilde{u}_L, \tilde{c}_L, \tilde{t}_L, \tilde{u}_R, \tilde{c}_R, \tilde{t}_R)^T$ and $\tilde{d} = (\tilde{d}_L, \tilde{s}_L, \tilde{b}_L, \tilde{d}_R, \tilde{s}_R, \tilde{b}_R)^T$ are six-component vectors of left- and right-handed up-type and down-type squarks. Accordingly, the matrices $\mathcal{M}_{\tilde{u}}^2$ and $\mathcal{M}_{\tilde{d}}^2$ are 6×6 mass squared matrices which can be decomposed into four 3×3 blocks

$$\mathcal{M}_{\tilde{u},\tilde{d}}^2 = \begin{pmatrix} \mathcal{M}_{\tilde{u},\tilde{d}LL}^2 & \mathcal{M}_{\tilde{u},\tilde{d}LR}^2 \\ \mathcal{M}_{\tilde{u},\tilde{d}LR}^{2\dagger} & \mathcal{M}_{\tilde{u},\tilde{d}RR}^2 \end{pmatrix}\ . \tag{2.15}$$

The blocks explicitly mix the left- and right-handed components of the vectors $\tilde{u}$ and $\tilde{d}$, respectively, which is indicated by the subscripts LL, RR and LR. As is obvious from Eq. (2.12) flavor mixings can be introduced by flavor-changing entries in the soft SUSY-breaking mass matrices $m_{\tilde{Q}}^2$, $m_{\tilde{U}}^2$, and $m_{\tilde{D}}^2$, and by the trilinear coupling matrices T_U and T_D. In the limit of no flavor violation in the squark sector, the mass matrix only connects left- and right-handed squarks of equal flavors. In this case only the diagonal terms of the soft SUSY-breaking mass matrices and trilinear couplings are present and are denoted by $m_{\tilde{Q}_i}$, $i = 1, 2, 3$, $m_{\tilde{U}_R}$, $U = u, c, t$ and $m_{\tilde{D}_R}$, $D = d, s, b$. In the remaining mixing of left- and right-handed states, usually only the mixing in the third generation is considered, since the strength of the mixing is proportional to the mass of the corresponding SM quark, which is small for the first two generations. The two sbottoms $\tilde{b}_L$ and $\tilde{b}_R$ are mixed to a light mass eigenstate $\tilde{b}_1$ and a heavy mass eigenstate $\tilde{b}_2$ and likewise $\tilde{t}_L$ and $\tilde{t}_R$ form the mass eigenstates $\tilde{t}_1$ and $\tilde{t}_2$. The left- and right-handed states of the first two generations are directly treated as mass eigenstates. This version of sfermion mixing is considered in Ch. 4.

[3] An introduction to mSUGRA is provided in [55].

In case flavor-changing effects are considered as in Ch. 3, flavor off-diagonal elements in the squark mass matrices are not neglected. In this case, the mass matrix is diagonalized by a 6×6 rotation matrix, which incorporates both flavor- and left-right-mixing of the squarks. The resulting mass eigenstates are no longer flavor eigenstates, but a mixture of all three flavors. The mass eigenstates are then denoted by up-type squarks $\tilde{u}_i$, $i = 1...6$ and down-type squarks $\tilde{d}_i$, $i = 1...6$, which are ordered in mass, with $\tilde{u}_1$ and $\tilde{d}_1$ being the lightest ones. The flavor-violating elements in the squark mass matrix can be manipulated by the flavor off-diagonal elements in the soft SUSY-breaking mass matrices and trilinear couplings. The inputs of the model can then be chosen in the so-called Super-Cabibbo-Kobayashi-Maskawa (Super-CKM) basis, where the squarks are rotated in parallel to the quarks, as defined in [68]. However, even if only flavor diagonal entries of the soft SUSY-breaking parameters are set, flavor violation in the mass matrices in the Super-CKM basis is induced by the CKM matrix. This is inevitable due to $SU(2)_L$ invariance enforcing the common soft SUSY-breaking mass matrix $m^2_{\tilde{Q}}$ for left-handed up-type and down-type squarks, faced with the distinct rotations of up- and down-quarks in flavor space. By convention in this case the down-type sector is diagonal in flavor space, whereas the up-type sector remains flavor mixed, with the mixing given by the CKM matrix. This general mixing of squarks is considered in Ch. 3, and with the parameter choices made there, the strongest contribution to the lightest up-type squark $\tilde{u}_1$ stems from the top flavor as the left-right-mixing for the stops is much larger than the flavor mixing.
For sleptons throughout this work only the left-right-mixing is considered for the staus, while for the smuons and selectrons the left- and right-handed states are taken to be mass eigenstates. Accordingly, in Ch. 3, where the soft SUSY-breaking parameters are set explicitly, it is sufficient to provide the diagonal entries of the matrices $m^2_{\tilde{L}}$ and $m^2_{\tilde{E}}$, given by $m_{\tilde{L}_i}$, $i = 1, 2, 3$ and $m_{\tilde{E}_R}$, $E = e, \mu, \tau$, and correspondingly for the trilinear couplings.

2.1.3. Experimental Constraints

Important searches of the two experiments ATLAS and CMS at the LHC concentrate on the production of SUSY particles. For the work on the decay of the lightest up-type squark in Ch. 3, the limits obtained for the production of stops are taken over, because as explained in Sec. 2.1.2 in our case the $\tilde{u}_1$ is stop-like. Current limits on stop pair production from both experiments are shown in Fig. 2.1. In both summary plots, the result is plotted in the plane of the mass of the light stop $m_{\tilde{t}_1}$ and the mass of the lightest neutralino $m_{\tilde{\chi}^0_1}$, such that constant differences are given by straight lines from the lower left to the upper right, as indicated explicitly by the dashed lines in Fig. 2.1(a). As can be inferred, the exclusion limits strongly depend on the kinematic situation and the decay channel of the stop, once the mass difference is smaller than the mass of the top-quark. The specific analyses for different decay channels and kinematic regions are indicated in the legends of the plots. An important aspect for deriving these limits is to have precise predictions for the branching ratios in the region of small mass differences between the stop and the neutralino. Note, that in Fig. 2.1(b) the region where the mass difference is smaller than the mass of the W boson m_W is not shown, but results for this region can be found in [71]. According to the plots, the highest stop mass that can be excluded is about 550 GeV in case the mass difference is smaller than the mass of the top-quark, but larger than the W boson mass. However, if the mass difference is slightly smaller than m_W, a stop is only excluded for $m_{\tilde{t}_1} \lesssim 300$ GeV. The white spots for small stop masses in Fig. 2.1(a) are not covered by the searches indicated in the legend so far. At the time the research described in Ch. 3 has been done, these limits were still much weaker [72–77] and the coverage with different decay modes across the kinematic thresholds was not

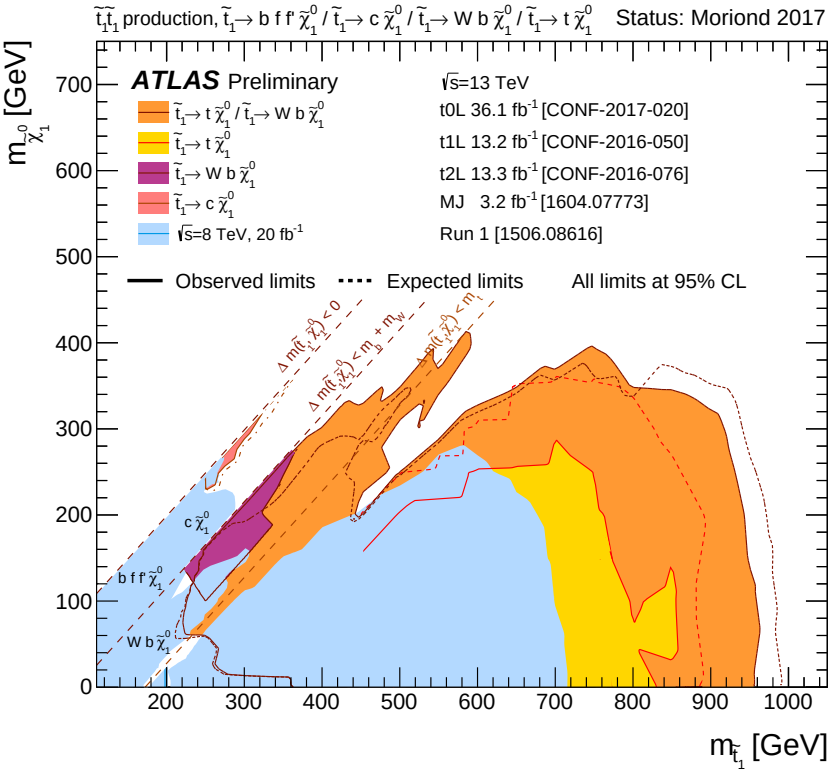

(a) Exclusion limits from ATLAS, taken from [69].

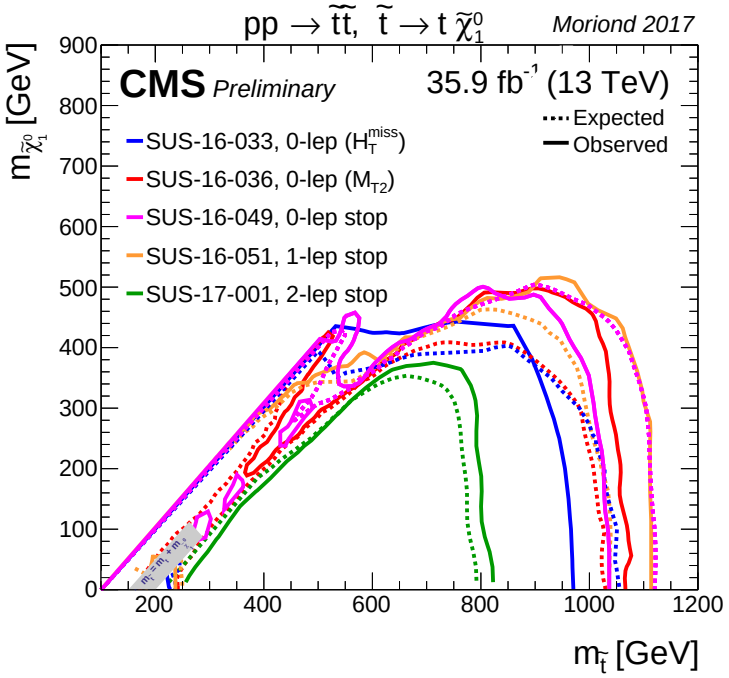

(b) Exclusion limits from CMS, taken from [70].

Figure 2.1: Summary plots of exclusion limits for stop pair production in various decay channels for different values of the mass difference between the stop and the lightest neutralino. The specific analyses are indicated in the legends of the plots.

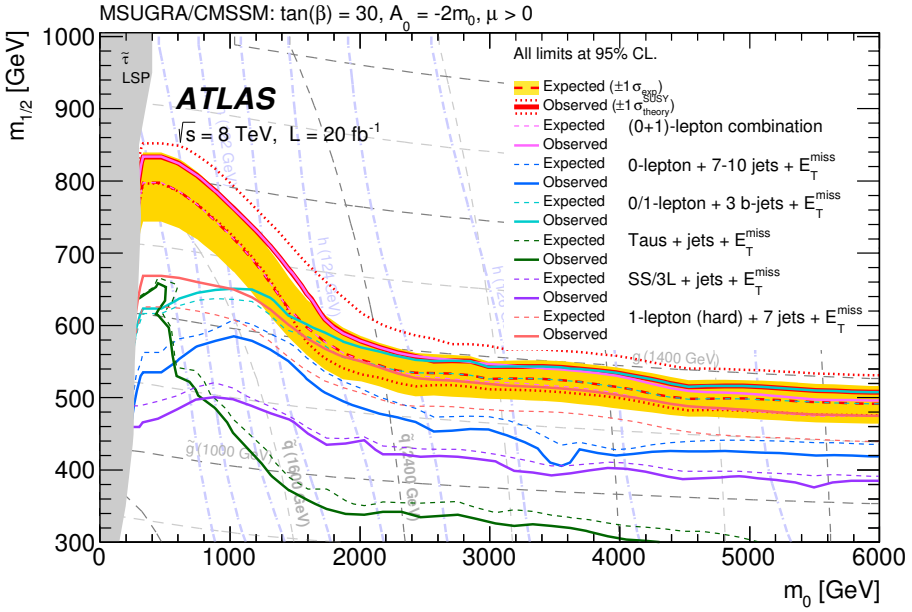

Figure 2.2: Exclusion limits on mSUGRA scenarios obtained by ATLAS [69, 78].

complete. Hence, an important motivation was also to show the contribution of possible decay channels for this region. Furthermore, the limits reported in Fig. 2.1 were derived for branching ratios of 100% for the respective final states. If the branching ratios are smaller, the expected cross sections are smaller as well and thereby the limits will be lower. This is of particular interest in the region where the mass difference of the stop and the lightest neutralino is smaller than the top-quark mass, such that several competing decay channels are relevant. The experimental bounds used for the analysis are the ones which were available when the work was done and are described in Sec. 3.2.
While the exclusion limits on stop pair production have been obtained by interpretation within simplified models, the observed limits on cross sections for the production of SUSY particles have also been interpreted within the mSUGRA approach described in Sec. 2.1.1, which is used for the analysis of squark gluino production in Ch. 4. This way it is possible to constrain the input parameters of the model directly. The plot in Fig. 2.2 shows the obtained exclusions for the first run of the LHC in the plane of the common scalar mass parameter m_0 and the common fermion mass parameter $m_{1/2}$, while the other parameters have been set to

$$A_0 = -2m_0 \ , \qquad \tan\beta = 30 \ , \qquad \mu > 0 \ . \tag{2.16}$$

The physical mass spectrum resulting from the input parameters is schematically indicated by the dashed grey and light blue lines in the background. The scenarios chosen for the analysis in Ch. 4 are guided by the choice of Eq. (2.16) and are located in the region which is not excluded in Fig. 2.2. Additionally they fulfill current limits on the masses of squarks, gluinos and stops as described in Sec. 4.5.

2.2. Fixed Order Calculations and Event Generators

This section provides principles of hadronic cross sections and NLO calculations in Sec. 2.2.1 and major aspects of the event generator POWHEG − BOX in Sec. 2.2.2. These basics are used in the calculation of squark gluino production in Ch. 4.

2.2.1. Fixed Order Calculation at Next-to-Leading Order

The calculations performed in this work are tailored to experiments at the LHC, where bunches of protons[4] are accelerated in opposite directions and are brought to collision in the center of the detectors, as for instance ATLAS and CMS. However, the protons are composite objects and the calculations performed here are based on quarks and gluons in the initial state, which are constituents of the protons. The relation between the differential hadronic cross section for a final state f with n particles and with protons P_1, P_2 in the initial state, $\mathrm{d}\sigma_{P_1P_2\to f}$, and the partonic scattering cross section $\mathrm{d}\sigma_{ij\to f}$ with initial partons i, j is given by the factorization formula [79]

$$\mathrm{d}\sigma_{P_1P_2\to f} = \int_0^1 \mathrm{d}x_1 \int_0^1 \mathrm{d}x_2 \sum_{i,j} f_{iP_1}(x_1,\mu_F) f_{jP_2}(x_2,\mu_F) \mathrm{d}\sigma_{ij\to f} \ , \tag{2.17}$$

where $f_{iP_1}(x_1,\mu_F)$ and $f_{jP_2}(x_2,\mu_F)$ are the parton distribution functions (PDFs) for the partons i in the proton P_1 and j in the proton P_2. The integration variables x_1 and x_2 are the fractions of the proton momenta taken by the two partons, such that the momenta of the initial partons of the partonic scattering cross section p_i and p_j are given by

$$p_i = x_1 p_{P_1} \ , \tag{2.18}$$

$$p_j = x_2 p_{P_2} \ , \tag{2.19}$$

where p_{P_1} and p_{P_2} are the momenta of the two protons. The sum extends over all suitable partons inside the proton, namely quarks and gluons in this work. The PDFs are determined experimentally and provide the probability of extracting a parton i with a momentum fraction x_1 of the proton, and a parton j with momentum fraction x_2. The PDFs depend on the factorization scale μ_F at which the factorization of the complete cross section into PDFs and the partonic cross section is performed. The calculation performed for the squark gluino production in Ch. 4 focuses on the partonic cross section which generically reads [80]

$$\mathrm{d}\sigma_{ij\to f} = \frac{1}{4\sqrt{(p_ip_j)^2 - m_i^2 m_j^2}} |\mathcal{M}_{ij\to f}|^2 \mathrm{d}\Phi_n \ , \tag{2.20}$$

where m_i and m_j are the masses of the incoming partons[5], $|\mathcal{M}_{ij\to f}|^2$ is the amplitude squared for the partonic process $ij \longrightarrow f$ which can be calculated by Feynman diagrams and $\mathrm{d}\Phi_n$ denotes the n-particle phase space given by

$$\mathrm{d}\Phi_n = (2\pi)^4 \delta^4 \left(p_i + p_j - \sum_{k=1}^{n} p_{f_k} \right) \prod_{k=1}^{n} \frac{\mathrm{d}^3\vec{p}_{f_k}}{(2\pi)^3 2p^0_{f_k}} \ . \tag{2.21}$$

The delta function ensures four-momentum conservation, where p_{f_k}, $k = 1...n$ are the momenta of the n final state particles. The matrix element squared is determined order by order in perturbation theory. In Ch. 4 the leading order (LO) as well as the next-to-leading order in the strong coupling constant α_s are considered.
The calculation of the NLO corrections to the partonic process amounts to calculating virtual corrections to, and real emissions from the LO process. The loop diagrams appearing in the virtual corrections can lead to both ultraviolet (UV) and infrared (IR) divergences which have to be removed properly. The UV divergences can be extracted by continuation from four to

[4] Heavy ion collisions are not considered in this thesis.
[5] The masses of quarks of the first two generations are set to zero in Ch. 4.

$D = 4 - 2\epsilon$ dimensions, known as dimensional regularization, where the divergences show up as poles in ϵ. These poles can be eliminated by renormalization of the masses, couplings and wave functions in the Lagrangian. Thereby the bare parameters and fields are replaced by renormalized ones, and counterterms are added. The UV divergences are then absorbed by the counterterms so that the final result is UV finite. Conventional dimensional regularization breaks SUSY due to a mismatch of bosonic and fermionic degrees of freedom. This can be cured by introducing a SUSY-restoring counterterm [25]. We refrain from giving more details on the virtual corrections and the renormalization as they are not the focus of this thesis. Specific aspects for squark gluino production are given in Sec. 4.2.
The IR divergences contained in the virtual corrections are canceled by the IR divergences in the corresponding real emission amplitudes, as guaranteed by the Kinoshita-Lee-Nauenberg (KLN) theorem [81, 82]. For total cross sections $\sigma_{\text{tot}}^{\text{NLO}}$, this cancelation can be performed analytically, since the phase space for the real emission process $\mathrm{d}\Phi_{n+1}$ can be factorized into the Born phase space $\mathrm{d}\Phi_n$ and an additional phase space only accounting for the real emission $\mathrm{d}\Phi_{\text{rad}}$, so that

$$\sigma_{\text{tot}}^{\text{NLO}} = \int \mathrm{d}\Phi_n \left[\mathcal{B}(\Phi_n) + \mathcal{V}(\Phi_n) + \int \mathrm{d}\Phi_{\text{rad}} \mathcal{R}(\Phi_{n+1}) \right] . \tag{2.22}$$

The Born and virtual contribution with the renormalization already performed are denoted by $\mathcal{B}(\Phi_n)$ and $\mathcal{V}(\Phi_n)$ and depend on n-body kinematics Φ_n, whereas the real correction is denoted by $\mathcal{R}(\Phi_{n+1})$ and depends on $(n+1)$-body kinematics Φ_{n+1}. Integrating out the additional phase space $\mathrm{d}\Phi_{\text{rad}}$ in D dimensions reveals the IR divergences as poles in ϵ which cancel the IR divergences of the virtual corrections. Hence the integrand of the Born phase space integration is already IR finite, and the integration can be performed in four dimensions safely. The cancelation of the IR divergences in an event generator like the POWHEG − BOX, however, requires additional work explained in Sec. 2.2.2.

In this thesis the squark gluino production and the subsequent decays of the squark and the gluino are investigated. Including also the decay of the squark stemming from the gluino decay the entire process is hence a $2 \to 5$ process, schematically illustrated by the graph in Fig. 2.3, where the quarks and squarks can be of any light flavor and both left- and right-handed and only the decay of the squark into a quark and the lightest neutralino is considered. The NLO corrections in the strong coupling constant to this process involve many different loop topologies up to hexagon diagrams and real emission graphs with six particles in the final state, rendering the calculation complicated. A common method to reduce the complexity of the calculation is given by the Narrow Width Approximation (NWA) (see [83] and references therein), which allows for separating the complete process into the production of an on-shell squark and gluino, and the subsequent on-shell decays of the particles. Accordingly, the process can be split into the subprocesses indicated by the dashed lines cutting the squark and gluino lines in Fig. 2.3, which are

$$q + g \longrightarrow \tilde{q} + \tilde{g} , \tag{2.23}$$

$$\tilde{g} \longrightarrow \tilde{q} + \bar{q} , \tag{2.24}$$

$$\tilde{q} \longrightarrow q + \tilde{\chi}_1^0 . \tag{2.25}$$

The NWA holds in the limit where the width Γ_i of the unstable intermediate particle $i = \tilde{q}, \tilde{g}$ is small, since in this limit for the denominator of the propagator in the amplitude squared holds

$$\frac{1}{(p_i^2 - m_i^2)^2 + m_i^2 \Gamma_i^2} \xrightarrow{m_i \Gamma_i \to 0} \frac{\pi}{m_i \Gamma_i} \delta(p_i^2 - m_i^2) , \tag{2.26}$$

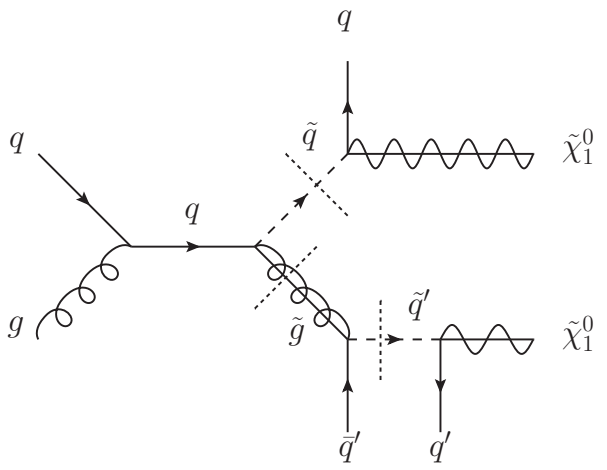

Figure 2.3: Complete process of squark gluino production including the decays of the gluino and the squarks. The dashed lines cutting the lines of the squarks and the gluino split the entire process into the subprocesses calculated in the Narrow Width Approximation.

where p_i is the momentum of the intermediate particle. This limit sets the intermediate particle on-shell and allows for the factorization of production and decay. For squarks and gluinos this is a good approximation for the scenarios considered here, such that the expected error of $\mathcal{O}(\Gamma_i/m_i)$ [84, 85] is small. In this approximation, NLO corrections have to be calculated for the specific subprocesses Eqs. (2.23)-(2.25). Employing the NWA, the differential cross section for the entire process at LO $\mathrm{d}\sigma_{\mathrm{tot}}^{\mathrm{LO}}$ is then given by

$$\mathrm{d}\sigma_{\mathrm{tot}}^{\mathrm{LO}} = \mathrm{d}\sigma_0 \frac{\mathrm{d}\Gamma_0^{\tilde{g}\to\tilde{q}'\bar{q}'}}{\Gamma_0^{\tilde{g}}} \frac{\mathrm{d}\Gamma_0^{\tilde{q}\to q\tilde{\chi}_1^0}}{\Gamma_0^{\tilde{q}}} \frac{\mathrm{d}\Gamma_0^{\tilde{q}'\to q'\tilde{\chi}_1^0}}{\Gamma_0^{\tilde{q}'}} \ , \tag{2.27}$$

where $\mathrm{d}\sigma_0$ is the differential cross section at LO for the production of the squark and the gluino, $\mathrm{d}\Gamma_0^{\tilde{g}\to\tilde{q}'\bar{q}'}$, $\mathrm{d}\Gamma_0^{\tilde{q}\to q\tilde{\chi}_1^0}$ and $\mathrm{d}\Gamma_0^{\tilde{q}'\to q'\tilde{\chi}_1^0}$ are the differential partial decay widths at LO for the decays indicated in the superscript, and Γ_0^i, $i = \tilde{g}, \tilde{q}, \tilde{q}'$ are the total decay widths at LO for the particles i. For the total cross section $\sigma_{\mathrm{tot}}^{\mathrm{LO}}$ the ratios of partial and total decay widths become branching ratios, resulting in

$$\sigma_{\mathrm{tot}}^{\mathrm{LO}} = \sigma_0 \cdot \mathrm{BR}(\tilde{g} \to \tilde{q}'\bar{q}') \cdot \mathrm{BR}(\tilde{q} \to q\tilde{\chi}_1^0) \cdot \mathrm{BR}(\tilde{q}' \to q'\tilde{\chi}_1^0) \ , \tag{2.28}$$

where BR denotes the branching ratio of the decay indicated in the argument. Inserting the expansions of the differential NLO production cross section $\mathrm{d}\sigma$ and the (differential partial) decay widths (d)Γ in the strong coupling constant

$$\mathrm{d}\sigma = \mathrm{d}\sigma_0 + \alpha_s \mathrm{d}\sigma_1 \ , \tag{2.29}$$

$$\mathrm{d}\Gamma^{\tilde{g}\to\tilde{q}'\bar{q}'} = \mathrm{d}\Gamma_0^{\tilde{g}\to\tilde{q}'\bar{q}'} + \alpha_s \mathrm{d}\Gamma_1^{\tilde{g}\to\tilde{q}'\bar{q}'} \ , \tag{2.30}$$

$$\mathrm{d}\Gamma^{\tilde{q}\to q\tilde{\chi}_1^0} = \mathrm{d}\Gamma_0^{\tilde{q}\to q\tilde{\chi}_1^0} + \alpha_s \mathrm{d}\Gamma_1^{\tilde{q}\to q\tilde{\chi}_1^0} \ , \tag{2.31}$$

$$\mathrm{d}\Gamma^{\tilde{q}'\to q'\tilde{\chi}_1^0} = \mathrm{d}\Gamma_0^{\tilde{q}'\to q'\tilde{\chi}_1^0} + \alpha_s \mathrm{d}\Gamma_1^{\tilde{q}'\to q'\tilde{\chi}_1^0} \ , \tag{2.32}$$

$$\Gamma^i = \Gamma_0^i + \alpha_s \Gamma_1^i \ , \quad i = \tilde{g}, \tilde{q}, \tilde{q}' \tag{2.33}$$

in Eq. (2.27) and keeping only terms up to $\mathcal{O}(\alpha_s)$ yields the formula for the differential cross section for squark gluino production at NLO combined with the decays of the gluino and the

squarks in the NWA $\mathrm{d}\sigma_{\mathrm{tot}}^{\mathrm{NLO}}$ used in this thesis

$$\begin{aligned}\mathrm{d}\sigma_{\mathrm{tot}}^{\mathrm{NLO}} =& \frac{1}{\Gamma_0^{\tilde{g}}\Gamma_0^{\tilde{q}}\Gamma_0^{\tilde{q}'}}\Bigg[\mathrm{d}\sigma_0\mathrm{d}\Gamma_0^{\tilde{g}\to\tilde{q}'\bar{q}'}\mathrm{d}\Gamma_0^{\tilde{q}\to q\tilde{\chi}_1^0}\mathrm{d}\Gamma_0^{\tilde{q}'\to q'\tilde{\chi}_1^0}\left(1-\alpha_s\left(\frac{\Gamma_1^{\tilde{g}}}{\Gamma_0^{\tilde{g}}}+\frac{\Gamma_1^{\tilde{q}}}{\Gamma_0^{\tilde{q}}}+\frac{\Gamma_1^{\tilde{q}'}}{\Gamma_0^{\tilde{q}'}}\right)\right)\\ &+\alpha_s\Bigg(\mathrm{d}\sigma_1\mathrm{d}\Gamma_0^{\tilde{g}\to\tilde{q}'\bar{q}'}\mathrm{d}\Gamma_0^{\tilde{q}\to q\tilde{\chi}_1^0}\mathrm{d}\Gamma_0^{\tilde{q}'\to q'\tilde{\chi}_1^0}+\mathrm{d}\sigma_0\mathrm{d}\Gamma_1^{\tilde{g}\to\tilde{q}'\bar{q}'}\mathrm{d}\Gamma_0^{\tilde{q}\to q\tilde{\chi}_1^0}\mathrm{d}\Gamma_0^{\tilde{q}'\to q'\tilde{\chi}_1^0}\\ &+\mathrm{d}\sigma_0\mathrm{d}\Gamma_0^{\tilde{g}\to\tilde{q}'\bar{q}'}\mathrm{d}\Gamma_1^{\tilde{q}\to q\tilde{\chi}_1^0}\mathrm{d}\Gamma_0^{\tilde{q}'\to q'\tilde{\chi}_1^0}+\mathrm{d}\sigma_0\mathrm{d}\Gamma_0^{\tilde{g}\to\tilde{q}'\bar{q}'}\mathrm{d}\Gamma_0^{\tilde{q}\to q\tilde{\chi}_1^0}\mathrm{d}\Gamma_1^{\tilde{q}'\to q'\tilde{\chi}_1^0}\Bigg)\Bigg]\ .\end{aligned} \tag{2.34}$$

In Eqs. (2.29)-(2.34) the quantities with subscript '1' denote the NLO correction to the quantity. If any of the subprocesses is calculated only at LO, in Eq. (2.34) the terms proportional to the NLO correction of this process drop out.
Final state radiation from the production process could be interpreted as initial state radiation from the decay process, depending on whether the radiation takes place before or after the intermediate particle is on-shell. Although in the entire process this appears as a single contribution, within the NWA both final state radiation off the production and initial state radiation off the decay have to be taken into account [86].

2.2.2. Matching to Parton Showers via POWHEG − BOX

In an event generator instead of the analytic cancelation of the IR divergences in the integral over the entire phase space as explained in Sec. 2.2.1, a pointwise cancelation of the divergences is required, which is provided by a subtraction method. The idea of a subtraction method is the following: counterterms $\mathcal{C}(\Phi_{n+1})$ are introduced which have the same singular behavior as the real emission amplitudes and which are easy to integrate analytically. Adding and subtracting these counterterms in Eq. (2.22) yields

$$\begin{aligned}\sigma_{\mathrm{tot}}^{\mathrm{NLO}} =& \int \mathrm{d}\Phi_n\left[\mathcal{B}(\Phi_n)+\mathcal{V}(\Phi_n)+\int\mathrm{d}\Phi_{\mathrm{rad}}\mathcal{C}(\Phi_{n+1})\right]\\ &+\int\mathrm{d}\Phi_{n+1}\left[\mathcal{R}(\Phi_{n+1})-\mathcal{C}(\Phi_{n+1})\right]\ .\end{aligned} \tag{2.35}$$

In the integral over the Born phase space $\mathrm{d}\Phi_n$ the analytic structure of IR divergences is universal and known. The counterterms integrated over the radiation phase space can then be used to cancel the divergences, such that the integrand is finite and the integration over the Born phase space can be performed numerically. As the singular structure of the counterterms is the same as for the real corrections, also the integral over the phase space including the real radiation $\mathrm{d}\Phi_{n+1}$ can be performed numerically and the singularities are canceled pointwise[6]. The total result remains unaltered. In the event generator POWHEG − BOX a specific variant called Frixione-Kunszt-Signer (FKS) subtraction scheme [87, 88] is implemented and the subtraction terms are generated automatically once the user provides color and spin correlated Born amplitudes defined in Sec. 4.4. The color and spin correlated amplitudes serve as building blocks for the subtraction method due to the factorization of the real amplitudes in the soft and collinear limits. Specific details on the implementation of the FKS subtraction scheme in the POWHEG − BOX can be found in [37].

The hard scattering process described by $\sigma_{\mathrm{tot}}^{\mathrm{NLO}}$ is only the first step of deriving predictions for physical events which can be measured by experiments. The quarks in the final state of the hard scattering depicted in Fig. 2.3 will radiate gluons which can radiate further or

[6] Note, that counterterms required for canceling initial state collinear singularities are not considered here for simplicity. Details can be found in [37].

split into quarks, such that a cascade of partons is produced. When the energy scale of the partons reaches a sufficiently low value, due to color confinement the partons form hadrons that are color singlets and which can decay further. Moreover the remnants of the protons which collide and give rise to the hard scattering process are not color singlets any more, so that also their evolution has to be modeled. All these steps connecting the hard scattering process calculated here to the physical event recorded by experiments are performed by parton showers.
At NLO combining the hard scattering process with the parton shower poses the following problem: the first radiation performed by a parton shower off the Born process is covered by the real correction of the hard scattering already, which leads to a double counting. One way to avoid this double counting problem is to subtract from the NLO calculation of the hard scattering process the contribution the parton shower would generate, known as MC@NLO approach [89]. However, the difference of the NLO computation and the parton shower contribution is not necessarily positive. Hence, events with negative weights are possible. Moreover, the NLO computation has to be adapted to the parton shower which is attached. The event generator POWHEG − BOX used in this work employs another approach called POWHEG method [36, 37] (POsitive Weight Hardest Emission Generator). Here, the hardest emission is generated first with the full NLO accuracy, which leads to positive weights by construction[7]. The differential POWHEG cross section $\mathrm{d}\sigma_{\mathrm{PWHG}}$ is given by [37]

$$\mathrm{d}\sigma_{\mathrm{PWHG}} = \bar{B}(\Phi_n)\left[\Delta(\Phi_n, p_T^{\min}) + \Delta(\Phi_n, k_T(\Phi_{n+1}))\frac{\mathcal{R}(\Phi_{n+1})}{\mathcal{B}(\Phi_n)}\mathrm{d}\Phi_{\mathrm{rad}}\right]\mathrm{d}\Phi_n \ , \tag{2.36}$$

where

$$\bar{B}(\Phi_n) = \mathcal{B}(\Phi_n) + \bar{\mathcal{V}}(\Phi_n) + \int \mathrm{d}\Phi_{\mathrm{rad}}\left(\mathcal{R}(\Phi_{n+1}) - \mathcal{C}(\Phi_{n+1})\right) \tag{2.37}$$

with the renormalized virtual amplitude with all IR singularities canceled by appropriate subtractions denoted by $\bar{\mathcal{V}}(\Phi_n)$. The POWHEG Sudakov form factor is called $\Delta(\Phi_n, p_T)$ and can be interpreted as probability for no emission down to p_T and reads

$$\Delta(\Phi_n, p_T) = \exp\left\{-\int \frac{\mathcal{R}(\Phi_{n+1})}{\mathcal{B}(\Phi_n)}\mathrm{d}\Phi_{\mathrm{rad}}\theta(k_T(\Phi_{n+1}) - p_T)\right\} \ . \tag{2.38}$$

The first emission in Eq. (2.36) is hence generated with a transverse momentum k_T with a lower cutoff $p_T^{\min}$. All subsequent emissions generated by the parton shower will have smaller transverse momenta and accordingly, the NLO calculation is matched to the parton shower without double counting. The POWHEG − BOX generates events at NLO precision with the hardest radiation according to Eq. (2.36) and writes them to Les Houches Event (LHE) files [90] which can be forwarded to a parton shower. The essential ingredients for the implementation of squark gluino production in the POWHEG − BOX are summarized in Sec. 4.4 and details on POWHEG and the POWHEG − BOX can be found in [36–38].

2.3. The Electroweak Phase Transition

Introductions and reviews for EWBG and field theory at finite temperature can be found for instance in [91–93]. The dynamics of the EWPT are governed by the effective potential V_{eff} which will be explained in detail in Sec. 5.1. Schematically, the behavior of the effective potential with respect to the temperature around the phase transition can be deduced from Fig. 2.4. The figure displays a one-dimensional potential $V(\omega, T)$ depending on the variable

[7] Note, that due to the NLO expansion of the total widths Eq. (2.33) negative events are possible in the NWA Eq. (2.34) due to the resulting correction $\propto \alpha_s$ in the first line of Eq. (2.34). This can be avoided by leaving the total widths unexpanded with the drawback, that the total NLO cross section is not reproduced.

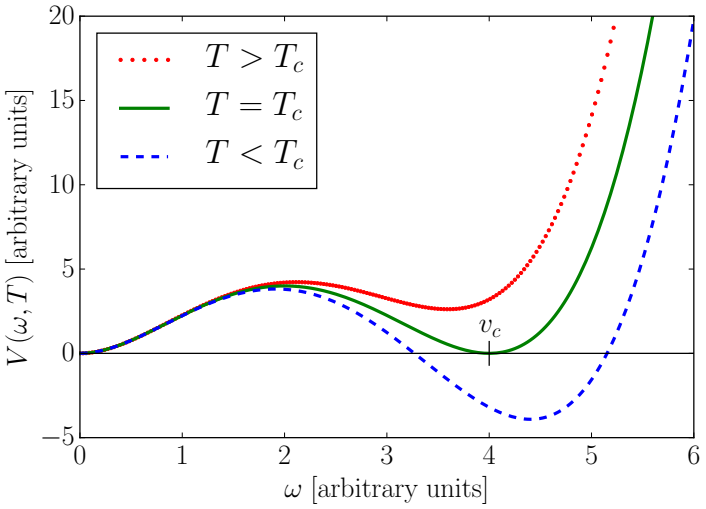

Figure 2.4: General one-dimensional potential in arbitrary units for different temperatures T.

ω which will take the role of a specific field configuration in Sec. 5.1 and the temperature T. Illustrating the basic properties of the effective potential around the temperature where the phase transition happens, we show three representative cases of the temperature: a high temperature (red, dotted), the temperature where the phase transition takes place T_c (green line) and a low temperature (blue, dashed). In the early universe at high temperatures $T > T_c$, the potential might exhibit several minima varying with the temperature, but the global minimum determining the ground state of the system is always located at $\omega = 0$. Consequently the vacuum expectation value v vanishes and the electroweak symmetry is not broken. As the universe evolves and cools down, at some point a temperature T_c, called critical temperature, is reached, where one of the minima other than the one at $\omega = 0$ has the same depth as the one at the origin, leading to two degenerate minima. The position of the minimum other than the one at $\omega = 0$ determines the critical vacuum expectation value v_c. When the universe cools down further, the new minimum at $\omega \neq 0$ will get deeper than the one at $\omega = 0$ and therefore turn into the new global minimum. Hence, there will be a finite non-zero vacuum expectation value for $T < T_c$ and the electroweak symmetry is broken. Accordingly, the phase transition is marked by a jump of the vacuum expectation value from zero to a non-zero value at $T = T_c$. Phase transitions from the minimum at $\omega = 0$ to the global minimum at $\omega \neq 0$ with a potential barrier in between such that the transition to the global minimum proceeds via tunneling through the barrier are of first order. For successful EWBG, the phase transition not only has to be of first order [41], but it also has to be strong enough: in this work, we classify a phase transition to be strong first order and consequently valid for EWBG, if (see for example [91–93] and references therein)

$$\frac{v_c}{T_c} \geq 1 \,. \tag{2.39}$$

Thus, for the 2HDM to be able to explain the BAU it is essential to investigate the EWPT in this model to quantify the ratio v_c/T_c. Existing works [94–107] have already studied the EWPT and possible EWBG in the 2HDM. But only in [107] the results of the LHC at a center of mass energy of 8 TeV and especially the discovery of a Higgs boson at a mass of roughly 125 GeV were taken into account for phenomenological studies. In our work [108]

we not only take into account the latest results from the LHC at 13 TeV, but also relevant results from flavor physics, electroweak precision experiments and tree-level perturbative unitarity. Furthermore, we propose a novel treatment of massless Goldstone bosons in the renormalization procedure, other than the regularization applied in [106, 107]. Moreover, we develop a new renormalization scheme which for the first time preserves both masses and mixing angles of the Higgs sector at the tree-level values. At high temperature the effective potential at one-loop can lose meaningfulness due to large contributions from higher orders in perturbation theory. These contributions can be captured by resumming higher-order corrections from so-called ring-diagrams [109–111]. Both methods proposed in [110, 111] are investigated in our work. All details concerning the calculation, the renormalization and the results are presented in Ch. 5.

3. Decays of the Lightest Up-Type Squark

In Sec. 2.1.3 the current limits on the mass of the light stop were explained, together with the dependence of the limits on the investigated decay channels at the kinematic thresholds. The first threshold is located where the W boson can be produced on-shell in the decay of the light stop, and the second one resides where the top-quark can be on-shell. As explained in Sec. 2.1.3, these limits are carried over to the lightest up-type squark $\tilde{u}_1$ for the case of general flavor mixing investigated here. In this work the focus is on the parameter region leading to differences of the mass of the lightest up-type squark $m_{\tilde{u}_1}$ to the mass of the lightest neutralino $m_{\tilde{\chi}_1^0}$, $\Delta m = m_{\tilde{u}_1} - m_{\tilde{\chi}_1^0}$ from $\Delta m = 60$ GeV up to $\Delta m = 140$ GeV, covering the first of the two thresholds and investigate possible decay modes of the lightest up-type squark $\tilde{u}_1$ (*cf.* 2.1.2). In Sec. 3.1 possible decay modes of the $\tilde{u}_1$ are explained. After a brief summary of the numerical setup in Sec. 3.2, the results are presented in Sec. 3.3. We finish this chapter by a conclusion in Sec. 3.4.

3.1. Decay Channels

In the parameter region, where the W boson cannot be produced on-shell, there are two competing decay modes

$$\tilde{u}_1 \longrightarrow \tilde{\chi}_1^0(u, c) \ , \tag{3.1}$$

where $\tilde{\chi}_1^0$ is the lightest neutralino and u and c are the up- and charm-quark, respectively, and

$$\tilde{u}_1 \longrightarrow \tilde{\chi}_1^0 d_i f \bar{f}' \ , \quad i = 1...3 \ , \tag{3.2}$$

with d_i, $i = 1...3$ being a down-type quark of generation i and $f\bar{f}'$ denoting all possible combinations that can result from a W boson decay with $f = u, d, s, c, \tau, \nu_\tau, \mu, \nu_\mu, e, \nu_e$. If the mass difference Δm exceeds the sum of the W boson mass m_W and the mass of the down-type quark m_{d_i}, the W boson can be produced on-shell in the decay of the $\tilde{u}_1$ and the four-body decay Eq. (3.2) turns into the three-body decay

$$\tilde{u}_1 \longrightarrow \tilde{\chi}_1^0 W^+ d_i \ . \tag{3.3}$$

A representative Feynman diagram for each of these three decay modes is shown in Fig. 3.1.

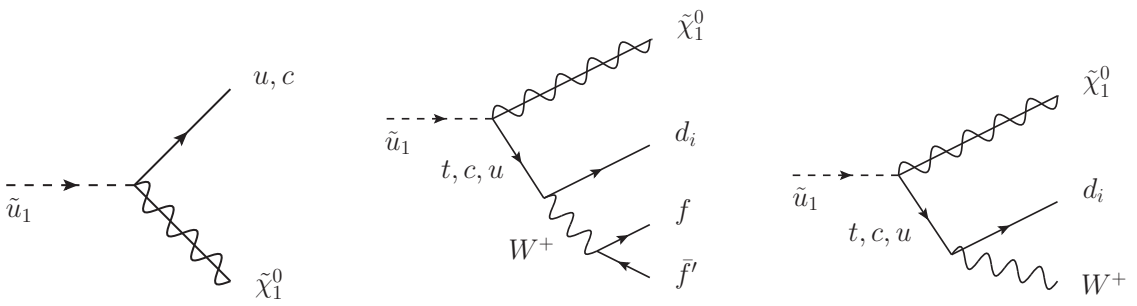

(a) Example for the two-body decay Eq. (3.1).

(b) Example for the four-body decay Eq. (3.2).

(c) Example for the three-body decay Eq. (3.3).

Figure 3.1: Representative Feynman diagrams for the three decay modes considered.

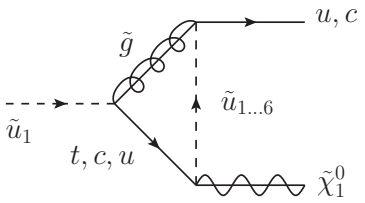

Figure 3.2: Example for a one-loop correction to the two-body decay Eq. (3.1).

The tree-level diagram for the two-body decay $\tilde{u}_1 \longrightarrow \tilde{\chi}_1^0(u, c)$ is shown in Fig. 3.1(a). The general flavor structure as explained in Sec. 2.1.2 is vital for this process to happen at tree-level. The four-body decay is represented by Fig. 3.1(b), where due to the flavor mixing, all three up-type quarks can propagate internally. The corresponding diagram for the three-body decay is shown in Fig. 3.1(c), which is obtained from Fig. 3.1(b) by leaving the W boson undecayed. For the two-body decay, SUSY-Quantum-Chromo-Dynamic (SUSY-QCD) corrections were included, where a representative diagram is shown in Fig. 3.2. The general flavor structure affects all three vertices and causes all three generations of up-type quarks and all six up-type squarks to propagate in the loop.
Previous calculations for the flavor-changing neutral current two-body decay of the light stop into a charm-quark and the lightest neutralino [15, 16] showed that within the hypothesis of Minimal Flavor Violation [112–115] resummation effects should be taken into account by solving RGEs, leading to flavor-changing elements in the squark mixing matrix. For that reason the two-body decay has been calculated with general flavor mixings including contributions at NLO in SUSY-QCD [17, 116, 117]. In order to consistently compare the two-body decay to the other decay modes, also the three- and four-body decays have been calculated with a general flavor structure, thereby extending existing calculations for these decay modes [19, 20, 118]. Moreover, the masses of fermions of the third generation have been taken into account in the final state. Details on the three- and four-body decays have been presented in [117] and [21]. Here, we put emphasis on the method employed to account for finite width effects in the four-body decay, resulting from a W boson going on-shell.
The amplitude for the four-body decay has contributions proportional to

$$\frac{1}{p_W^2 - m_W^2} \,, \tag{3.4}$$

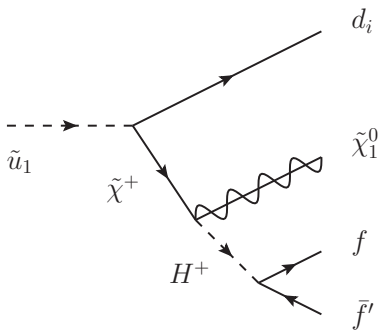

Figure 3.3: Example for a non-resonant contribution to the four-body decay of the $\tilde{u}_1$, which is suppressed at the W threshold due to the factor Eq. (3.5).

where p_W is the W boson four-momentum, stemming from the W boson propagator in diagrams like the one shown in Fig. 3.1(b). These terms lead to a singularity once the phase space available in the decay of the $\tilde{u}_1$ is large enough to allow for $p_W^2 = m_W^2$. In order to cure this singularity the amplitude can be regularized by incorporating the finite width of the W boson. In general, this can be done in a consistent and gauge-invariant way by the Complex-Mass-Scheme [119]. In our case, however, a simpler approach is also valid: the Overall-Factor-Scheme [120]. In this scheme, the entire amplitude is multiplied by

$$\frac{p_W^2 - m_W^2}{p_W^2 - m_W^2 + \mathrm{i} m_W \Gamma_W} \tag{3.5}$$

for each W boson propagator which can become singular in the integration over the phase space. More precisely, among all terms of the amplitude the maximum power of the divergent propagator Eq. (3.4) has to be figured out and the whole amplitude has to be multiplied by the non-divergent factor Eq. (3.5) to exactly that power. Thereby all divergent denominators are canceled and replaced by the expression leading to the correct Breit-Wigner resonance shape when squaring the amplitude. Since the entire amplitude is multiplied in this way, gauge invariance is preserved. Moreover, having analytical expressions of the amplitudes at hand, the implementation of this procedure is straight forward. The drawback of this method is the suppression of non-resonant contributions at the threshold due to uncanceled numerators of Eq. (3.5). In our calculation this affects diagrams without any internal W bosons, such as for instance the one shown in Fig. 3.3 with an internal chargino $\tilde{\chi}^+$ and an internal charged Higgs H^+. In Fig. 3.4 we show the absolute value squared of the factor Eq. (3.5) as it is present in the matrix element squared in this method for $m_W = 80.385$ GeV and $\Gamma_W = 2.085$ GeV [121] as a function of the momentum of the W boson p_W. Apparently, the overall factor is close to one already ten GeV away from the threshold. Consequently, the suppression is limited to a narrow region around the threshold. Moreover, the contribution arising from diagrams similar to Fig. 3.3 to the total amplitude squared strongly depends on the masses of the internal particles and thereby on the specific scenario under consideration. To this end we verified explicitly that in all scenarios shown in the results below the non-resonant diagrams give only minor contributions. Hence, in our case the Overall-Factor-Scheme is a valid approach to describe the threshold effects when the W boson goes on-shell.

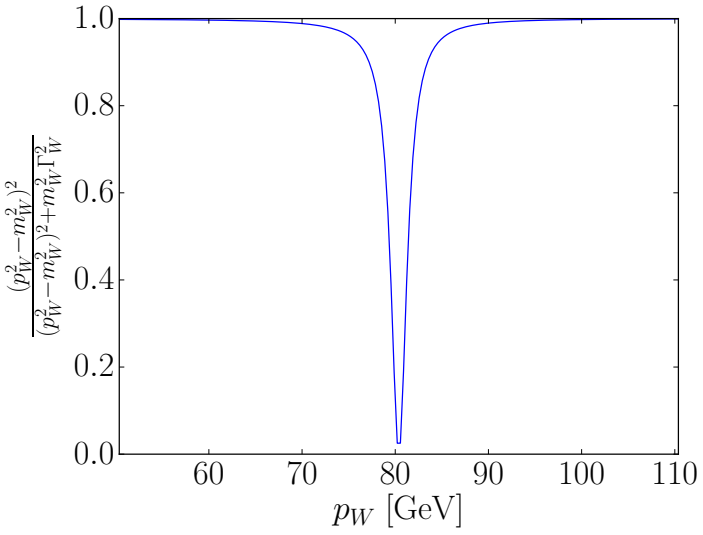

Figure 3.4: Absolute value squared of the overall factor of Eq. (3.5) as a function of the W boson momentum p_W.

3.2. Implementation and Numerical Setup

The numerical setup is explained in detail in Refs [17, 21, 116]. Here, the most important facts are summarized for convenience.
The three decay modes explained above have been implemented in the program package `SUSY-HIT` [17, 122]. Provided with all required input parameters by means of an SLHA2 [60, 68] file, the program can calculate the branching ratios of SUSY particle decays, including the decays considered here. The SUSY spectra were generated using the spectrum generator `SPHENO` [123, 124]. For the general MSSM with flavor violation the inputs are given by SM parameters and soft SUSY-breaking parameters. The SM parameters were set to [121]

$$\begin{aligned} G_F &= 1.166379 \cdot 10^{-5}\ \text{GeV}^{-2}\ , & \alpha_s(M_Z)_{\overline{\text{MS}}} &= 0.1185\ , \\ m_t(\text{pole}) &= 173.07\ \text{GeV}\ , & m_b(m_b)_{\overline{\text{MS}}} &= 4.18\text{GeV}\ , \\ M_Z(\text{pole}) &= 91.1876\ \text{GeV}\ , & m_\tau(\text{pole}) &= 1.77682\ \text{GeV}\ , \end{aligned} \tag{3.6}$$

and the CKM matrix has been provided by the Wolfenstein parametrization with the values [121]

$$\lambda = 0.22535\ , \quad A = 0.811\ , \quad \bar{\rho} = 0.131\ , \quad \bar{\eta} = 0.345\ . \tag{3.7}$$

Not all soft SUSY-breaking parameters have strong impact on the decays considered in this work. Moreover, due to the large number of input parameters a scan covering all parameters is unfavorable for practical reasons. Therefore we restricted the investigated parameter space and derived our scenarios with the following settings:
The soft SUSY-breaking bino mass M_1 has been varied within the range

$$M_1 \in [75, 500]\ \text{GeV}\ , \tag{3.8}$$

whereas the wino and gluino mass parameters M_2 and M_3 have been set to

$$M_2 = 650\ \text{GeV} \quad \text{and} \quad M_3 = 1530\ \text{GeV}\ , \tag{3.9}$$

respectively. This leads to a rather light bino-like neutralino being the LSP in our scenarios. The gluino mass parameter has been chosen as light as possible regarding the experimental exclusion bounds at the time when the analysis was performed. The wino mass parameter together with the higgsino mass parameter μ, which was set to

$$\mu = 900 \text{ GeV} , \tag{3.10}$$

ensure that there are no light charginos that could drop below experimental limits. The trilinear couplings of sleptons and down-type squarks of all three generations, and the trilinear couplings for up-type squarks of the first and second generation were taken to be zero. In contrast, the trilinear coupling of the stops A_t was varied in the range

$$A_t \in [1.0, 2.0] \text{ TeV} . \tag{3.11}$$

These values for A_t lead to large mixing in the stop sector so that one stop becomes light. This light stop contributes most to the lightest up-type squark which is the NLSP in our scenarios. Moreover, the large mixing enters the radiative corrections to the mass of the light CP-even Higgs boson and helps lifting the mass from the tree-level bound m_Z to the actual value measured by the experiments (see [125] and references therein). Furthermore, the Higgs sector of the MSSM is characterized by the ratio of the vacuum expectation values of the two Higgs doublets, $\tan\beta$, and the mass of the pseudoscalar Higgs boson m_A. These two parameters were varied within

$$\tan\beta \in [1, 15] \quad \text{and} \quad m_A \in [150, 1000] \text{ GeV} . \tag{3.12}$$

The values of $\tan\beta$ are favored by constraints on the parameter space due to B-physics observables, which we took into account. The bino-like LSP emerging from the choices in Eqs. (3.8) to (3.10) often causes the relic density to be too high to be compatible with experimental data. However, Higgs funnels offer a possibility to reduce the relic density, e.g. in the case of $2m_{\tilde{\chi}_1^0} \approx m_A$ via the annihilation of two neutralinos into a pseudo scalar Higgs in the s-channel. For that reason, the parameter m_A has been chosen such that the range accommodates this neutralino annihilation mode for the expected values of $m_{\tilde{\chi}_1^0}$ due to Eq. (3.8).
The remaining parameters which have to be defined are the soft SUSY-breaking masses for squarks and sleptons. As we do not investigate the impact of light sleptons on the decays explained in Sec. 3.1 we set the soft SUSY-breaking masses for sleptons to

$$M_{\tilde{E}_R} = M_{\tilde{L}_i} = 1 \text{ TeV} \; ; \; E = e, \mu, \tau \; ; \; i = 1, 2, 3 . \tag{3.13}$$

Thereby the sleptons are heavy enough to have negligible impact on the considered decays and at the same time evade the experimental exclusion limits. In the squark sector the soft SUSY-breaking masses for the third generation are important, since the lightest up-type squark $\tilde{u}_1$ is mostly stop-like. In order to have a light stop, but not a light sbottom, the soft SUSY-breaking mass for the right-handed stop $M_{\tilde{t}_R}$ was chosen in the range of

$$M_{\tilde{t}_R} \in [300, 600] \text{ GeV} . \tag{3.14}$$

Choosing the soft SUSY-breaking mass for the left-handed doublet of the third generation $m_{\tilde{Q}_{L3}}$ to be low instead, would lead to a light sbottom accompanying the light stop. In order to comply with experimental exclusion limits and to avoid a light right-handed sbottom, the soft

SUSY-breaking masses for the right-handed down-type squarks $m_{\tilde{D}_R}$ and the right-handed up-type squarks of the first and second generation $m_{\tilde{U}_R}$ have been fixed at

$$m_{\tilde{D}_R} = m_{\tilde{U}_R} = 1.5 \text{ TeV} \; ; \; D = d, s, b \; ; \; U = u, c \; . \tag{3.15}$$

Finally, the residual soft SUSY-breaking masses of left-handed squarks $m_{\tilde{Q}_L}$ have been set according to

$$m_{\tilde{Q}_1} = m_{\tilde{Q}_2} = 1.5 \text{ TeV} \; , \; m_{\tilde{Q}_3} \in [1.0, 1.5] \text{ TeV} \; . \tag{3.16}$$

All these parameters are read in by the spectrum generator at the scale

$$M_{\text{in}} = M_{\text{SUSY}} \; , \tag{3.17}$$

with M_{SUSY} being the geometric mean of the two stop masses.

In order to be valid scenarios for our numerical analysis, the scenarios generated with these parameter choices had to fulfill several experimental constraints. All constraints explained in the following are the ones which were available at the time the analysis was performed.
First of all, the scenario must provide a candidate that is compatible with the observed Higgs signal. We check this by invoking `HiggsSignals` [126]. As the MSSM comprises four Higgs bosons, but only one has been measured so far, we have to check for the non-observation of three of them. This is done by requiring the scenarios to pass `HiggsBounds` [127–130], which checks for compatibility with exclusion bounds at 95% confidence level. The effective couplings and branching ratios for the Higgs bosons required by these two programs were calculated using `HDECAY` [131–133]. As this program is not suited to work with arbitrary flavor mixing among the squarks, we reduced the general mixing of the squarks $\tilde{u}_s$, $s = 1...6$, to the dominant ones for the third generation and omitted the mixing for the first and second generation. This is possible since the flavor-violating elements in the mixing matrix are usually very small such that for each squark $\tilde{u}_s$ the dominant flavor contribution can be identified uniquely. From the mixing of the two resulting squarks which correspond to the third generation, the stop mixing matrix was constructed. The remaining squarks were assigned to the left- and right-handed squarks of the first and second generation giving the strongest contribution. The same procedure was followed for the down-type squarks. More details on this can be found in [116]. The error in the branching ratios and effective couplings caused by this are small in comparison to the experimental precision and can be neglected.
Further constraints on BSM physics originate from B-physics observables and in particular from rare meson decays. All scenarios considered in the analysis are required to fulfill

$$\text{BR}(B_s^0 \longrightarrow \mu^+\mu^-) = (2.8^{+0.7}_{-0.6}) \times 10^{-9} \qquad [134] \; , \tag{3.18}$$

$$\text{BR}(B^0 \longrightarrow \mu^+\mu^-) \; < \; 8.1 \times 10^{-10} \text{ at } 95\% \text{ CL} \qquad [135] \; , \tag{3.19}$$

$$\text{BR}(B^+ \longrightarrow \tau^+\nu_\tau \;) = \; (1.05 \pm 0.25) \times 10^{-4} \qquad [121] \; , \tag{3.20}$$

$$\text{BR}(B \longrightarrow X_s\gamma) \; = \; (355 \pm 24 \pm 9) \times 10^{-4} \qquad [136] \; . \tag{3.21}$$

The theory predictions of our scenarios for these observables have been calculated by `SuperIso` [137, 138] and were required to be within the two sigma range of Eq. (3.18) to Eq. (3.21). Moreover, the impact of the new particles in the spectrum on the ρ-parameter which is determined by electroweak precision measurements has been constrained by requiring the ρ-parameter for the spectrum calculated by `SPheno` to be within two standard deviations of

$$\rho = 1.0004 \pm 0.00024 \qquad [125] \; . \tag{3.22}$$

The lightest neutralino $\tilde{\chi}_1^0$ being the LSP in our scenarios is a suitable candidate for DM. The space telescope `Planck` reported a cold DM density of

$$\Omega_c h^2 = 0.1199 \pm 0.0027 \qquad [3] \ , \tag{3.23}$$

which we take as an upper bound on the neutralino relic density for our scenarios. This means that there could also be particles other than the neutralino that contribute to the observed DM density. To verify this bound the neutralino relic density has been calculated with `SuperIsoRelic` [139, 140] and

$$\Omega_c h^2 < 0.12 \tag{3.24}$$

was requested for a parameter point to be valid.
Finally there are limits from direct searches for SUSY particles. All scenarios had to fulfill a constraint on the gluino mass $m_{\tilde{g}}$ and on the masses of squarks of the first two generations $m_{\tilde{q}}$

$$m_{\tilde{g}} > 1450 \text{ GeV} \quad \text{and} \quad m_{\tilde{q}} > 900 \text{ GeV} \qquad [141, 142] \ . \tag{3.25}$$

In addition, there are limits on stop pair production which directly constrain the allowed masses for the light stop, depending on the mass of the lightest neutralino. These limits on the stop $\tilde{t}_1$ are taken over for the $\tilde{u}_1$ as in typical scenarios the dominant contribution to the $\tilde{u}_1$ stems from the stop flavor. However, these limits were derived under the assumption of the branching ratios being one for the respective decay modes which are looked for. If there are competing decay modes, this assumption is in general not valid any more and the resulting limits can be weaker. To investigate this impact, we have used the experimental exclusion limits, but reinterpreted them for branching ratios other than one under the assumption

$$\text{BR(2-body)} + \text{BR(4-body)} = 1 \tag{3.26}$$

for $m_{\tilde{u}_1} - m_{\tilde{\chi}_1^0} < m_W$. The details of this procedure are described in [17] and [117]. If the difference between the masses of the lightest up-type squark and the lightest neutralino, $\Delta m = m_{\tilde{u}_1} - m_{\tilde{\chi}_1^0}$, is larger than m_W, `SModelS` [143, 144] was used to check compatibility of the scenario under consideration with the limits from direct searches for SUSY particles.

3.3. Results

First, we investigate the transition from the four-body decay $\tilde{u}_1 \longrightarrow \tilde{\chi}_1^0 d_i f \bar{f}'$ to the three-body decay $\tilde{u}_1 \longrightarrow \tilde{\chi}_1^0 W^+ d_i$. In Fig. 3.5(a) we show the ratio of the partial decay width for the four-body decay divided by the one for the three-body decay. As expected, for mass differences well above the threshold, the two partial decay widths approach each other, resulting in a ratio $\Gamma_{\text{4-body}}/\Gamma_{\text{3-body}} \approx 1$. However, for mass differences of $\Delta m \approx 100$ GeV the partial decay widths can still differ by about 10%, with increasing values closer to the threshold[8]. Hence, predictions for the branching ratio of a particular final state close to the threshold will depend on whether the three-body or the four-body decay of the $\tilde{u}_1$ has been assumed. Inspecting the region of large Δm in Fig. 3.5(a) we observe that the decay width of the 4-body decay remains slightly above the width for the three-body decay. This emerges from the integration of the Breit-Wigner resonance resulting from the overall-factor of Eq. (3.5) in the phase space integration of the four-body decay. Thus, the small shift in the decay width at high Δm from the three- to the four-body decay can be regarded as the finite-width effect of the W boson. In Fig. 3.5(b) we show the partial decay width of all three decay modes with respect to

[8] The ratio diverges for $\Delta m \to m_W$ since the partial width for the three-body decay vanishes in this limit.

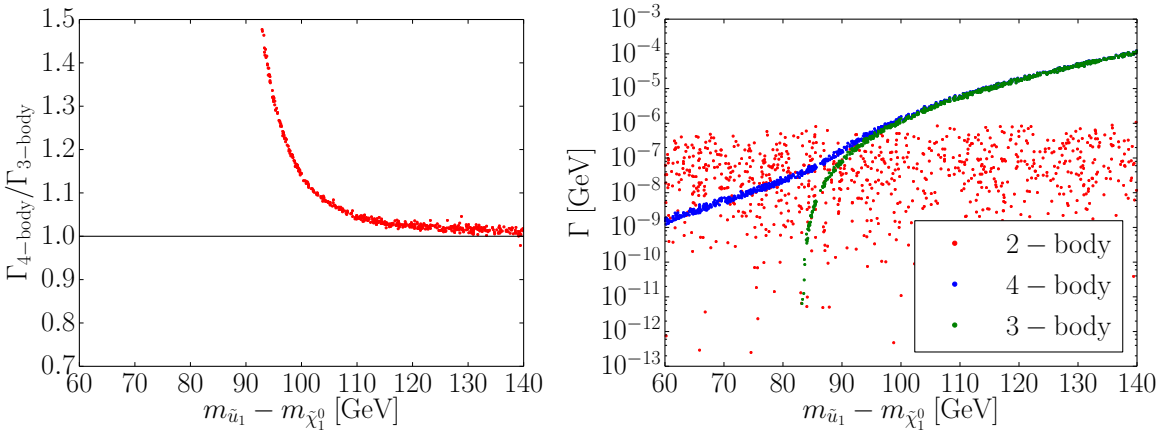

(a) Partial decay width of the four-body decay normalized to the one of the three-body decay.

(b) Partial decay widths of the two-, three- and four-body decay.

Figure 3.5: Results for the partial decay widths with respect to $\Delta m = m_{\tilde{u}_1} - m_{\tilde{\chi}_1^0}$ [21].

the mass difference Δm. Below the W threshold, only the two-body (red) and the four-body (blue) decays are possible, above the threshold additionally the three-body decay is present, depicted in green. The partial decay width for the two-body decay is scattered widely, whereas the points for the four- and three-body decays are concentrated on narrow lines. This reflects the different dependence of the decay modes on the flavor mixing: while the two-body decay being a flavor-changing neutral current decay essentially relies on the flavor-changing elements in the squark mixing matrix, the four- and three-body decays are dominated by flavor-conserving elements. In our scenarios, the size of the flavor-changing elements can vary over a large range [17], but the flavor-conserving mixing matrix elements are always of $\mathcal{O}(1)$. Furthermore, we observe that close to the threshold the two-body decay can be competitive with the other decay modes and in some cases even dominate them.
This becomes obvious in Fig. 3.6(a), where the branching ratio of the two-body decay is shown as a function of the mass difference Δm. Even 10 GeV above the W boson threshold, the branching ratio of the two-body decay can be as large as about 50%. Experimental searches in the kinematic region around the threshold require special care, since the separation of signal and background can become difficult if the decay products of the $\tilde{u}_1$ are produced nearly at rest in the rest frame of the $\tilde{u}_1$. A branching ratio of the two-body decay as large as found here can have two effects: on the one hand, exclusion bounds derived from searches in the four- or three-body decay can be loosened by the branching ratios deviating from one. On the other hand, a new search channel for the lightest up-type squark with different signature and kinematics and in consequence a different background is provided in the threshold region and above. This might lead to new discovery or exclusion prospects in the threshold region.
Finally, in Fig. 3.6(b) the results are shown in the $m_{\tilde{u}_1} - m_{\tilde{\chi}_1^0}$ plane, with the color code indicating the branching ratio of the two-body decay. The absence of parameter points for very low $m_{\tilde{u}_1}$ is due to experimental constraints, whereas for high $m_{\tilde{u}_1}$ it is caused by the limited ranges of the input parameters. We find a high branching ratio of the two-body decay close to the lower bound of the mass difference considered and a transition region where the branching ratio decreases down to zero for increasing Δm. This feature holds irrespective of the actual values of the masses of the lightest up-type squark and the neutralino. It solely

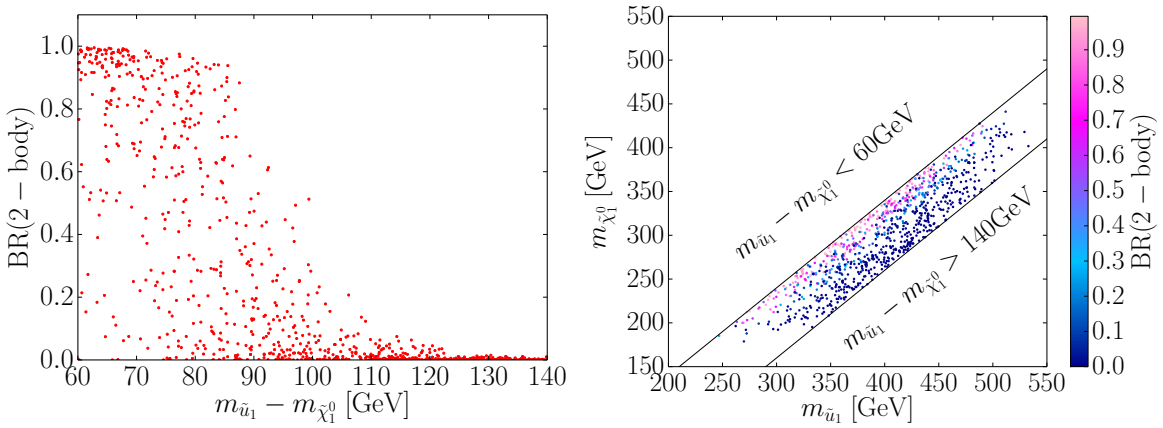

(a) Branching ratio of the two-body decay as a function of Δm.

(b) Results in the $m_{\tilde{u}_1} - m_{\tilde{\chi}_1^0}$ plane. The color code indicates the branching ratio of the two-body decay.

Figure 3.6: Relative importance of the two-body decay with respect to the four-body decay [21].

depends on the mass difference and the size of the flavor-changing elements in the squark mixing matrix as explained above.

3.4. Conclusion

The consistent calculation of the four-body decay across the W boson threshold by means of the Overall-Factor-Scheme shows, that the finite width of the W boson has a sizable effect on the partial decay width close to the threshold. Hence, for calculations of branching ratios in the investigated parameter region the four-body decay should be used rather than the three-body decay. This holds especially in view of the results for the two-body decay at the threshold, showing partial decay widths similar to the ones of the three- and four-body decay mode, which increases the importance of small effects on the branching ratios. Nevertheless, bearing in mind that the W boson can be on-shell above the threshold might be useful for reconstruction purposes. Generally, we find that the flavor mixing has strong influence on the phenomenology of the $\tilde{u}_1$ decay. Depending on the actual scenario, the branching ratios of all decay modes can vary from zero to one at the threshold, solely due to the size of the flavor-changing matrix elements in the squark mixing matrix. Hence, complementary searches have to be conducted in the two- and the four-body decay in order to cover the parameter region around the W boson threshold. Hereby a large branching ratio of the two-body decay potentially offers an alternative channel for studies in the threshold region. The impact of branching ratios deviating from one on the exclusion bounds was recently confirmed by the experimental analysis [54].

4. Squark Gluino Production with Spin Correlations at Next-to-Leading Order

In this chapter the squark gluino production is discussed. The inclusion of spin correlations is an important feature considered in this work. To this end, in Sec. 4.1 the framework is described, how this is accomplished in the combination of squark gluino production with the decay of the gluino, followed by formulae for the gluino and the squark decay at LO. In Sec. 4.2 the virtual corrections are described shortly, before focusing on the real corrections to the production process in Sec. 4.3. Finally the implementation of the calculation in the POWHEG − BOX and preliminary results are discussed in Secs. 4.4 and 4.5 before drawing a conclusion in Sec. 4.6.
If not stated otherwise, q and $\tilde{q}$ in this chapter generally denote left- and right-handed quarks and squarks of the first two generations and the quarks are treated as massless.

4.1. Framework at Leading Order

In order to combine the production and the decay of all particles in the squark gluino production the NWA as described in Sec. 2.2.1 is used. Hence, the complete process is split into three sub-processes: first, the squark gluino production $qg \longrightarrow \tilde{q}\tilde{g}$ with corresponding Feynman diagrams at leading order in Fig. 4.1(a). Second, the squark decay into a quark of the same flavor and the lightest neutralino $\tilde{q} \longrightarrow q\tilde{\chi}_1^0$ (Fig. 4.1(b)), and third the gluino decay into a squark and an antiquark of the same flavor $\tilde{g} \longrightarrow \tilde{q}\bar{q}$ (Fig. 4.1(c)). In the complete process, the squark from the gluino decay decays further. Both squarks can be either left- or right-handed. In the production and also the decays, antisquarks are considered as well, but for simplicity only the processes with squarks are shown in Fig. 4.1. These processes are calculated separately and plugged together according to Eq. (2.27) and Eq. (2.34) for the LO and the NLO case, respectively. However, naively summing over final state polarizations in the production and averaging over initial state polarizations in the decay of the gluino, spin correlations between production and decay are lost. A convenient way of maintaining them in a calculation using the NWA is given by employing helicity density matrices. In the next subsection it is shown how helicity density matrices are used in this work, based on [145]. After that, the gluino decay will be evaluated at leading order to demonstrate the procedure and its consequences by means of a short example.

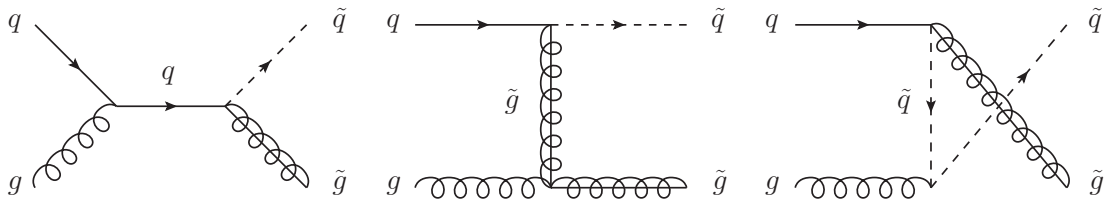

(a) Diagrams for the production sub-process $qg \longrightarrow \tilde{q}\tilde{g}$.

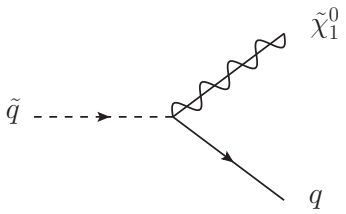

(b) Diagram for the squark decay $\tilde{q} \longrightarrow q\tilde{\chi}_1^0$.

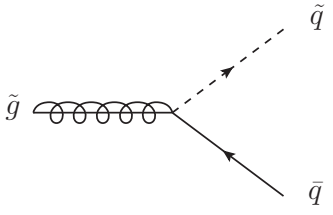

(c) Diagram for the gluino decay $\tilde{g} \longrightarrow \tilde{q}\bar{q}$.

Figure 4.1: Generic diagrams for squark gluino production and the decays of the squark and gluino at tree-level. Indices for chiralities and flavors are omitted for simplicity.

4.1.1. Helicity Density Matrices

Consider the squark gluino production at leading order where the gluino directly decays into a squark and an antiquark with a total amplitude $\mathcal{M}_{\text{tot}}$, ignoring the decays of the squarks for the moment as shown in Fig. 4.2 (i.e. before factorizing production and decay for the gluino). In order to separate the production and decay process, not only the denominator of the gluino propagator is involved according to Eq. (2.26), but also the numerator has to be factorized. In the matrix element $\mathcal{M}_{\text{tot}}$ for the diagram Fig. 4.2, the spin of the gluino is consistently transferred from the production to the decay, encoded in the numerator of the

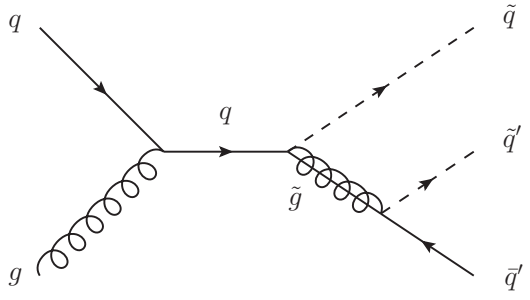

Figure 4.2: Tree-level Feynman diagram for squark gluino production with the decay of the gluino directly attached. Indices for chiralities and flavors are omitted for simplicity.

gluino propagator $\not{p}_{\tilde{g}} + m_{\tilde{g}}$. In the limit of Eq. (2.26) the total amplitude then takes the form

$$\mathcal{M}_{\text{tot}} = \mathcal{M}_{\tilde{D}}(\not{p}_{\tilde{g}} + m_{\tilde{g}})\mathcal{M}_{\tilde{P}} \ , \tag{4.1}$$

where $\mathcal{M}_{\tilde{P},\tilde{D}}$ are the remaining parts of the amplitude for the production of the squark and the gluino and the decay of the gluino. In order to factorize this expression into production and decay, the polarization sum for the gluino

$$\not{p}_{\tilde{g}} + m_{\tilde{g}} = \sum_{\lambda} u(p_{\tilde{g}}, \lambda)\bar{u}(p_{\tilde{g}}, \lambda) \tag{4.2}$$

can be used, where $u(p_{\tilde{g}}, \lambda)$ is the u-spinor for the gluino with momentum $p_{\tilde{g}}$ and helicity λ, so that

$$\mathcal{M}_{\text{tot}} = \sum_{\lambda} \mathcal{M}_{\tilde{D}} u(p_{\tilde{g}}, \lambda)\bar{u}(p_{\tilde{g}}, \lambda)\mathcal{M}_{\tilde{P}} \ . \tag{4.3}$$

Identifying

$$\mathcal{M}_{\tilde{D}} u(p_{\tilde{g}}, \lambda) = \mathcal{M}_{D,\lambda} \tag{4.4}$$

and

$$\bar{u}(p_{\tilde{g}}, \lambda)\mathcal{M}_{\tilde{P}} = \mathcal{M}_{P,\lambda} \ , \tag{4.5}$$

where $\mathcal{M}_{P(D),\lambda}$ is the stand-alone matrix element for the production (decay) of the gluino with helicity λ, we obtain

$$\mathcal{M}_{\text{tot}} = \sum_{\lambda} \mathcal{M}_{D,\lambda}\mathcal{M}_{P,\lambda} \ . \tag{4.6}$$

The amplitude squared then reads

$$|\mathcal{M}_{\text{tot}}|^2 = \sum_{\lambda} \mathcal{M}_{D,\lambda}\mathcal{M}_{P,\lambda} \sum_{\lambda'} \mathcal{M}^{\dagger}_{P,\lambda'}\mathcal{M}^{\dagger}_{D,\lambda'} \tag{4.7a}$$

$$= \sum_{\lambda,\lambda'} \underbrace{\mathcal{M}^{\dagger}_{D,\lambda'}\mathcal{M}_{D,\lambda}}\underbrace{\mathcal{M}_{P,\lambda}\mathcal{M}^{\dagger}_{P,\lambda'}} \tag{4.7b}$$

$$= \sum_{\lambda,\lambda'} \quad (\rho_D)_{\lambda',\lambda} \qquad (\rho_P)_{\lambda,\lambda'} \tag{4.7c}$$

$$= \text{Tr}\{\rho_P \rho_D\} \ , \tag{4.7d}$$

which defines the helicity density matrices for the production (decay) of the gluino $\rho_{P(D)}$. It is the coherent sum over the gluino helicities in production and decay in Eq. (4.6) and its representation via the matrix product and the trace in Eq. (4.7d) which retains the spin correlations. As shown in [145] an explicit evaluation of Eq. (4.7d) yields

$$|\mathcal{M}_{\text{tot}}|^2 = \frac{1}{2}|\mathcal{M}_{P,0}|^2|\mathcal{M}_{D,0}|^2 \left(1 + P^{\mu}\left(-g_{\mu\nu} + \frac{p_{\tilde{g}\mu}p_{\tilde{g}\nu}}{m^2_{\tilde{g}}}\right)D^{\nu}\right) \ , \tag{4.8}$$

where $\mathcal{M}_{P(D),0}$ and $P^{\mu}(D^{\mu})$ are the spin independent and spin dependent parts of the amplitude for the production (decay), respectively. These are defined by

$$|\mathcal{M}_{P,\lambda}|^2 = \frac{1}{2}|\mathcal{M}_{P,0}|^2 \left(1 + s^{(\lambda)}_{\mu} P^{\mu}\right) \ , \tag{4.9a}$$

$$|\mathcal{M}_{D,\lambda}|^2 = \frac{1}{2}|\mathcal{M}_{D,0}|^2 \left(1 + s^{(\lambda)}_{\mu} D^{\mu}\right) \ , \tag{4.9b}$$

where $s_\mu^{(\lambda)}$ is the spin-four-vector corresponding to the spin of the gluino with helicity λ. These formulations of the amplitudes for production and decay can be obtained through projection on the gluino helicity by [145]

$$u(p_{\tilde{g}},\lambda)\bar{u}(p_{\tilde{g}},\lambda) = \frac{1}{2}\left(1+\gamma_5 \not{s}^{(\lambda)}\right)(\not{p}_{\tilde{g}} + m_{\tilde{g}}) \ , \tag{4.10}$$

instead of summing over the helicities. At NLO, the total matrix element squared is still determined by Eq. (4.8), but all ingredients have to be determined at NLO. Also in the virtual and real corrections the separation into a spin independent part and a spin dependent part has to be done[9]. Since the amplitudes squared for the production including the spin dependence are rather lengthy, no explicit formulae are provided here. Instead, explicit relations with respect to the spin dependence for the gluino decay at LO are provided in the next section.

4.1.2. Gluino Decay at Leading Order

It is instructive to see the application of Eqs. (4.8)-(4.10) in practice by the example of an amplitude at tree-level. For simplicity, consider the amplitude squared for the decay of a gluino into a left-handed squark $\tilde{q}_L$ and an antiquark $\bar{q}$ corresponding to the diagram Fig. 4.1(c)

$$\sum_{\lambda_{\bar{q}}} |\mathcal{M}_{\tilde{g}\to\tilde{q}_L\bar{q}}|^2 = g_s^2\left((p_{\tilde{g}}p_{\bar{q}}) - m_{\tilde{g}}(p_{\bar{q}}s^{(\lambda)})\right) \ , \tag{4.11}$$

where g_s is the strong gauge coupling and $p_{\bar{q}}$ the four-momentum of the antiquark. The sum indicates that it has already been summed over the helicities of the final state antiquark $\lambda_{\bar{q}}$. On the other hand it is not summed over the gluino helicities, but the projection Eq. (4.10) has been used. This amplitude squared can now be split up into the spin dependent and spin independent part according to Eq. (4.9b), resulting in

$$|\mathcal{M}_{D,0}|^2 = 2g_s^2(p_{\tilde{g}}p_{\bar{q}}) \ , \tag{4.12a}$$

$$D^\mu = -\frac{m_{\tilde{g}}}{(p_{\tilde{g}}p_{\bar{q}})}p_{\bar{q}}^\mu \ . \tag{4.12b}$$

After computing the amplitude squared for the squark gluino production similarly, the combination of production and decay Eq. (4.8) is obtained by replacing the spin-vector in Eq. (4.9a) by

$$s_\mu^{(\lambda)} \longrightarrow \left(-g_{\mu\nu} + \frac{p_{\tilde{g}\mu}p_{\tilde{g}\nu}}{m_{\tilde{g}}^2}\right)D^\nu \ , \tag{4.13}$$

where D^ν is determined by Eq. (4.12b), and multiplying the result by $|\mathcal{M}_{D,0}|^2$ given by Eq. (4.12a). The result for the spin dependent part Eq. (4.12b) also holds when the gluino decays into a right-handed antisquark. On the other hand, if it decays into a right-handed squark, or a left-handed antisquark, the spin dependent part Eq. (4.12b) changes sign.
In order to understand the effect of incorporating the spin dependence in the calculation consider the matrix element squared Eq. (4.11) in the rest frame of the gluino: choosing the spin of the gluino as axis such that θ is the angle between the three-momentum of the

[9] In an implementation based on helicity amplitudes, rather than on analytic amplitudes squared, calculating the total amplitude squared by a direct evaluation of Eq. (4.7d) can be more convenient than using Eq. (4.8). In this work, analytic amplitudes squared are used for reasons given in Sec. 4.3.1.

antiquark and the space-components of the spin vector, the second scalar product of Eq. (4.11) for a massless antiquark with energy $E_{\bar{q}}$ reads

$$(p_{\bar{q}} s^{(\lambda)}) = -E_{\bar{q}} \cos\theta \ , \tag{4.14}$$

since the time-component of the spin vector vanishes in the rest frame of the gluino [145]. Then Eq. (4.11) simplifies to

$$\sum_{\lambda_{\bar{q}}} |\mathcal{M}_{\tilde{g}\to\tilde{q}_L\bar{q}}|^2 = g_s^2 m_{\tilde{g}} E_{\bar{q}} (1+\cos\theta) \ . \tag{4.15}$$

The effect of the spin dependence explicitly taken into account is now solely contained in the second term $\cos\theta$ and leads to the following findings: the spin-contribution has no impact on the total decay width, since in this case the matrix element squared is integrated over the complete range of $\cos\theta$ such that the second term has no effect as it is linear in $\cos\theta$. By contrast, the second term leads to an angular modulation of the differential decay width proportional to $\cos\theta$. This observation holds more generally: spin correlations do not affect branching ratios and total cross sections, but influence kinematic distributions.

4.1.3. Squark Decay at Leading Order

The partial decay width for the squark decay $\tilde{q} \longrightarrow q\tilde{\chi}_1^0$, where the squark can be either left- or right-handed and of any light flavor is well known in the literature [146]. For the implementation in the `POWHEG − BOX` the matrix element squared has to be separated from the flux factor and the phase space. The only Feynman diagram contributing to the decay at LO is shown in Fig. 4.1(b). The corresponding matrix element squared for a massless quark in the final state, summed over the quark and neutralino helicities λ_q and $\lambda_{\tilde{\chi}}$, is given by

$$\sum_{\lambda_q\lambda_{\tilde{\chi}}} |\mathcal{M}_{\tilde{q}\to q\tilde{\chi}_1^0}|^2 = 4\pi\alpha m_{\tilde{q}}^2 \left(1 - \frac{m_{\tilde{\chi}_1^0}^2}{m_{\tilde{q}}^2}\right) f_{L/R}^2 \ , \tag{4.16}$$

where α is the electroweak fine-structure constant, $m_{\tilde{q}}$ and $m_{\tilde{\chi}_1^0}$ are the masses of the squark and the lightest neutralino, respectively. The factor $f_{L/R}$ has to be chosen according to the chirality of the squark,

$$f_L = \sqrt{2}\left[e_q N'_{11} + (I_3^q - e_q s_W^2)\frac{1}{s_W c_W} N'_{12}\right] \ , \tag{4.17}$$

$$f_R = -\sqrt{2}\left[e_q N'_{11} - e_q \frac{s_W}{c_W} N'_{12}\right] \ . \tag{4.18}$$

In the above equations e_q is the charge of the quark q in units of the elementary charge, I_3^q is the third component of the isospin of the quark q and N'_{11} and N'_{12} are given by

$$N'_{11} = c_W N_{11} + s_W N_{12} \ , \tag{4.19}$$

$$N'_{12} = -s_W N_{11} + c_W N_{12} \ , \tag{4.20}$$

where N_{11} and N_{12} are elements of the neutralino mixing matrix and $s_W = \sin\theta_W$ and $c_W = \cos\theta_W$ with θ_W being the weak mixing angle. As the squark is a scalar particle its decay is isotropic and is not involved in the spin correlations.

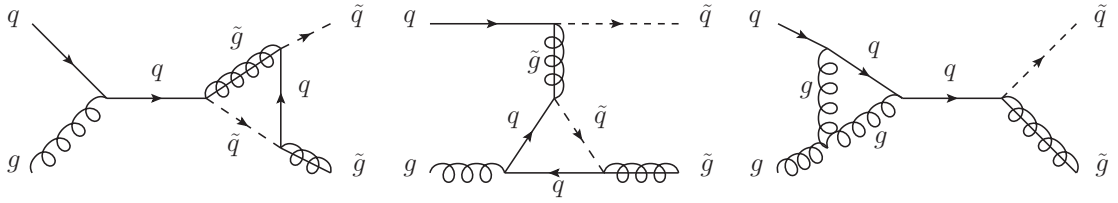

(a) Example diagrams for triangle contributions.

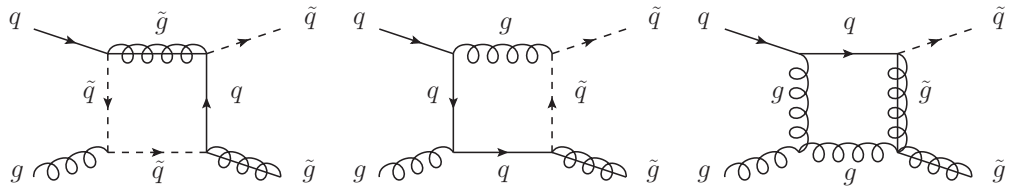

(b) Example diagrams for box contributions.

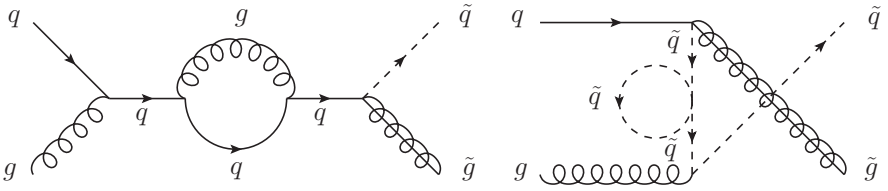

(c) Example diagrams for self-energy contributions.

Figure 4.3: Example diagrams for virtual contributions to squark gluino production at the one-loop level. Indices indicating chiralities or flavors have been omitted for better readability.

4.2. Virtual Corrections

The virtual corrections have been calculated using the program packages `FeynArts` [147] and `FormCalc` [148] by another team member, and will be explained here only briefly. Examples for the three different types of virtual contributions are shown in Fig. 4.3. The corrections consist of triangle and box contributions like Fig. 4.3(a) and Fig. 4.3(b), respectively, and self-energy diagrams similar to the ones shown in Fig. 4.3(c). The regularization and renormalization has been performed similarly to [149]. The divergences have been regularized by dimensional regularization and in consequence a SUSY-restoring counterterm [25]

$$\delta\hat{g}_s = \delta g_s + \frac{\alpha_s}{3\pi} \ , \tag{4.21}$$

where $\hat{g}_s$ is the Yukawa coupling present in the squark quark gluino vertex and g_s is the strong gauge coupling, has been introduced for compatibility with supersymmetry. The renormalization of the quark, squark and gluino fields and masses is performed in the on-shell scheme, whereas the strong gauge coupling is renormalized in the $\overline{\text{MS}}$ scheme with five active flavors. For details, see [149].
The spin correlations for the gluino included in this work can be incorporated in the Fortran code for the one-loop corrections generated by `FormCalc` in a convenient way: in the sum over helicities of the gluino performed in the code, a replacement similar to Eq. (4.13) can be made.

4.3. Real Corrections

The computation of the real corrections to squark gluino production is a key ingredient to the NLO corrections to squark gluino production including spin correlations. As will be explained in detail in Secs. 4.3.1 and 4.3.2 care has to be taken in the calculation due to intermediate resonances and fermion-number-violating interactions. Issues connected to gauge invariance of the amplitudes are discussed in Sec. 4.3.3.

4.3.1. On-Shell Subtraction

The real corrections to squark gluino production result from radiation of a gluon or a massless quark. Consequently, the real corrections to the production of a left-handed squark with flavor i, $\tilde{q}_{iL}$, and a gluino from a quark q_i and a gluon, $q_i g \longrightarrow \tilde{q}_{iL}\tilde{g}$, consist of the sub-processes

$$q_i + g \longrightarrow \tilde{q}_{iL} + \tilde{g} + g \ , \tag{4.22}$$
$$g + g \longrightarrow \tilde{q}_{iL} + \tilde{g} + \bar{q}_i \ , \tag{4.23}$$
$$q_i + \bar{q}_i \longrightarrow \tilde{q}_{iL} + \tilde{g} + \bar{q}_i \ , \tag{4.24}$$
$$q_i + q_i \longrightarrow \tilde{q}_{iL} + \tilde{g} + q_i \ , \tag{4.25}$$
$$q_i + \bar{q}_j \longrightarrow \tilde{q}_{iL} + \tilde{g} + \bar{q}_j \ , \quad i \neq j \ , \tag{4.26}$$
$$q_i + q_j \longrightarrow \tilde{q}_{iL} + \tilde{g} + q_j \ , \quad i \neq j \ , \tag{4.27}$$
$$q_j + \bar{q}_j \longrightarrow \tilde{q}_{iL} + \tilde{g} + \bar{q}_i \ , \quad i \neq j \ . \tag{4.28}$$

The flavor indices indicate, that the quark or squark is of flavor i or j, respectively, where $i, j = u, d, s, c$. The corresponding sub-processes for producing a right-handed squark $\tilde{q}_{iR}$ are the same and the channels for antisquarks are obtained by replacing quarks and squarks by their respective antiparticles. The channels Eq. (4.22) and Eq. (4.23) are related by crossing symmetry, as well as the channels Eq. (4.24) and Eq. (4.25). The channel Eq. (4.26)

comprises only the subset of diagrams of channel Eq. (4.24), where the two initial quarks are disconnected in flavor space, channel Eq. (4.27) is obtained via crossing from Eq. (4.26). The last channel Eq. (4.28) is the disjoint subset of the diagrams of channel Eq. (4.24) in comparison to the subset needed for channel Eq. (4.26), i.e. all diagrams from Eq. (4.24) where the initial quarks are connected in flavor space[10]. Hence, in the calculation only the channels Eq. (4.23) and Eq. (4.24) were calculated explicitly and all others were derived as described above. The Feynman diagrams for the gluon gluon channel Eq. (4.23) are presented in Fig. 4.4. In Fig. 4.4(a) the diagrams with an intermediate gluino resonance are collected, in Fig. 4.4(b) the diagrams with an intermediate squark resonance, and the diagrams depicted in Fig. 4.4(c) do not involve any intermediate resonance. The Feynman diagrams for the quark antiquark channel Eq. (4.24) are shown in Fig. 4.5. Analogous to the case of the gluon gluon channel also here a classification into diagrams with an intermediate gluino resonance in Fig. 4.5(a), diagrams with intermediate squark resonance Fig. 4.5(b), and diagrams without any resonance in Fig. 4.5(c) has been made. An important feature of the quark antiquark channel is that there are diagrams involving an intermediate squark whose chirality is independent of the chirality of the external squark. This is the case for the diagrams $\mathcal{M}_2$ - $\mathcal{M}_5$ in Fig. 4.5(a), for the diagrams $\mathcal{M}_7$ and $\mathcal{M}_8$ of Fig. 4.5(b), and for the diagrams $\mathcal{M}_{10}$ and $\mathcal{M}_{11}$ of Fig. 4.5(c). Consequences of this will be discussed in Sec. 4.3.2.

The intermediate resonances present in Figs. 4.4(a), 4.4(b), 4.5(a) and 4.5(b) are problematic if the kinematic situation allows for the intermediate particle to be on its mass shell. For instance, the intermediate gluino in $\mathcal{M}_1$ of Fig. 4.4(a) can be on-shell (OS) if $m_{\tilde{q}_{iL}} < m_{\tilde{g}}$ and if the center-of-mass energy allows for the production of two OS gluinos. In this case, the gluino propagator becomes divergent, which is why these divergences are called on-shell singularities (OSS). From a different point of view, this OS resonance can be regarded as gluino pair production, followed by the decay of one gluino at leading order. The resonant contribution is hence already taken into account in the calculation for gluino pair production. In order to avoid double counting of this contribution, it has to be subtracted properly in the calculation of squark gluino production. Similar OS contributions which are already taken into account in the calculation of different production processes arise also from OS squarks, and are present for all channels of the real corrections except the quark gluon channel Eq. (4.22). The OSS occurring in the production of a left-handed squark $\tilde{q}_{iL}$ and a gluino are summarized in Tab. 4.1. While the channel is indicated in the first column, in the second column the process that already covers the resonant contribution is stated. In the third column the diagrams developing the OSS are listed. For OSS stated in channels derived by crossing, the diagrams are those which develop an OSS *after* crossing. In the last column the kinematic constraint is provided, which decides on whether the OSS can develop or not. Apparently there can be OSS stemming from gluino pair production ($\tilde{g}\tilde{g}$ production), squark pair production of same flavors and chiralities ($\tilde{q}_{iL}\tilde{q}_{iL}$ production), squark antisquark production of same flavor and chiralities ($\tilde{q}_{iL}\tilde{q}^*_{iL}$ production) and the corresponding channels for mixed flavors and chiralities.

The occurrence of these OSS is not a unique feature of squark gluino production but has been studied already for tW production in the SM [150, 151], for the production of neutralinos and charginos [152] or squarks and gluinos [25, 31, 34, 35]. The existing methods for subtracting the OS contributions used in these works on the one hand differ in how a regulator is introduced to the resonant amplitudes in order to regularize the singularities and on the other hand they subtract different contributions. In [34] and [149] a detailed analysis of existing methods has been performed, together with the proposal for a new procedure to treat the

[10] Alternatively, channel Eq. (4.28) can also be obtained from channel Eq. (4.27) by crossing.

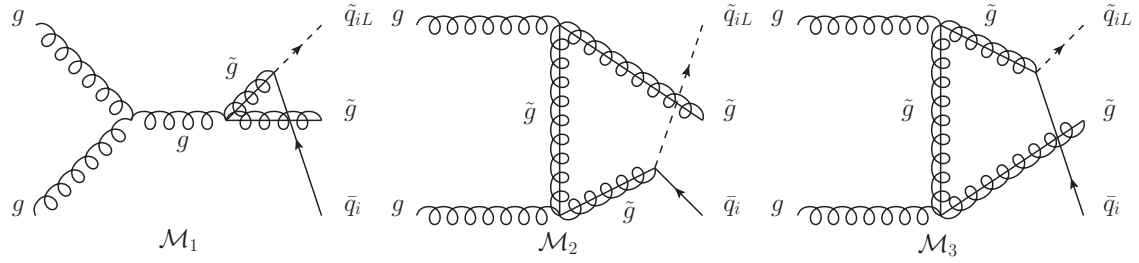

(a) Diagrams with intermediate gluino resonance.

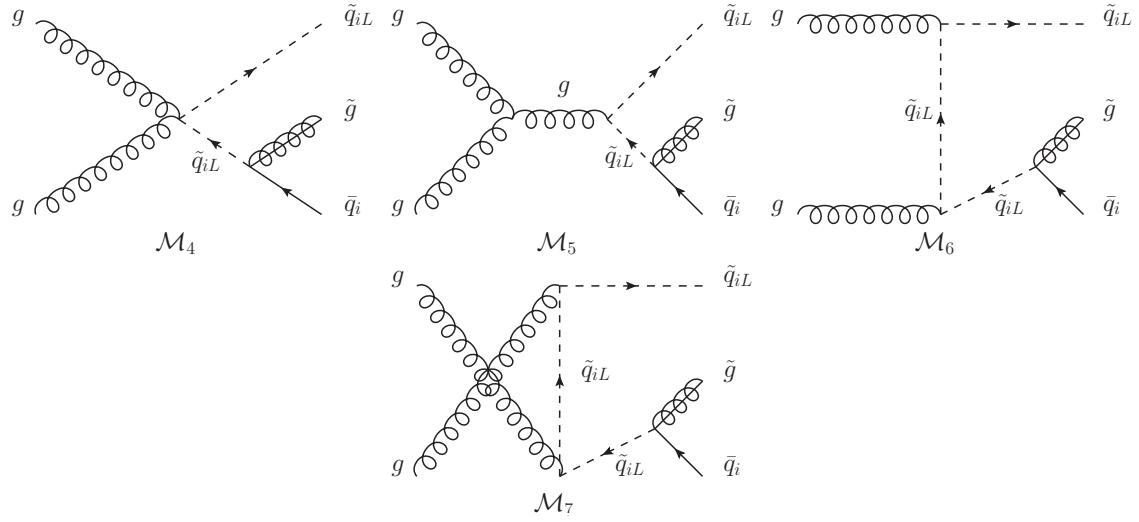

(b) Diagrams with intermediate squark resonance.

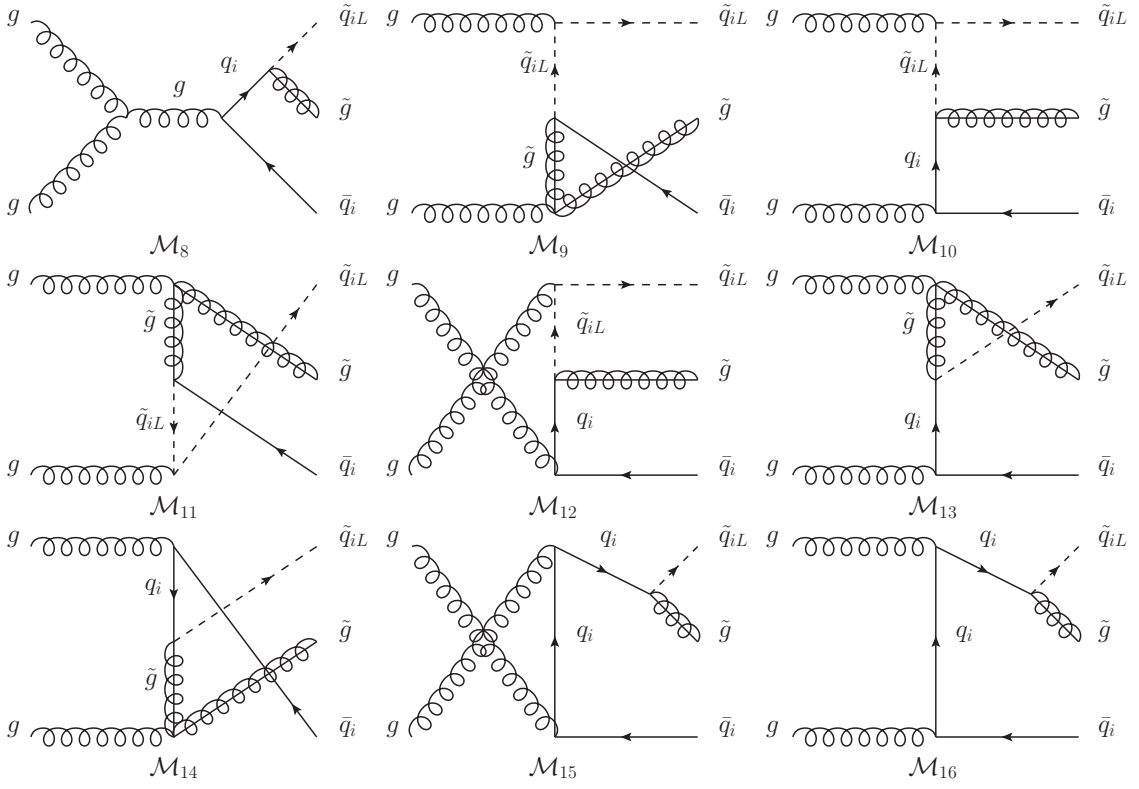

(c) Diagrams without intermediate resonance.

Figure 4.4: Feynman diagrams contributing to the sub-process $g + g \longrightarrow \tilde{q}_{iL} + \tilde{g} + \bar{q}_i$, Eq. (4.23), of the real corrections to squark gluino production.

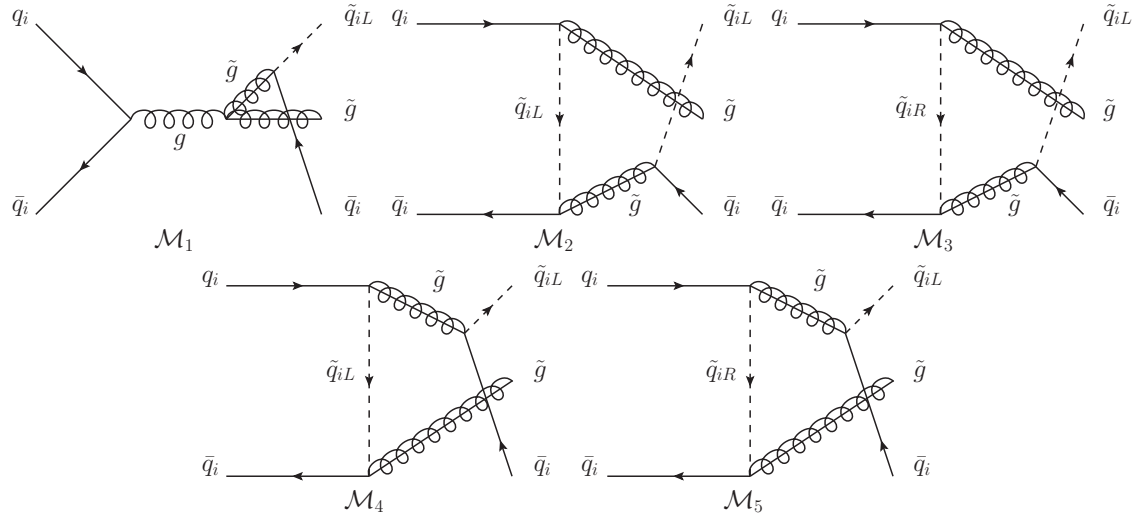

(a) Diagrams with intermediate gluino resonance.

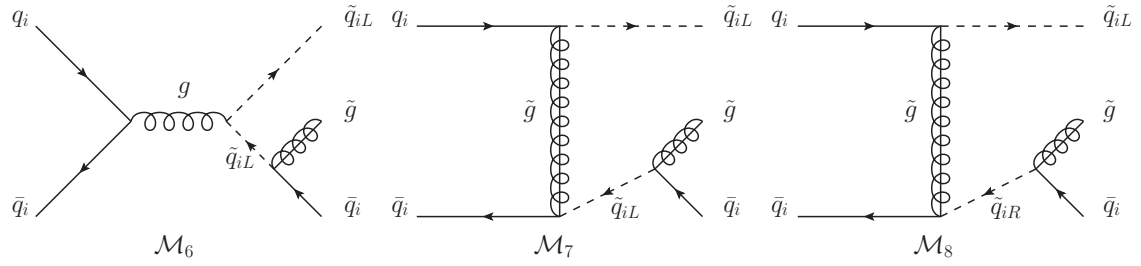

(b) Diagrams with intermediate squark resonance.

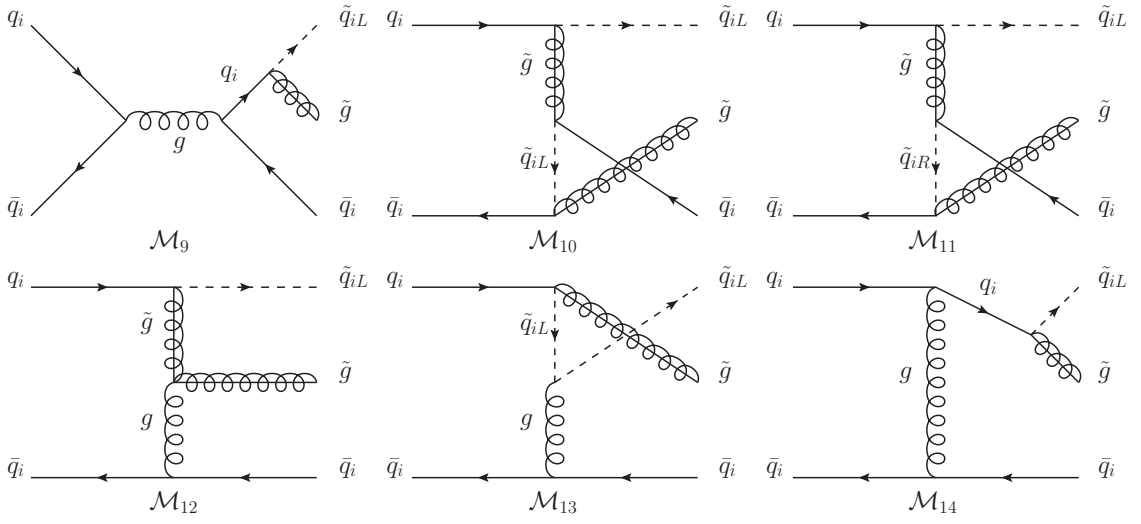

(c) Diagrams without intermediate resonance.

Figure 4.5: Feynman diagrams contributing to the sub-process $q_i + \bar{q}_i \longrightarrow \tilde{q}_{iL} + \tilde{g} + \bar{q}_i$, Eq. (4.24), of the real corrections to squark gluino production.

Channel	OSS stemming from	Diagrams	Kinematic Constraint
Eq. (4.23): $g + g$	$\tilde{q}_{iL}\tilde{q}^*_{iL}$ production	4, 5, 6, 7	$m_{\tilde{g}} < m_{\tilde{q}_{iL}}$
	$\tilde{g}\tilde{g}$ production	1, 2, 3	$m_{\tilde{q}_{iL}} < m_{\tilde{g}}$
Eq. (4.24): $q_i + \bar{q}_i$	$\tilde{g}\tilde{g}$ production	1, 2, 3, 4, 5	$m_{\tilde{q}_{iL}} < m_{\tilde{g}}$
	$\tilde{q}_{iL}\tilde{q}^*_{iL}$ production	6, 7	$m_{\tilde{g}} < m_{\tilde{q}_{iL}}$
	$\tilde{q}_{iL}\tilde{q}^*_{iR}$ production	8	$m_{\tilde{g}} < m_{\tilde{q}_{iR}}$
Eq. (4.25): $q_i + q_i$	$\tilde{q}_{iL}\tilde{q}_{iL}$ production	4,10	$m_{\tilde{g}} < m_{\tilde{q}_{iL}}$
	$\tilde{q}_{iL}\tilde{q}_{iR}$ production	5,11	$m_{\tilde{g}} < m_{\tilde{q}_{iR}}$
Eq. (4.26): $q_i + \bar{q}_j$	$\tilde{q}_{iL}\tilde{q}^*_{jL}$ production	7	$m_{\tilde{g}} < m_{\tilde{q}_{jL}}$
	$\tilde{q}_{iL}\tilde{q}^*_{jR}$ production	8	$m_{\tilde{g}} < m_{\tilde{q}_{jR}}$
Eq. (4.27): $q_i + q_j$	$\tilde{q}_{iL}\tilde{q}_{jL}$ production	10	$m_{\tilde{g}} < m_{\tilde{q}_{jL}}$
	$\tilde{q}_{iL}\tilde{q}_{jR}$ production	11	$m_{\tilde{g}} < m_{\tilde{q}_{jR}}$
Eq. (4.28): $q_j + \bar{q}_j$	$\tilde{g}\tilde{g}$ production	1, 2, 3, 4, 5	$m_{\tilde{q}_{iL}} < m_{\tilde{g}}$
	$\tilde{q}_{iL}\tilde{q}^*_{iL}$ production	6	$m_{\tilde{g}} < m_{\tilde{q}_{iL}}$

Table 4.1: Overview of OSS in the real corrections to $\tilde{q}_{iL}\tilde{g}$-production. The diagram numbers refer to the numbers indicated in Fig. 4.4 for the gluon gluon channel and to Fig. 4.5 for the other channels.

OSS. For convenience, the major facts are summarized in the following.
In general, the amplitude for a specific channel of the real corrections to squark gluino production $\mathcal{M}_{\text{tot}}$ can always be decomposed as

$$\mathcal{M}_{\text{tot}} = \mathcal{M}_{\text{r}} + \mathcal{M}_{\text{nr}} \ , \tag{4.29}$$

where $\mathcal{M}_{\text{r}}$ comprises all diagrams which develop an OSS and other diagrams are collected in $\mathcal{M}_{\text{nr}}$. Following [149], the different methods can then be classified as follows:

- Diagram Removal Type I (DRI): this method amounts to neglecting all resonant diagrams, such that $|\mathcal{M}_{\text{tot}}|^2 = |\mathcal{M}_{\text{nr}}|^2$.
- Diagram Removal Type II (DRII): in this case the interference terms of resonant and non-resonant contributions are kept as well, so $|\mathcal{M}_{\text{tot}}|^2 = |\mathcal{M}_{\text{nr}}|^2 + 2\text{Re}(\mathcal{M}_{\text{nr}}\mathcal{M}^*_{\text{r}})$.
- Diagram Subtraction (DS): here, a counterterm is constructed which subtracts only the resonant part of the amplitude pointwise in phase space but retains off-shell contributions from $|\mathcal{M}_{\text{r}}|^2$. To that end, a regulator Γ_{reg} is introduced to the resonant amplitudes. For the counterterm the original momenta of the particles are remapped to a kinematic configuration where the intermediate particle is OS via a Catani-Seymour remapping [153]. The counterterm then subtracts from the total amplitude the contribution resulting from the resonant amplitudes evaluated at the remapped configuration.

The first two methods DRI and DRII spoil gauge invariance since they only take into account a subset of diagrams, or neglect parts of the amplitude squared. Whether the DS method is gauge-invariant or not depends on how the regulator is introduced. In [31, 152] the regulator is introduced at the amplitude level by replacing the denominator of the propagator that

leads to the singularity by

$$(p_{\tilde{q}_{iL}} + p_{\bar{q}_i})^2 - m_{\tilde{g}}^2 \longrightarrow (p_{\tilde{q}_{iL}} + p_{\bar{q}_i})^2 - m_{\tilde{g}}^2 + \mathrm{i} m_{\tilde{g}} \Gamma_{\mathrm{reg}} \tag{4.30}$$

for the example of the gluino resonance present for instance in the diagrams of Fig. 4.4(a), where $p_{\tilde{q}_{iL}}$ and $p_{\bar{q}_i}$ are the momenta of the external squark and antiquark, respectively[11]. This variant is, however, not gauge-invariant for $\Gamma_{\mathrm{reg}} \neq 0$, but only in the limit $\Gamma_{\mathrm{reg}} \to 0$. A fully gauge-invariant OS subtraction scheme, called DS*, has been pioneered in [34, 35, 149]. Here, the regulator is introduced at the amplitude squared level after expanding the entire amplitude in a non-redundant set of kinematic invariants. This is motivated by the fact, that each type of OSS always develops in a single kinematic invariant, defined by the denominator of the propagator developing the OSS. Namely, the gluino resonance in the real corrections Eq. (4.23) and Eq. (4.24) always develops in the invariant

$$d_{\tilde{g}} = (p_{\tilde{q}_{iL}} + p_{\bar{q}_i})^2 - m_{\tilde{g}}^2 \tag{4.31}$$

in the limit $d_{\tilde{g}} \to 0$. Expanding the entire amplitude squared in this invariant results in a power series, where each order is independently gauge-invariant [34, 149]. The difference between the DS and DS* method is that the term of $\mathcal{O}(d_{\tilde{g}}^{-2})$ in the expansion is not necessarily the same as $|\mathcal{M}_{\mathrm{r}}|^2$, which is used to determine the counterterm in the DS method. This is the case if the numerator of $|\mathcal{M}_{\mathrm{r}}|^2$ contains an implicit dependence on $d_{\tilde{g}}$, for example brought about by scalar products like

$$(p_{\tilde{q}_{iL}} p_{\bar{q}_i}) = \frac{1}{2}(d_{\tilde{g}} + m_{\tilde{g}}^2 - m_{\tilde{q}_{iL}}^2) \ , \tag{4.32}$$

where $m_{\tilde{q}_{iL}}$ is the mass of the squark $\tilde{q}_{iL}$. Then $|\mathcal{M}_{\mathrm{r}}|^2$ implicitly contains terms of $\mathcal{O}(d_{\tilde{g}}^{-1})$. Introducing the regulator not at the amplitude level, but at the amplitude squared level and constructing the counterterm from the term of $\mathcal{O}(d_{\tilde{g}}^{-2})$ in the proper expansion in the invariant $d_{\tilde{g}}$ preserves gauge invariance [34, 149].

In order to make the gauge-invariant method DS* applicable, analytic amplitudes squared are required to allow for the expansion in kinematic invariants. To that end, the calculation of the amplitudes squared for the real corrections to squark gluino production has been performed by hand and traces of γ-matrices have been evaluated using `FeynCalc` [154]. The spin dependence of the amplitudes has been taken into account similarly to the case at leading order described in Sec. 4.1.

4.3.2. Left- and Right-Handed Squarks and Fermion-Number-Violating Interactions

Since the calculation of the amplitudes squared including the spin dependence by hand provides many sources of mistakes and hence requires diligence, it is convenient to reduce the number of amplitudes which have to be calculated to a minimum amount. Hence only the channels Eq. (4.23) and Eq. (4.24) were calculated and all other channels have been obtained via subsets of diagrams and crossing symmetry as stated in 4.3.1. While from Sec. 4.1.2 one could conclude that it is sufficient to calculate the amplitude squared for producing a left-handed squark and to obtain the amplitude for a right-handed squark by changing the sign of the spin dependent part, this is not true in general for the real corrections.
In order to clarify this, consider the subset $\mathcal{M}_2$, $\mathcal{M}_3$, $\mathcal{M}_6$, $\mathcal{M}_{10}$, $\mathcal{M}_{11}$ of the diagrams in Fig. 4.5. According to the projection operators at the squark quark gluino vertices it can be figured out, which helicities of the external quarks contribute to the amplitude, leading to the results shown in Tab. 4.2. Since $\bar{u}(p,\lambda)u(p,\lambda') \propto \delta_{\lambda\lambda'}$ there is no interference between

[11] Note, that intentionally not the physical width of the gluino is inserted, but a regulator width Γ_{reg}.

Diagram	Helicity of initial q_i	Helicity of initial $\bar{q}_i$	Helicity of final $\bar{q}_i$
$\mathcal{M}_2$	-	+	+
$\mathcal{M}_3$	+	-	+
$\mathcal{M}_6$	0	0	+
$\mathcal{M}_{10}$	-	+	+
$\mathcal{M}_{11}$	-	-	-

Table 4.2: Helicities of the external quarks contributing to the amplitude for the diagrams indicated in the first column for the process $q_i + \bar{q}_i \longrightarrow \tilde{q}_{iL} + \tilde{g} + \bar{q}_i$, Eq (4.24). A '+/−' means positive/negative helicity, a '0' means that both contribute. For massless quarks holds $u(p,\lambda) = v(p,-\lambda)$ [145].

Diagram	Helicity of initial q_i	Helicity of initial $\bar{q}_i$	Helicity of final $\bar{q}_i$
$\mathcal{M}_2$	-	+	-
$\mathcal{M}_3$	+	-	-
$\mathcal{M}_6$	0	0	-
$\mathcal{M}_{10}$	+	+	+
$\mathcal{M}_{11}$	+	-	-

Table 4.3: Helicities of the external quarks contributing to the amplitude for the diagrams indicated in the first column for the process $q_i + \bar{q}_i \longrightarrow \tilde{q}_{iR} + \tilde{g} + \bar{q}_i$, which is the process corresponding to Eq. (4.24) with a right-handed squark. A '+/−' means positive/negative helicity, a '0' means that both contribute. For massless quarks holds $u(p,\lambda) = v(p,-\lambda)$ [145].

diagrams with different helicities. As a consequence the interference terms $\mathcal{M}_2\mathcal{M}_6^*$, $\mathcal{M}_3\mathcal{M}_6^*$ and $\mathcal{M}_6\mathcal{M}_{10}^*$ are non-zero, whereas $\mathcal{M}_6\mathcal{M}_{11}^* = 0$. Similarly there is no interference between diagrams 10 and 11, and between 2 and 3, but $\mathcal{M}_2\mathcal{M}_{10}^* \neq 0$. Likewise all different combinations of diagrams can be analyzed on their helicity structure to see how they contribute to the process. For comparison, consider the helicities of these diagrams, when a right-handed squark is produced instead of a left-handed one in Tab. 4.3. Here, for each amplitude one helicity has changed with respect to the ones for the $\tilde{q}_{iL}$, resulting in different vanishing or non-vanishing combinations: in contrast to the $\tilde{q}_{iL}$ case now $\mathcal{M}_6\mathcal{M}_{10}^* = 0$ but $\mathcal{M}_6\mathcal{M}_{11}^* \neq 0$. The interference between diagram 2 and 10 is still present though. In total this shows that depending on the chirality of the external squark different interference terms contribute. However, it is not true, that always only one type of internal squarks gives non-vanishing contributions so that a simple replacement of $L \leftrightarrow R$ could be executed in the amplitudes, but both contribute in separate interferences. In general the left- and right-handed squarks are not degenerate in mass and hence the propagator of a left-handed squark is not equal to the one of a right-handed squark. This renders the total amplitude and in particular its spin dependent part different if a right-handed squark is produced instead of a left-handed one. Only in the limit of degenerate squark masses the difference reduces to a global sign of the spin dependent part as seen at leading order in the gluino decay. Producing a left-handed

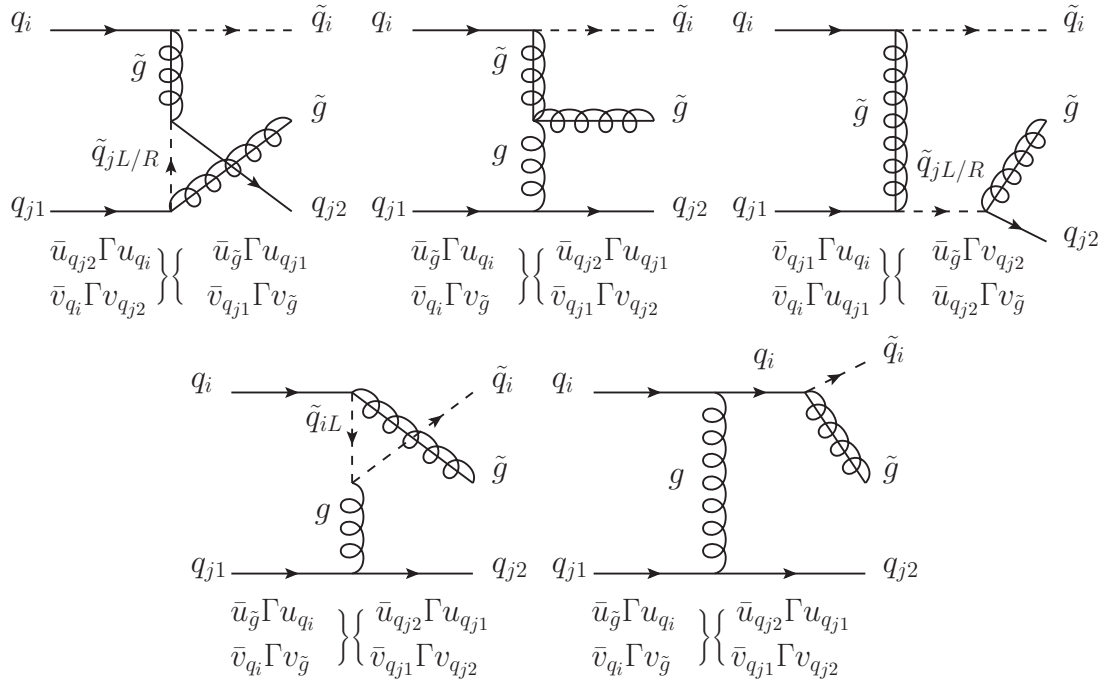

Figure 4.6: Diagrams for the sub-process $q_i + q_{j1} \longrightarrow \tilde{q}_{iL} + \tilde{g} + q_{j2}$. The diagrams differing only in the chirality of the internal squark are collected and different spinor combinations for the external fermions according to the orientation of the fermion flows are provided below the diagrams.

antisquark instead of a squark results in the same pattern as indicated in Tab. 4.2, but with opposite helicities. Hence the analytical structure of the amplitude squared is equal to the one for a squark, but the overall change of helicities translates into the opposite helicity of the gluino being projected out. The net effect is that the spin dependent part changes sign with respect to the amplitude squared for a squark. The same holds for the transition from a right-handed squark to a right-handed antisquark. At leading order and for the channels Eq. (4.22) and Eq. (4.23) this complication does not occur, since there exists only one single fermion chain and no internal squark whose chirality is detached from the chirality of the external squark.

Due to the Majorana nature of the gluino the squark quark gluino vertex is a fermion-number-violating interaction. Feynman rules for fermion-number-violating interactions have been derived in [155, 156] and have to be applied here. This amounts to assigning to each fermion line a new continuous fermion flow and applying appropriate Feynman rules for the chosen orientation of the fermion flow for vertices, propagators and external legs. Hence, for each fermion line in a diagram, there are two possibilities to derive the amplitude. For the quark-initiated channel, Eq. (4.24), this results in four different expressions for the amplitude of a single diagram. To clarify this point, in Fig. 4.6 the diagrams for the quark-initiated channel, Eq. (4.27), are displayed. These diagrams correspond to diagrams $\mathcal{M}_7$ and $\mathcal{M}_8$ of Fig. 4.5(b) and diagrams $\mathcal{M}_{10}$ - $\mathcal{M}_{14}$ of Fig. 4.5(c), and the diagrams only differing in the chirality of the internal squark have been gathered, such that the internal squark can be either left- or right-handed, denoted by $\tilde{q}_{jL/R}$. In order to distinguish between the initial and final quark of flavor j, the initial quark is called q_{j1} and the final one q_{j2}, respectively. According to the orientation of the fermion flow, the external particles are represented by

either u- or v-spinors. From the formulae below the diagrams, for each diagram the four different representations can be read off: the upper and lower term on the left-hand side of the curly brackets correspond to the resulting expressions for the one fermion chain for both orientations of the fermion flow, the upper and lower term on the right-hand side correspond to the two orientations of the fermion flow for the second fermion chain. While the spinors for the particle a with momentum p_a and helicity λ_a are denoted explicitly by $u_a := u(p_a, \lambda_a)$ and $v_a := v(p_a, \lambda_a)$, all remainders of the amplitude are collected in the generic variable Γ [12]. For each diagram any concatenation of a term on the left-hand side of the curly brackets with one term on the right-hand side of the brackets leads to a valid expression for the amplitude. For the analytic calculation of the interference terms, one has to make sure that from the four possible expressions for each of the single amplitudes, the ones are picked which lead to a common spinor representation of each particle. For example for the interference term between the upper left and middle diagram in Fig. 4.6 for both diagrams one can choose the upper term on both sides of the curly brackets, since then all particles are described by u-spinors in both amplitudes. Similarly one could also choose the lower terms on both sides of the brackets for both diagrams. However, any other combination is not possible for the analytic calculation since then a single particle is represented by a v-spinor in the one amplitude, but by a u-spinor in the other amplitude. For the interference term between the upper left and the upper right diagram of Fig. 4.6, one could choose either the upper left and lower right term, or the lower left and upper right term in both amplitudes for a valid description. Other combinations mix u- and v-spinors. The reason for the different combinations to be compatible or not lies in the distinct connections of external fermions by the fermion chains. In the upper left diagram q_i is connected to q_{j2}, in the middle it is connected to the gluino and on the right to the other quark q_{j1}. To summarize, for each interference term being calculated suitable individual choices for the orientations of the fermion flows have to be made for the two amplitudes involved.
It turns out, that two different combinations of fermion flows are sufficient for each diagram to cover all interference terms. In the gluon-initiated channel and the leading order diagrams there is only a single fermion line involved such that the fermion flow can be fixed once and for all.

In total, a calculation of the quark-initiated real corrections, Eq. (4.24), has been performed for a left-handed squark and a right-handed squark and for two different orientations of the fermion flows, the gluon-initiated channel, Eq. (4.23), and the leading order amplitudes were calculated only for a left-handed squark for one orientation of the fermion flow. All remaining chiralities and the amplitudes for antisquarks have been obtained by appropriate changes of the sign of the the spin dependent parts.

4.3.3. Gauge Invariance for Amplitudes with Two External Gluons

Slavnov-Taylor identities offer a test of gauge invariance and unitarity of the S matrix (see for example [157]). Thereby they also help to ensure that only the physical states of quantum fields contribute to the scattering amplitude. In the channels Eq. (4.22) and Eq. (4.23) this is of particular interest as the non-abelian nature of QCD encoded in the $SU(3)$ symmetry can lead to unphysical longitudinal polarization states of the gluons. To subtract these unphysical states one can either calculate and subtract the corresponding ghost contribution or choose the polarization sums for the external gluons such that only the physical modes remain. Here,

[12] Note, that these remainders are not identical for the different diagrams and fermion flows, but still we denote them collectively by Γ for better readability and since the exact expressions do not matter for the current explanation.

we focus on the gluon gluon channel Eq. (4.23) which was calculated explicitly.
Let the momentum and color of the first gluon be k_1 and a, respectively, and the ones for the second gluon k_2 and b. Stripping off the polarization vectors for the gluons, the amplitude for this process can be denoted by $\mathcal{M}^{ab}_{\mu\nu}$ and the corresponding ghost contribution by $\mathcal{G}^{ab}$. From the unitarity of the S-matrix one can derive the condition that [157]

$$\mathcal{M}^{ab}_{\mu\nu}\mathcal{M}^{ab*}_{\mu'\nu'}g^{\mu\mu'}g^{\nu\nu'} - 2\mathcal{G}^{ab}\mathcal{G}^{ab*} = \mathcal{M}^{ab}_{\mu\nu}\mathcal{M}^{ab*}_{\mu'\nu'}P^{\mu\mu'}(k_1)P^{\nu\nu'}(k_2) \ , \tag{4.33}$$

where $g^{\mu\mu'}$ is the Minkowski metric and $P^{\mu\mu'}(k_1)$ and $P^{\nu\nu'}(k_2)$ are the polarization sums for the external gluons only accounting for the physical modes. The left-hand side of Eq. (4.33) corresponds to using the simple polarization sum over physical polarizations λ_{phys}

$$\sum_{\lambda_{\text{phys}}} \epsilon^{\mu*}(k_i)\epsilon^{\nu}(k_i) = -g^{\mu\nu} \ , \tag{4.34}$$

with the polarization vectors $\epsilon^{\mu}(k_i)$ for $i = 1, 2$, known from QED. Thereby in a first step the unphysical polarization states are not treated properly. They are then canceled explicitly by subtracting the ghost amplitude squared incoherently. On the right-hand side, unphysical polarizations of the external gluons are directly avoided by summing over physical states only by the correct polarization sums $P^{\mu\mu'}(k_1)$ and $P^{\nu\nu'}(k_2)$. Following [157], in this section we will show the equality of both approaches by Slavnov-Taylor identities and discuss possible advantages and disadvantages of the methods.

The polarization sums of axial type on the right-hand side of Eq. (4.33) are given by

$$\begin{aligned} P^{\mu\mu'}(k_1) &= -g^{\mu\mu'} + \frac{k_1^{\mu}n_1^{\mu'} + k_1^{\mu'}n_1^{\mu}}{(k_1n_1)} - \frac{n_1^2k_1^{\mu}k_1^{\mu'}}{(k_1n_1)^2} \ , \\ P^{\nu\nu'}(k_2) &= -g^{\nu\nu'} + \frac{k_2^{\nu}n_2^{\nu'} + k_2^{\nu'}n_2^{\nu}}{(k_2n_2)} - \frac{n_2^2k_2^{\nu}k_2^{\nu'}}{(k_2n_2)^2} \ , \end{aligned} \tag{4.35}$$

where n_1 and n_2 are arbitrary four-vectors fulfilling

$$n_i \cdot \epsilon_i(k_i) = 0 \qquad \text{and} \qquad n_i \cdot k_i \neq 0 \ . \tag{4.36}$$

It directly follows that n_i must not be proportional to k_i. For the polarization vectors ϵ_i we have

$$k_i \cdot \epsilon_i(k_i) = 0 \ . \tag{4.37}$$

Transversality of the polarization sums Eq. (4.35) can be shown by contraction with the corresponding momenta. Comparing the left- and right-hand side of Eq. (4.33) apparently the terms involving the vectors n_i in the polarization sums Eq. (4.35) must account for the ghost part on the left-hand side of Eq. (4.33). To verify this explicitly, contractions of the amplitudes $\mathcal{M}^{ab}_{\mu\nu}$ and $\mathcal{M}^{ab*}_{\mu'\nu'}$ with these terms have to be calculated. In that context, the two contractions $k_1^{\mu}\mathcal{M}^{ab}_{\mu\nu}$ and $\mathcal{M}^{ab}_{\mu\nu}k_2^{\nu}$ are of particular interest and are given by Slavnov-Taylor identities [157]

$$k_1^{\mu}\mathcal{M}^{ab}_{\mu\nu} = -\mathrm{i}\mathcal{G}^{ab}k_{2\nu} \ , \tag{4.38}$$

$$\mathcal{M}^{ab}_{\mu\nu}k_2^{\nu} = -\mathrm{i}\mathcal{G}^{ab}k_{1\mu} \ . \tag{4.39}$$

Moreover, choosing light-like vectors n_i such that $n_i^2 = 0, \ i = 1, 2$, removes the last term in the sums Eq. (4.35) and simplifies the calculation. With this simplification the right-hand

side of Eq. (4.33) is given by

$$\mathcal{M}_{\mu\nu}\mathcal{M}^*_{\mu'\nu'}P^{\mu\mu'}(k_1)P^{\nu\nu'}(k_2) \tag{4.40a}$$

$$= \mathcal{M}_{\mu\nu}\mathcal{M}^*_{\mu'\nu'}\left(-g^{\mu\mu'}+\frac{k_1^\mu n_1^{\mu'}+k_1^{\mu'}n_1^\mu}{(k_1n_1)}\right)\left(-g^{\nu\nu'}+\frac{k_2^\nu n_2^{\nu'}+k_2^{\nu'}n_2^\nu}{(k_2n_2)}\right) \tag{4.40b}$$

$$= \mathcal{M}_{\mu\nu}\mathcal{M}^*_{\mu'\nu'}\Bigg(g^{\mu\mu'}g^{\nu\nu'} - \underbrace{g^{\mu\mu'}\frac{k_2^\nu n_2^{\nu'}+k_2^{\nu'}n_2^\nu}{(k_2n_2)}}_{\mathcal{I}_1{}^{\mu\mu'\nu\nu'}} - \underbrace{g^{\nu\nu'}\frac{k_1^\mu n_1^{\mu'}+k_1^{\mu'}n_1^\mu}{(k_1n_1)}}_{\mathcal{I}_2{}^{\mu\mu'\nu\nu'}} + \underbrace{\frac{k_1^\mu n_1^{\mu'}+k_1^{\mu'}n_1^\mu}{(k_1n_1)}\frac{k_2^\nu n_2^{\nu'}+k_2^{\nu'}n_2^\nu}{(k_2n_2)}}_{\mathcal{I}_3{}^{\mu\mu'\nu\nu'}}\Bigg)\,, \tag{4.40c}$$

where the color indices a and b have been omitted for simplicity. The first term in the bracket of Eq. (4.40c) can be identified with the first term on the left-hand side of Eq. (4.33). With the help of Eqs. (4.38) and (4.39) the contraction of the matrix elements with $\mathcal{I}_1$ is computed as

$$\mathcal{M}_{\mu\nu}\mathcal{M}^*_{\mu'\nu'}\mathcal{I}_1{}^{\mu\mu'\nu\nu'} = \mathcal{M}_{\mu\nu}\mathcal{M}^*_{\mu'\nu'}g^{\mu\mu'}\frac{k_2^\nu n_2^{\nu'}+k_2^{\nu'}n_2^\nu}{(k_2n_2)} \tag{4.41a}$$

$$= \frac{(-\mathrm{i}\mathcal{G}k_{1\mu})\mathcal{M}^{*\mu}{}_{\nu'}n_2^{\nu'}}{(k_2n_2)} + \frac{\mathcal{M}_{\mu\nu}(+\mathrm{i}\mathcal{G}^*k_1^\mu)n_2^\nu}{(k_2n_2)} \tag{4.41b}$$

$$= \frac{-\mathrm{i}\mathcal{G}(+\mathrm{i}\mathcal{G}^*k_{2\nu'})n_2^{\nu'}}{(k_2n_2)} + \frac{\mathrm{i}\mathcal{G}^*(-\mathrm{i}\mathcal{G}k_{2\nu})n_2^\nu}{(k_2n_2)} \tag{4.41c}$$

$$= (\mathcal{G}\mathcal{G}^*+\mathcal{G}^*\mathcal{G})\frac{(k_2n_2)}{(k_2n_2)} \tag{4.41d}$$

$$= 2\mathcal{G}\mathcal{G}^*\,. \tag{4.41e}$$

Likewise also the contraction of the matrix elements with $\mathcal{I}_2$ of Eq. (4.40c) can be evaluated and results in

$$\mathcal{M}_{\mu\nu}\mathcal{M}^*_{\mu'\nu'}\mathcal{I}_2{}^{\mu\mu'\nu\nu'} = 2\mathcal{G}\mathcal{G}^*\,. \tag{4.42}$$

Focusing only on the numerators first, the computation of the four terms resulting from the last term in the bracket of Eq. (4.40c) yields

$$\begin{aligned}\mathcal{M}_{\mu\nu}\mathcal{M}^*_{\mu'\nu'}k_1^\mu n_1^{\mu'}k_2^\nu n_2^{\nu'} &= -\mathrm{i}\mathcal{G}k_{2\nu}k_2^\nu\mathcal{M}^*_{\mu'\nu'}n_1^{\mu'}n_2^{\nu'}\\ &= 0\,,\end{aligned} \tag{4.43}$$

$$\begin{aligned}\mathcal{M}_{\mu\nu}\mathcal{M}^*_{\mu'\nu'}k_1^\mu n_1^{\mu'}k_2^{\nu'}n_2^\nu &= -\mathrm{i}\mathcal{G}k_{2\nu}n_1^{\mu'}(+\mathrm{i}\mathcal{G}^*k_{1\mu'})n_2^\nu\\ &= \mathcal{G}\mathcal{G}^*(n_1k_1)(n_2k_2)\,,\end{aligned} \tag{4.44}$$

$$\begin{aligned}\mathcal{M}_{\mu\nu}\mathcal{M}^*_{\mu'\nu'}k_1^{\mu'}n_1^\mu k_2^\nu n_2^{\nu'} &= -\mathrm{i}\mathcal{G}k_{1\mu}(+\mathrm{i}\mathcal{G}^*k_{2\nu'})n_1^\mu n_2^{\nu'}\\ &= \mathcal{G}\mathcal{G}^*(k_1n_1)(k_2n_2)\,,\end{aligned} \tag{4.45}$$

$$\begin{aligned}\mathcal{M}_{\mu\nu}\mathcal{M}^*_{\mu'\nu'}k_1^{\mu'}n_1^\mu k_2^{\nu'}n_2^\nu &= \mathcal{M}_{\mu\nu}k_1^{\mu'}n_1^\mu(+\mathrm{i}\mathcal{G}^*k_{1\mu'})n_2^\nu\\ &= 0\,,\end{aligned} \tag{4.46}$$

where in Eqs. (4.43) and (4.46) it has been used that the external gluons are on-shell. Hence

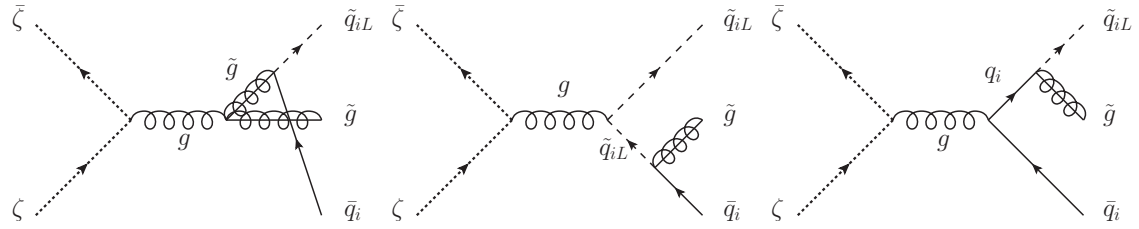

Figure 4.7: Diagrams for the unphysical process $\zeta + \bar{\zeta} \longrightarrow \tilde{q}_{iL} + \tilde{g} + \bar{q}_i$.

the contraction of the matrix elements with $\mathcal{I}_3$ results in

$$\mathcal{M}_{\mu\nu}\mathcal{M}^*_{\mu'\nu'}\mathcal{I}_3{}^{\mu\mu'\nu\nu'} = \frac{\mathcal{G}\mathcal{G}^*(n_1k_1)(n_2k_2) + \mathcal{G}\mathcal{G}^*(k_1n_1)(k_2n_2)}{(k_1n_1)(k_2n_2)} \tag{4.47}$$

$$= 2\mathcal{G}\mathcal{G}^* \ . \tag{4.48}$$

Altogether we find for Eq. (4.40)

$$\mathcal{M}_{\mu\nu}\mathcal{M}^*_{\mu'\nu'}P^{\mu\mu'}(k_1)P^{\nu\nu'}(k_2) = \mathcal{M}_{\mu\nu}\mathcal{M}^*_{\mu'\nu'}\left(g^{\mu\mu'}g^{\nu\nu'} - 2\mathcal{G}\mathcal{G}^* - 2\mathcal{G}\mathcal{G}^* + 2\mathcal{G}\mathcal{G}^*\right) \tag{4.49}$$

$$= \mathcal{M}_{\mu\nu}\mathcal{M}^*_{\mu'\nu'}\left(g^{\mu\mu'}g^{\nu\nu'} - 2\mathcal{G}\mathcal{G}^*\right) \ , \tag{4.50}$$

which proves that the polarization sums Eq. (4.35) with $n_1^2 = n_2^2 = 0$ satisfy Eq. (4.33). Since the contractions of the matrix elements with $\mathcal{I}_1$ and $\mathcal{I}_2$ lead to the same result, one of them is already sufficient to fulfill Eq. (4.33), meaning that in the polarization sums Eq. (4.35) the second term is required only for one of the polarization sums. If both are taken into account, the contribution of one of them is canceled by the contraction of the matrix elements with $\mathcal{I}_3$. Hence, the only choice to be made is to define either n_1 or n_2. The verification of Eq. (4.33) shown above only requires the second condition of Eq. (4.36) to hold. Accordingly, it is possible to set $n_1^\mu = k_2^\mu$ or $n_2^\mu = k_1^\mu$. This is advantageous as no new four-vector is introduced which would lead to new contractions with momenta in the matrix element squared. The polarization sums then read

$$\begin{aligned} P^{\mu\mu'}(k_1) &= -g^{\mu\mu'} + \frac{k_1^\mu k_2^{\mu'} + k_1^{\mu'} k_2^\mu}{(k_1k_2)} \ , \\ P^{\nu\nu'}(k_2) &= -g^{\nu\nu'} \ . \end{aligned} \tag{4.51}$$

As explained above alternatively the unphysical degrees of freedom can be canceled explicitly by subtracting the ghost contribution. In the case of the gluon gluon channel the latter is given by the unphysical process of two ghosts ζ producing the squark, the antiquark and the gluino. Working in Feynman gauge for the internal gluon, the only interaction of physical particles with ghosts is given by the ghost ghost gluon vertex and only the diagrams with a triple gluon vertex can be converted into diagrams contributing to the ghost amplitude. These are the diagrams $\mathcal{M}_1$, $\mathcal{M}_5$ and $\mathcal{M}_8$ of Fig. 4.4 and the resulting ghost diagrams are presented in Fig. 4.7. Also the calculation of the matrix element $\mathcal{M}^{ab}_{\mu\nu}$ can be performed in Feynman gauge, where the numerator of the gluon propagator takes a simple form. The amplitude squared for the process Eq. (4.23) is then given by the left-hand side of Eq. (4.33).

Both approaches have been implemented and have been used as cross-check. Note, that if a regulator width Γ_{reg} is introduced at the amplitude level for regularizing an OSS, the

two methods do not give identical results any more. Only in the limit $\Gamma_{\text{reg}} \longrightarrow 0$ they are equivalent. Although the polarization sums Eq. (4.51) are much simpler than the general ones Eq. (4.35), still the resulting amplitudes squared for the calculation with physical polarization sums are much longer than the amplitudes squared obtained with the calculation with ghosts. However, since for the OS subtraction explained above the amplitudes are split in resonant and non-resonant parts and depending on the subtraction method several parts of the amplitude squared are dropped, one has to make sure that the cancelation of the unphysical polarizations is still intact as there are OS resonances also in the ghost process. Therefore in order to be on the safe side the matrix element squared computed according to the right-hand side of Eq. (4.33) with the polarization sums Eq. (4.51) has been used for the implementation and the results. For internal gluons the Feynman gauge has been used[13].
The entire calculation of the amplitude squared for the real corrections to squark gluino production has been checked against an independent calculation of a team member. Moreover, numerical checks against results obtained by `FeynArts` and `FormCalc` have been performed for the spin independent part. Due to their length, we do not show explicit formulae for the amplitudes squared for the real corrections with spin dependence here.

4.4. Implementation in the POWHEG-BOX

The process has been implemented in the `POWHEG − BOX` [38], which has been introduced in Sec. 2.2.2. The implementation of the production process with the gluino decay at LO has been performed according to the procedure explained in Sec. 4.1.1 and Sec. 4.1.2. Additionally, the amplitude for the squark decay presented in Sec. 4.1.3 has been implemented in order to complete the decay chain. The total decay widths of squarks and gluinos at LO which are required for the correct application of the NWA explained in Sec. 2.2.1 are computed with routines from `SDECAY` [158]. These routines can also be used to calculate the decay widths at NLO as required for the NLO computation. After implementing all amplitudes for the LO process as explained above, as well as the virtual and real corrections for the production process, spin and color correlated matrix elements which occur in the soft and collinear limits of the real amplitudes squared have been derived and implemented. The color correlated Born amplitudes are given by [38]

$$\mathcal{B}_{ij} = -N \sum_{s,c} \mathcal{M}_{\{c_k\}} \left(\mathcal{M}^{\dagger}_{\{c_k\}}\right)_{\substack{c_i \to c_{i'} \\ c_j \to c_{j'}}} T^a_{c_i c_{i'}} T^a_{c_j c_{j'}} \ , \tag{4.52}$$

where N is a factor collecting all contributions from spin and color averaging, the sum runs over all spins s and colors c and $\{c_k\}$ denotes all color indices in the Born matrix elements $\mathcal{M}$. The minus sign is a convention of the `POWHEG − BOX`. The generators $T^a_{c_i c_{i'}}$ depend on the $SU(3)$ representation of the i^{th} particle, namely $T^a_{cb} = \mathrm{i} f_{cab}$ for particles in the adjoint representation, like gluons or gluinos, where f_{abc} are the structure constants of $SU(3)$. For incoming particles and outgoing antiparticles in the fundamental representation (quarks, squarks) we have $T^a_{\alpha\beta} = t^a_{\alpha\beta}$ and for incoming antiparticles and outgoing particles $T^a_{\alpha\beta} = -t^a_{\beta\alpha}$ where $t^a_{\alpha\beta}$ are the color matrices in the fundamental representation of $SU(3)$. This means that the color correlated matrix elements are given by the usual Born matrix elements squared with a color factor modified according to Eq. (4.52). They have been derived both for the production process and the decays. The spin correlated matrix elements must not be confused with the spin correlations between production and decay of the gluino which we investigate here. The

[13] The tensor $\mathcal{M}_{\mu\nu}$ is a gauge-invariant quantity, so the gauge for the internal gluons can be chosen independently of the polarization sums.

spin correlated Born amplitudes are defined by [38]

$$\mathcal{B}_j^{\mu\nu} = N \sum_{\substack{\{s\},s_j,s_{j'} \\ \text{color}}} \mathcal{M}(\{s\},s_j)\mathcal{M}^\dagger(\{s\},s_{j'})\epsilon^{\mu*}(s_j)\epsilon^\nu(s_{j'}) \ , \tag{4.53}$$

with s_j denoting the spin of the j^{th} gluon and $\{s\}$ all other spins, respectively, and N is the normalization factor covering spin and color averages. The polarization vectors $\epsilon^\mu(s_j)$ are normalized by

$$g_{\mu\nu}\epsilon^{\mu*}(s_j)\epsilon^\nu(s_{j'}) = -\delta_{s_j s_{j'}} \ , \tag{4.54}$$

such that

$$g_{\mu\nu}\mathcal{B}_j^{\mu\nu} = -\mathcal{B} \ , \tag{4.55}$$

where $\mathcal{B}$ denotes the Born matrix element squared. A check for the correctness of the spin- and color correlated matrix elements is provided by verifying the cancelation of all soft and collinear divergences resulting from the real corrections. This is done automatically by the POWHEG − BOX.
Furthermore, a parametrization of the phase space for the leading order process has been implemented, which takes random numbers as inputs and defines all kinematics of the process accordingly. Starting from this Born phase space, the phase space for the real emission is constructed automatically by the POWHEG − BOX. As explained in [34, 149] this leads to two problems for the OS subtraction using the DS method. First, in this way the resonances in the real emission amplitudes are not sampled efficiently and second, the phase space which is remapped to the OS kinematics in the OS subtraction counterterm requires a modified Jacobian factor, which cannot be accomplished easily in the construction of the phase space by the POWHEG − BOX. A solution to these problems was invented in [34, 149] and taken up in [152]. There, the amplitudes squared of the real corrections are split into parts containing OS resonances and parts without resonances. The parts with resonances are integrated separately, while the non-resonant parts are integrated by the usual POWHEG − BOX routines. The separate integration is tailored to the resonance structure and allows for the modified Jacobian of the phase space. This splitting is possible as the resonant parts do not contain infrared singularities which have to be treated by the FKS subtraction scheme implemented in the POWHEG − BOX. However, this solution requires major modifications of the source code of the POWHEG − BOX because a new part of the cross section has to be defined, where the resonant parts are integrated separately, and which is added to the result in the end. While the virtual and real corrections described above have already been implemented the necessary modifications and implementations for the OS subtraction have not been adapted to squark gluino production yet.

The implementation has been accompanied by a documentation using Doxygen [159], which can provide assistance for future developments. A description of this together with basic information on input variables for the POWHEG − BOX is provided in App. A. The implementation of the LO process has been checked by independent calculations and implementations. Also the implementation of the real corrections in the POWHEG − BOX has been cross-checked by another team member and by results from FeynArts and FormCalc for the spin independent part.

4.5. Results

Since the full implementation of squark gluino production including the OS subtraction and the decays is not yet complete, we provide results at parton level for the calculation at

Scenario	m_0 [GeV]	$m_{1/2}$ [GeV]	A_0 [GeV]	$\tan\beta$
A	1000	1200	-2000	30
B	1600	1400	-3200	30

Table 4.4: Input parameters for the two test scenarios A and B. In both scenarios we set $\mu > 0$.

Particle mass	Scenario A	Scenario B
$m_{\tilde{u}_L} \approx m_{\tilde{c}_L}$ [GeV]	2466	3043
$m_{\tilde{d}_L} \approx m_{\tilde{s}_L}$ [GeV]	2467	3044
$m_{\tilde{u}_R} \approx m_{\tilde{c}_R}$ [GeV]	2379	2949
$m_{\tilde{d}_R} \approx m_{\tilde{s}_R}$ [GeV]	2369	2938
$m_{\tilde{g}}$ [GeV]	2544	2968

Table 4.5: Masses oft left- and right-handed squarks of the first two generations and the gluino for the test scenarios A and B.

LO which serve as a proof of principles for the spin correlations captured by the procedure explained in Sec. 4.1.1.
For these demonstration purposes we choose two different scenarios A and B in the MSSM using the mSUGRA mechanism (*cf.* Sec. 2.1). The input parameters of the scenarios are presented in Tab. 4.4. These parameters are read in by the spectrum generator `SPheno` to generate the complete particle spectrum. The electroweak fine-structure constant $\alpha^{\overline{\text{MS}}}(M_Z)$ and the strong coupling constant $\alpha_s^{\overline{\text{MS}}}(M_Z)$ in the $\overline{\text{MS}}$-scheme at the scale M_Z and the Fermi constant G_F have been set according to [80]

$$\left(\alpha^{\overline{\text{MS}}}(M_Z)\right)^{-1} = 127.95 \,, \qquad \alpha_s^{\overline{\text{MS}}}(M_Z) = 0.1182 \,, \qquad G_F = 1.1663787 \cdot 10^{-5} \,, \tag{4.56}$$

and the masses have been set to

$$m_Z = 91.1876 \text{ GeV} \,, \qquad m_t = 174.2 \text{ GeV} \,, \qquad m_b^{\overline{\text{MS}}}(m_b) = 4.18 \text{ GeV} \,, \tag{4.57}$$

$$m_\tau = 1.77686 \text{ GeV} \,, \qquad m_\mu = 105.6584 \text{ MeV} \,, \qquad m_e = 510.9989 \text{ keV} \,, \tag{4.58}$$

$$m_d = 4.7 \text{ MeV} \,, \qquad m_u = 2.2 \text{ MeV} \,, \qquad m_s = 96 \text{ MeV} \,, \tag{4.59}$$

$$m_c^{\overline{\text{MS}}}(m_c) = 1.27 \text{ GeV} \,, \tag{4.60}$$

where M_Z, m_t, m_τ, m_μ and m_e are the pole masses of the Z-boson, the top-quark, and the charged leptons, $m_b^{\overline{\text{MS}}}(m_b)$ and $m_c^{\overline{\text{MS}}}(m_c)$ are the running masses of the bottom- and the charm-quark in the $\overline{\text{MS}}$-scheme evaluated at the bottom- and charm-quark mass, respectively, and m_d, m_u, m_s are 'current quark masses' for the down-, the up- and the strange-quark as given in [80]. The masses of the squarks of the first two generations and the gluino in the scenarios A and B are given in Tab. 4.5. The scenarios are chosen such that they evade the exclusion limits on the parameters m_0 and $m_{1/2}$ shown in the introduction in Fig. 2.2. Moreover, with the masses given in Tab. 4.5 they are not excluded by current searches for

the four light-flavored squarks, stops and the gluino [160–168]. Additionally both scenarios feature a CP-even Higgs boson with a mass of

$$m_h^{\mathrm{A}} = 123.0 \text{ GeV} \qquad \text{and} \qquad m_h^{\mathrm{B}} = 124.7 \text{ GeV} \tag{4.61}$$

for scenario A and B, respectively, such that it is compatible with the measured value of (125.09 ± 0.32) GeV [47] regarding the theoretical uncertainty of the spectrum generator [169]. Since these scenarios serve for demonstration purposes only, a more detailed analysis of all relevant experimental exclusion bounds is not performed here.
In the first scenario A all squarks are lighter than the gluino, so all decay channels of the gluino are kinematically open. Scenario B is an intermediate case, where the left-handed squarks are heavier, but the right-handed squarks are lighter than the gluino. Accordingly the gluino can only decay into a right-handed squark. The phase space available in the gluino decay in scenario B is much smaller than in scenario A, which will influence the impact of spin correlations on kinematic distributions. With respect to the OS subtraction, these two scenarios will be interesting to study, as they lead to distinct patterns of OSS as shown in Tab. 4.1.

The parton distribution functions used for this analysis at LO are the CTEQ6LO functions [170] provided by the LHAPDF interface [171] and the factorization scale as well as the renormalization scale have been set to

$$\mu_F = \mu_R = \frac{m_{\tilde{q}} + m_{\tilde{g}}}{2} \ , \tag{4.62}$$

where $\tilde{q}$ denotes the specific squark considered in the analyses below. The total cross sections of the squark gluino production for all types of squarks calculated with the implementation in the `POWHEG − BOX` at a center-of-mass energy of 14 TeV are given in Tab. 4.6. In the bottom line the sum of all sub-channels is computed, which is the total cross section of squark gluino production to any squark and a gluino in the scenarios A and B. In order to investigate the spin correlations at the parton level, we pick one sub-channel and specify the complete decay chain for each scenario. In scenario A, a left-handed up-squark is produced directly and the gluino is chosen to decay into a right-handed down-squark and a down-antiquark. Completing the decay chain, the corresponding squark decays are attached for both squarks. For scenario B, we choose a right-handed down-squark to be produced directly and let the gluino decay into a right-handed charm-squark and a charm-antiquark. Again, the corresponding squark decays are attached. These choices for both scenarios are depicted in Figs. 4.8(a) and 4.8(b), respectively.
The total decay widths and the branching ratios of the squark and gluino decays which are relevant for the processes defined in Fig. 4.8 are obtained from the `SDECAY` routines and are given in Tab. 4.7. Hence for the process considered in scenario A a cross section of about $2.39 \cdot 10^{-5}$ fb and for the process in scenario B a cross section of about $4.45 \cdot 10^{-7}$ fb are expected according to the NWA. The total cross sections for these processes calculated from the `POWHEG − BOX` are listed in Tab. 4.8. The agreement of these numbers among each other and with the expected cross sections on the one hand shows that the implementation of the decays in the `POWHEG − BOX` is correct and on the other hand proves that the spin correlations do not change the total cross section, as already stated in Sec. 4.1.2.
In order to investigate the effect of the spin correlations we now turn to kinematic distributions. For differential cross sections with respect to an observable X shown in the upper panels of the following plots, the ratio plotted in the lower panels is always defined by

$$\text{Ratio} = \frac{\mathrm{d}\sigma/\mathrm{d}X|_{\text{with spin correlations}}}{\mathrm{d}\sigma/\mathrm{d}X|_{\text{without spin correlations}}} \ . \tag{4.63}$$

Squark produced	$\sigma^{\mathrm{A}}_{\mathrm{LO}}$ [fb]	$\sigma^{\mathrm{B}}_{\mathrm{LO}}$ [fb]
$\tilde{u}_L$	$1.24 \cdot 10^{-1}$	$1.24 \cdot 10^{-2}$
$\tilde{d}_L$	$2.93 \cdot 10^{-2}$	$2.46 \cdot 10^{-3}$
$\tilde{c}_L$	$2.28 \cdot 10^{-4}$	$1.48 \cdot 10^{-5}$
$\tilde{s}_L$	$5.64 \cdot 10^{-4}$	$3.45 \cdot 10^{-5}$
$\tilde{u}_R$	$1.49 \cdot 10^{-1}$	$1.52 \cdot 10^{-2}$
$\tilde{d}_R$	$3.67 \cdot 10^{-2}$	$3.16 \cdot 10^{-3}$
$\tilde{c}_R$	$2.85 \cdot 10^{-4}$	$1.88 \cdot 10^{-5}$
$\tilde{s}_R$	$7.31 \cdot 10^{-4}$	$4.56 \cdot 10^{-5}$
$\tilde{u}^*_L$	$1.19 \cdot 10^{-3}$	$7.85 \cdot 10^{-5}$
$\tilde{d}^*_L$	$9.61 \cdot 10^{-4}$	$4.98 \cdot 10^{-5}$
$\tilde{c}^*_L$	$2.28 \cdot 10^{-4}$	$1.48 \cdot 10^{-5}$
$\tilde{s}^*_L$	$5.64 \cdot 10^{-4}$	$3.45 \cdot 10^{-5}$
$\tilde{u}^*_R$	$1.48 \cdot 10^{-3}$	$1.00 \cdot 10^{-4}$
$\tilde{d}^*_R$	$1.26 \cdot 10^{-3}$	$6.73 \cdot 10^{-5}$
$\tilde{c}^*_R$	$2.85 \cdot 10^{-4}$	$1.88 \cdot 10^{-5}$
$\tilde{s}^*_R$	$7.31 \cdot 10^{-4}$	$4.56 \cdot 10^{-5}$
Total	$3.48 \cdot 10^{-1}$	$3.37 \cdot 10^{-2}$

Table 4.6: Cross sections for squark gluino production at leading order $\sigma^{\mathrm{A}}_{\mathrm{LO}}$ and $\sigma^{\mathrm{B}}_{\mathrm{LO}}$ for different squarks and antisquarks for scenarios A and B.

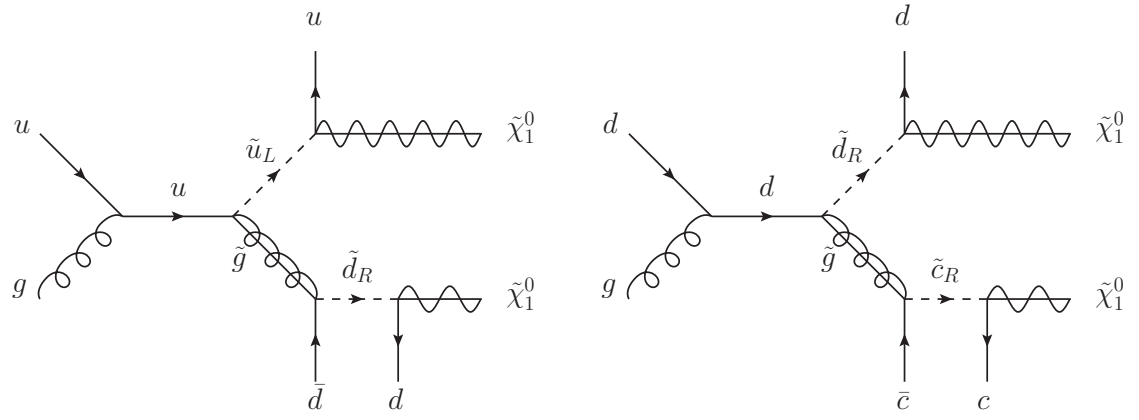

(a) Specific process considered for scenario A.

(b) Specific process considered for scenario B.

Figure 4.8: Processes considered for the analysis of spin correlations.

	Scenario A	Scenario B
$\Gamma_{\tilde{u}_L}$	21.8 GeV	28.2 GeV
$\Gamma_{\tilde{d}_R}$	1.20 GeV	1.50 GeV
$\Gamma_{\tilde{c}_R}$	4.82 GeV	6.04 GeV
$\Gamma_{\tilde{g}}$	35.0 GeV	33.3 GeV
$\mathrm{BR}(\tilde{u}_L \longrightarrow u\tilde{\chi}_1^0)$	$1.41 \cdot 10^{-2}$	$1.36 \cdot 10^{-2}$
$\mathrm{BR}(\tilde{d}_R \longrightarrow d\tilde{\chi}_1^0)$	$9.99 \cdot 10^{-1}$	$9.99 \cdot 10^{-1}$
$\mathrm{BR}(\tilde{c}_R \longrightarrow c\tilde{\chi}_1^0)$	$9.99 \cdot 10^{-1}$	$9.99 \cdot 10^{-1}$
$\mathrm{BR}(\tilde{g} \longrightarrow \tilde{d}_R\bar{d})$	$1.37 \cdot 10^{-2}$	$3.62 \cdot 10^{-4}$
$\mathrm{BR}(\tilde{g} \longrightarrow \tilde{c}_R\bar{c})$	$1.22 \cdot 10^{-2}$	$1.41 \cdot 10^{-4}$

Table 4.7: Total decay widths and branching ratios at leading order involved in the processes defined in Fig. 4.8.

	Scenario A	Scenario B
with spin correlations	$(2.396 \pm 0.003) \cdot 10^{-5}$ fb	$(4.468 \pm 0.005) \cdot 10^{-7}$ fb
without spin correlations	$(2.397 \pm 0.002) \cdot 10^{-5}$ fb	$(4.469 \pm 0.004) \cdot 10^{-7}$ fb

Table 4.8: Total cross sections for the processes defined in Fig. 4.8 for the two scenarios A and B calculated by the POWHEG − BOX with and without spin correlations. The error is the statistical error stated by the POWHEG − BOX.

Statistical errors provided by the POWHEG − BOX are indicated by the error bars on the ratio in the lower panel. For the distributions in the upper panels the errors are not shown for better readability.
The impact of the spin correlations on the angular distribution of the quarks can be investigated in Fig. 4.9, where differential distributions with respect to the pseudo-rapidities of the three quarks are shown. While for the up-quark and the down-quark stemming from the decays of the squarks in Figs. 4.9(a) and 4.9(c) the influence of the spin correlations is negligible, the central region for the down-antiquark from the gluino decay is slightly enhanced, as shown in Fig. 4.9(b). At the same time the tails for high absolute values of the pseudo-rapidity are suppressed such that the integral over the distribution is unchanged and leads to the total cross section given in Tab. 4.8.
A similar pattern can be observed in the distributions of the transverse momentum of the quarks shown in Fig. 4.10. The distributions for the two quarks from the squark decays in Figs. 4.10(a) and 4.10(c) are nearly unchanged, whereas the distribution for the down-antiquark from the gluino decay in Fig. 4.10(b) is shifted towards high $p_{T,\bar{d}}$. The strength of the enhancement can be up to about 20% for a transverse momentum of about 250 GeV. On the other hand, the suppression at low transverse momenta is about 10% for $p_{T,\bar{d}} < 150$ GeV. This is consistent with the observation for the pseudo-rapidities in Fig. 4.9, since a quark of a certain energy emitted in central direction has a higher transverse momentum than a

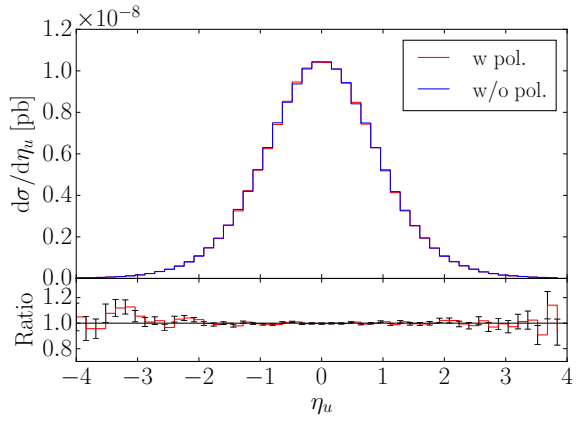

(a) Pseudo-rapidity of the up-quark.

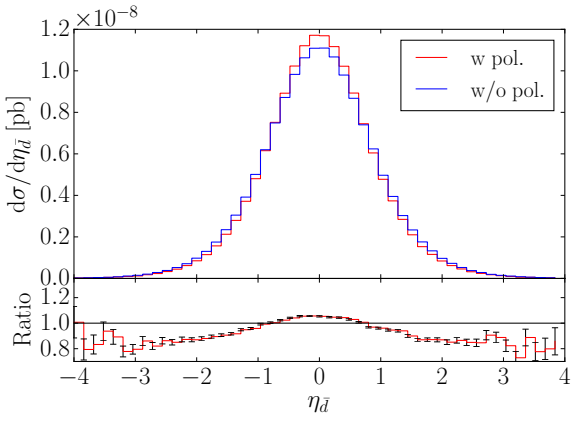

(b) Pseudo-rapidity of the down-antiquark.

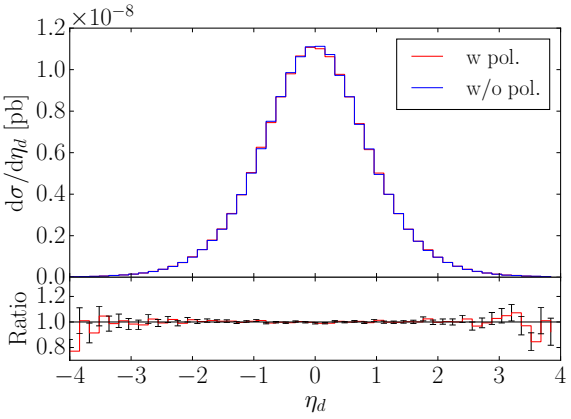

(c) Pseudo-rapidity of the down-quark.

Figure 4.9: Distributions of the pseudo-rapidities of the quarks for scenario A. The distributions in red correspond to the calculation with spin correlations for the gluino, the ones in blue are without spin correlations. The ratio in the lower panel is defined by Eq. (4.63). The error on the ratio results from the statistical errors provided by the POWHEG − BOX.

quark emitted at high absolute values of the pseudo-rapidity. The transverse momentum of the down-quark is dominated by the phase space available in the squark decay, such that the spin correlations do not have a visible impact on it. The distributions for the up-quark Figs. 4.9(a) and 4.10(a) are not expected to change due to spin correlations as the squark decay is isotropic.
Finally, the impact can also be measured in the distribution of the invariant mass of the up-quark and the down-antiquark $M_{u\bar{d}}$ displayed in Fig. 4.11. Also this distribution is shifted to higher values with enhancements up to about 20% for invariant masses of about 1300 GeV.

In the case of scenario B, we start investigating the transverse momenta of the quarks in Fig. 4.12. Similar to the case in scenario A in Fig. 4.10, the transverse momentum of the down-quark in Fig. 4.12(a) is not expected to change and the transverse momentum of the charm quark in Fig. 4.12(c) is dominated by the phase space available in the squark decay.

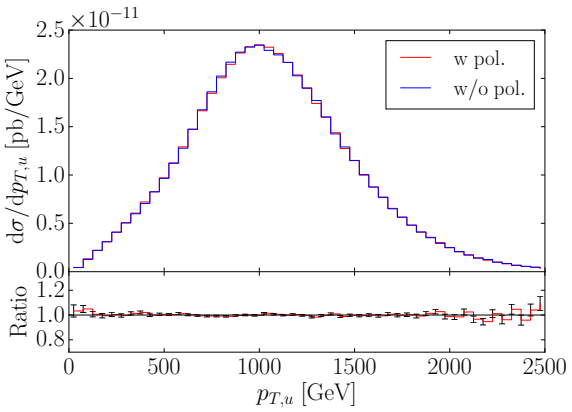

(a) Transverse momentum of the up-quark.

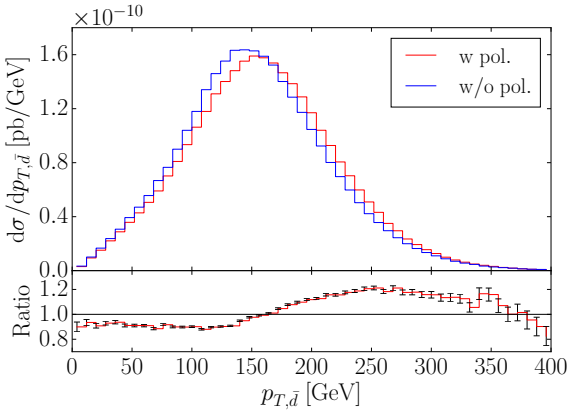

(b) Transverse momentum of the down-antiquark.

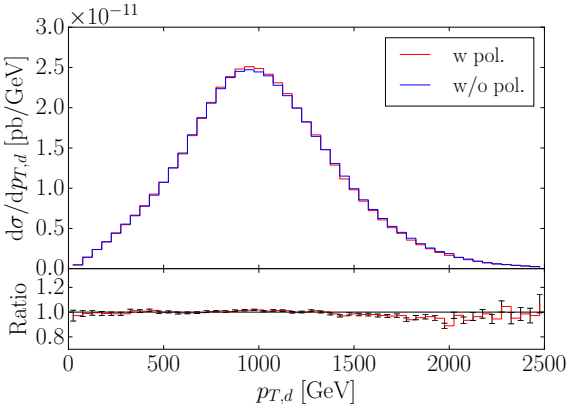

(c) Transverse momentum of the down-quark.

Figure 4.10: Transverse momentum distributions of the quarks for scenario A. The distributions with (without) spin correlations are shown in red (blue). The ratio in the lower panel is defined according to Eq. (4.63) with errors provided by the `POWHEG − BOX`.

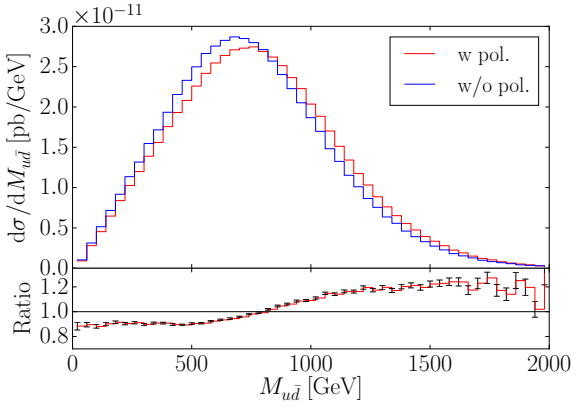

Figure 4.11: Invariant mass of the up-quark and the down-antiquark for scenario A. The result with spin correlations is plotted in red, the one without in blue, the ratio in the lower panel is defined by Eq. (4.63) with errors derived by the `POWHEG − BOX`.

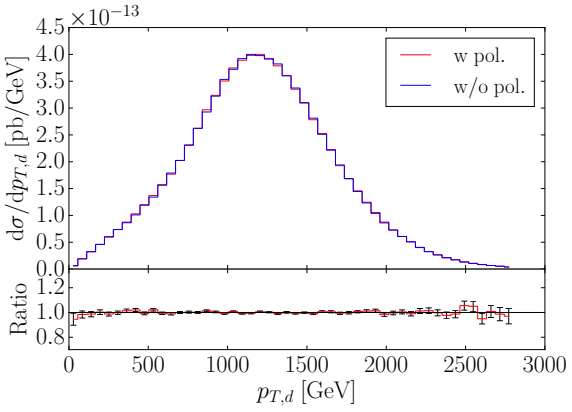

(a) Transverse momentum of the down-quark.

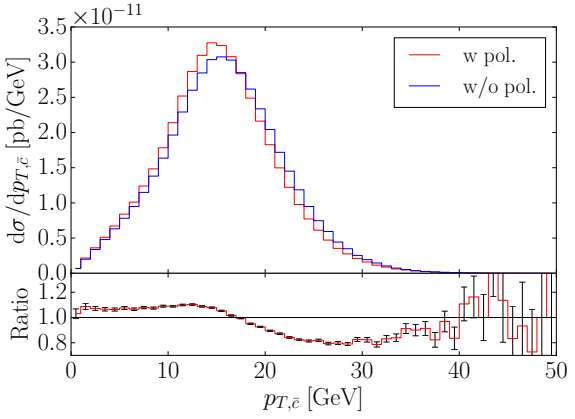

(b) Transverse momentum of the charm-antiquark.

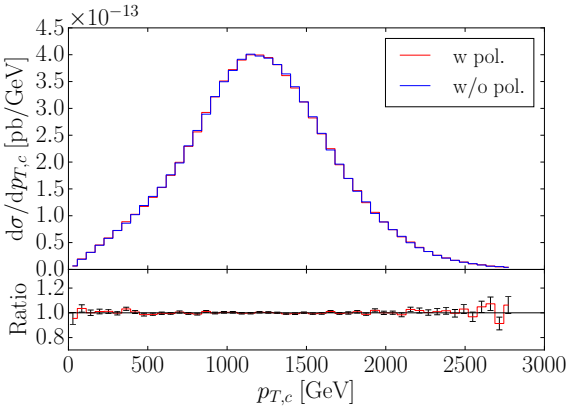

(c) Transverse momentum of the charm-quark.

Figure 4.12: Distributions of the transverse momenta of all three quarks for scenario B. In red the distributions with spin correlations, in blue the ones without. The ratio in the lower panel is given by Eq. (4.63) and the statistical error by the POWHEG − BOX.

The impact of the spin correlations is visible in the distribution of the transverse momentum of the charm-antiquark from the gluino decay in Fig. 4.12(b). This time, the spin correlations shift the distribution towards lower values. This results from the different chiralities of the squarks attached to the gluino line in Fig. 4.8(b) in comparison to Fig. 4.8(a). Instead of a left- and a right-handed squark, we now have two right-handed squarks, which cause the spin dependent part to have an opposite sign with respect to the process considered for scenario A (*cf.* Sec. 4.3.2). In contrast to the case for scenario A, the effect of the spin correlations cannot be observed in the distributions with respect to the pseudo-rapidities depicted in Fig. 4.13. While for the two quarks from the squark decays in Figs. 4.13(a) and 4.13(c) this is expected, it is not for the quark from the gluino decay in Fig. 4.13(b). The shift towards low values of the transverse momentum in Fig. 4.12(b) indicates an enhancement for large pseudo-rapidities. However, within the uncertainties indicated for the ratio in the lower panel of Fig. 4.13(b) this is not observed decisively. The reason for that is the very small difference

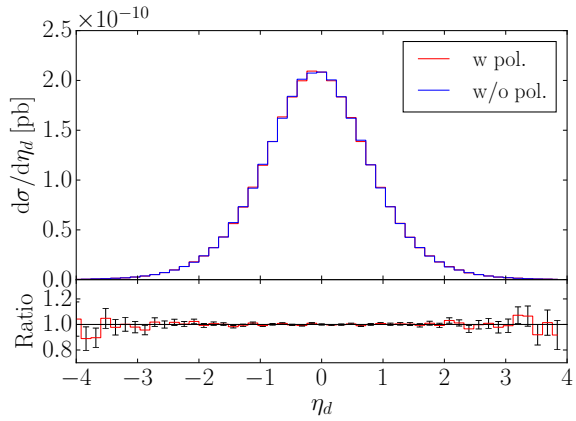

(a) Pseudo-rapidity of the down-quark.

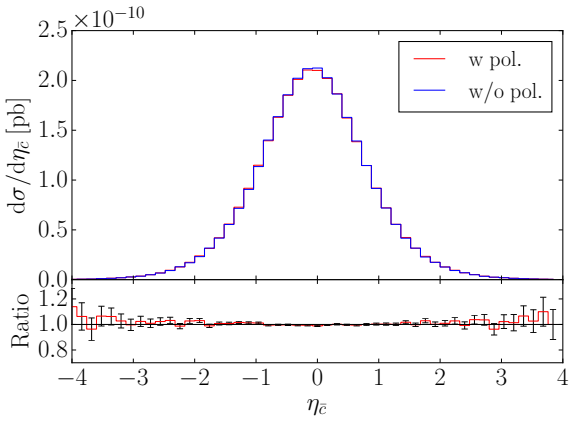

(b) Pseudo-rapidity of the charm-antiquark.

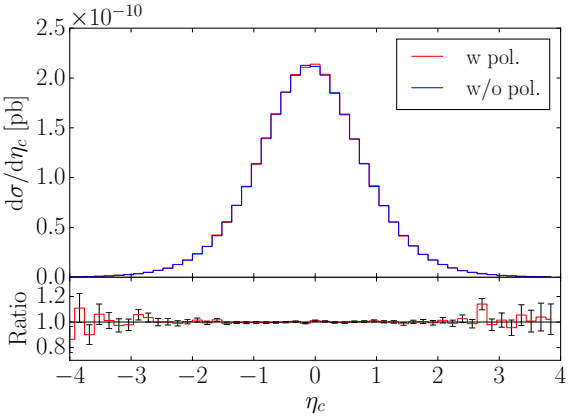

(c) Pseudo-rapidity of the charm-quark.

Figure 4.13: Distributions of the pseudo-rapidities of the quarks for scenario B. The distributions in red correspond to the calculation with spin correlations for the gluino, the ones in blue are obtained without spin correlations. The ratio in the lower panels is given by Eq. (4.63), the errors are derived by the POWHEG − BOX.

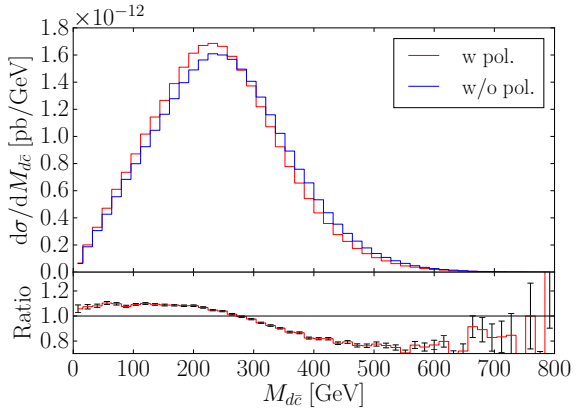

Figure 4.14: Invariant mass of the down-quark and the charm-antiquark of the process for scenario B. The red distribution results from the calculation with spin correlations, the blue curve is derived without them. The ratio in the lower panel is defined by Eq. (4.63) and the errors are provided by the POWHEG − BOX.

between the mass of the gluino and the mass of the right-handed charm squark of less than 20 GeV. Therefore the shift in the transverse momentum of the charm-antiquark caused by the spin correlations does not translate visibly into a to change of the angular distribution given by the pseudo-rapidity in Fig. 4.13(b) since its effect is completely overwhelmed by longitudinal boosts of the total event. These do not enter the distribution of the transverse momentum in Fig. 4.12(b). The invariant mass of the down-quark and the charm-antiquark shown in Fig. 4.14 on the other hand, is influenced by the spin correlations. Similarly to the case for the transverse momentum, the distribution is shifted towards low values of the invariant mass. The enhancement is about 10% for $M_{d\bar{c}} < 200$ GeV and the suppression for high values of the invariant mass reaches up to about 20% for $M_{d\bar{c}} \approx 500$ GeV.

4.6. Conclusion

In addition to NLO corrections, the spin correlations for the gluino are an important feature to investigate in the context of squark gluino production. In this work we have elaborated a framework to incorporate the spin correlations in a fully differential calculation of the production cross section for squark gluino production. The incorporation of the spin correlations also at NLO in a way where a gauge-invariant method to isolate and subtract OSS can be implemented required the analytic computation of the amplitudes squared for the real corrections to squark gluino production. This calculation has been accomplished here, the results have been implemented in the `POWHEG − BOX` and were checked against an independent calculation. The real corrections to the squark gluino production form a major ingredient for the full calculation at NLO. Since the final implementation of the OS subtraction together with the decays at NLO is not done yet, for demonstration purposes, results have been shown for the complete framework at LO. We found that the effect of spin correlations on distributions in the transverse momentum, pseudo-rapidities and invariant masses can be up to about 20%. These results only serve as a proof of principles. As we only investigated results at the parton level here, the observations can change when looking at physical events with a parton shower attached, which is left for future work.

5. Electroweak Phase Transition in the Two-Higgs-Doublet Model

This chapter is devoted to the investigation of the EWPT in the 2HDM. First, the effective potential of the 2HDM at finite temperature is explained in Sec. 5.1. Subsequently we will elucidate the renormalization procedure in Sec. 5.2 before finishing with the results and the conclusion in Secs. 5.3 and 5.4, respectively.

5.1. Effective Potential of the Two-Higgs-Doublet Model at Finite Temperature

Electroweak symmetry breaking takes place when the vacuum expectation value (VEV) of the Higgs field is no longer zero but attains a finite value. Hence, in order to find the critical temperature T_c where the EWPT occurs the Higgs potential has to be investigated as the VEV is determined by the field configuration in the global minimum of the potential. Obviously a calculation at vanishing temperature cannot cover the dynamics of the symmetry breaking which is why the potential has to be computed at finite temperature T. The temperature dependence first appears at the one-loop level and hence the effective potential V_{eff}, consisting of the tree-level potential V_0 and one-loop radiative corrections V_1

$$V_{eff} = V_0 + V_1 \tag{5.1}$$

has to be considered. Calculating the one-loop effective potential at finite temperature, as done for instance in [93], shows that V_1 can be split into two parts: a part already present at $T = 0$ called Coleman-Weinberg potential V_{CW} [172] and a part explicitly depending on the temperature V_T. In addition we add a counterterm potential V_{CT} which we use later to specify our renormalization scheme in Sec. 5.2. To summarize, the effective potential used in this work can be decomposed as

$$V_{eff} = V_0 + V_{CW} + V_T + V_{CT} \ . \tag{5.2}$$

We will now explain V_0, V_{CW} and V_T in detail and elaborate on the counterterm potential V_{CT} in Sec. 5.2.

5.1.1. Tree-Level Potential

Imposing a softly broken $\mathbb{Z}_2$ symmetry for the two $SU(2)$ Higgs doublets of the 2HDM Φ_1 and Φ_2 to avoid flavor-changing neutral currents

$$\Phi_1 \longrightarrow \Phi_1 \ , \quad \Phi_2 \longrightarrow -\Phi_2 \ , \tag{5.3}$$

the tree-level potential of the 2HDM respecting renormalizability and invariance with respect to the SM gauge group is given by

$$\begin{aligned} V_0 = m_{11}^2 \Phi_1^\dagger \Phi_1 + m_{22}^2 \Phi_2^\dagger \Phi_2 - \left[m_{12}^2 \Phi_1^\dagger \Phi_2 + \text{h.c.} \right] + \frac{1}{2}\lambda_1 (\Phi_1^\dagger \Phi_1)^2 + \frac{1}{2}\lambda_2 (\Phi_2^\dagger \Phi_2)^2 \\ + \lambda_3 (\Phi_1^\dagger \Phi_1)(\Phi_2^\dagger \Phi_2) + \lambda_4 (\Phi_1^\dagger \Phi_2)(\Phi_2^\dagger \Phi_1) + \left[\frac{1}{2}\lambda_5 (\Phi_1^\dagger \Phi_2)^2 + \text{h.c.} \right] \ . \end{aligned} \tag{5.4}$$

While the dimensionful parameters $m_{11}^2,\ m_{22}^2$ and the dimensionless parameters $\lambda_i,\ i = 1...4$ are real, the dimensionful parameter m_{12}^2 and the dimensionless one λ_5 can in general be complex, providing new sources of CP violation in the Higgs sector. Here, all parameters are kept real. The term proportional to m_{12}^2 breaks the $\mathbb{Z}_2$ symmetry softly[14]. Decomposing the two Higgs doublets as

$$\Phi_1 = \frac{1}{\sqrt{2}} \begin{pmatrix} \rho_1 + \mathrm{i}\eta_1 \\ \zeta_1 + \mathrm{i}\psi_1 \end{pmatrix} \ , \qquad \Phi_2 = \frac{1}{\sqrt{2}} \begin{pmatrix} \rho_2 + \mathrm{i}\eta_2 \\ \zeta_2 + \mathrm{i}\psi_2 \end{pmatrix} \ , \tag{5.5}$$

we allow the real fields $\zeta_1,\ \zeta_2$ and ψ_2 to acquire a VEV. In order to parametrize the development of the VEVs in the minimization of the effective potential, we furnish these fields with field configurations $\omega_1,\ \omega_2$ and ω_3

$$\zeta_1 \longrightarrow \zeta_1 + \omega_1 \ , \tag{5.6}$$
$$\zeta_2 \longrightarrow \zeta_2 + \omega_2 \ , \tag{5.7}$$
$$\psi_2 \longrightarrow \psi_2 + \omega_3 \ . \tag{5.8}$$

The VEVs $\overline{\omega}_i,\ i = 1,2,3$ of the fields $\zeta_1,\ \zeta_2,\ \psi_2$, respectively, are the values of the field configuration $\{\omega\} = \{\omega_1,\ \omega_2,\ \omega_3\}$ in the global minimum of V_{eff}. By allowing a VEV for ψ_2 we allow for spontaneous CP violation. Without loss of generality ψ_1 does not acquire a VEV. Furthermore, we do not allow the fields $\rho_i,\ \eta_i,\ i = 1,2$, to develop a VEV to avoid the breaking of the $U(1)_{em}$. At $T = 0$ the field configurations in the global minimum of the potential, i.e. the VEVs, are related to the measured value $v \approx 246$ GeV by

$$\overline{\omega}_1 = v_1 := v \cos\beta \ , \tag{5.9}$$
$$\overline{\omega}_2 = v_2 := v \sin\beta \ , \tag{5.10}$$
$$\overline{\omega}_3 = v_3 = 0 \ , \tag{5.11}$$

such that

$$\tan\beta = \frac{v_2}{v_1} \ . \tag{5.12}$$

The angle β rotates the charged gauge eigenstates $\rho_i,\ \eta_i,\ i = 1,2$ to the physical charged mass eigenstates, namely the charged Higgs bosons $H^\pm$ with masses $M_{H^\pm}$ and the massless

[14] If a hard breaking of the $\mathbb{Z}_2$ symmetry is allowed, two additional terms with complex couplings are possible. This is not considered here.

	Type I	Type II	Lepton-Specific	Flipped
Up-type quarks	Φ_2	Φ_2	Φ_2	Φ_2
Down-type quarks	Φ_2	Φ_1	Φ_2	Φ_1
Leptons	Φ_2	Φ_1	Φ_1	Φ_2

Table 5.1: Specification of the couplings of the Higgs doublets to quarks and massive leptons

charged Goldstone bosons $G^\pm$ [15]. At the same time, this angle rotates the neutral states $\psi_i,\ i = 1, 2$ to a pseudo-scalar CP-odd mass eigenstate, A^0 with mass m_A, and a massless neutral Goldstone boson G^0. Diagonalizing the mass matrix of the $\zeta_i,\ i = 1, 2$ by a rotation with a mixing angle α yields two CP-even Higgs bosons H and h with masses m_H and m_h, respectively.

For a complete definition of the 2HDM Higgs sector the couplings of the Higgs doublets to the fermions have to be specified: in order to avoid flavor-changing neutral currents at tree-level, each of the up-type quarks, down-type quarks or massive leptons can receive its mass only due to one of the Higgs doublets. This can be achieved by augmenting the $\mathbb{Z}_2$ symmetry Eq. (5.3) by suitable $\mathbb{Z}_2$ symmetries for right-handed fermions in various ways, resulting in different combinations of couplings of the Higgs doublets to fermions called Type I, Type II, Lepton-Specific and Flipped. These are summarized in Table 5.1. Here, we investigate the 2HDM of Type I and Type II [16].

A necessary condition for a minimum of V_{eff} is that the first derivative of the potential vanishes at the field configuration of the minimum. The resulting conditions are called tadpole conditions. Knowing the present VEVs Eqs. (5.9)-(5.11) at $T = 0$, the tadpole conditions can be used to eliminate two parameters of the tree-level potential. By choice, we eliminate m_{11}^2 and m_{22}^2 by

$$m_{11}^2 = \frac{v_2}{v_1} m_{12}^2 - \frac{1}{2}\left(\lambda_1 v_1^2 + v_2^2(\lambda_3 + \lambda_4 + \lambda_5)\right) , \tag{5.13}$$

$$m_{22}^2 = \frac{v_1}{v_2} m_{12}^2 - \frac{1}{2}\left(\lambda_2 v_2^2 + v_1^2(\lambda_3 + \lambda_4 + \lambda_5)\right) . \tag{5.14}$$

For phenomenological studies it is convenient to transform the parameters of the potential Eq. (5.4) to physically meaningful parameters like masses and mixing angles. This way, experimental constraints can be fulfilled by appropriate input parameters easier, which makes a scan over the parameter space of the 2HDM more efficient compared to a scan over the parameters of Eq. (5.4). Using the relations given in [173] the resulting set of input parameters is given by

$$m_h,\ m_H,\ m_A,\ m_{H^\pm},\ m_{12}^2,\ \alpha,\ \tan\beta,\ v\ . \tag{5.15}$$

Here, we directly exploited Eqs. (5.13) and (5.14) and traded v_1 and v_2 for v and $\tan\beta$, which is convenient as v is fixed by experimental data.

[15] We work in Landau gauge.

[16] For the choice Eq. (5.3) the $\mathbb{Z}_2$ symmetries for right handed fermions for Type I are $f_R \to -f_R$ for all right-handed fermions f_R and the symmetries leading to Type II are given by $u_R \to -u_R$, $d_R \to d_R$ and $l_R \to l_R$, where u_R, d_R and l_R generically denote right handed up-type quarks, down-type quarks and massive leptons of any generation. More details are given in [14].

5.1.2. Coleman-Weinberg Potential

In a compact form the Coleman-Weinberg potential V_{CW} in Landau gauge[17] and $\overline{\text{MS}}$ renormalization for a particle i is given by [93]

$$V_{CW,i}(m_i^2(\{\omega\})) = \frac{n_i}{64\pi^2}(-1)^{2s_i}(m_i^2(\{\omega\}))^2 \left[\log\left(\frac{m_i^2(\{\omega\})}{\mu^2}\right) - c_i\right] , \tag{5.16}$$

where the spin of the particle is denoted by s_i and $m_i^2(\{\omega\})$ is the corresponding eigenvalue of the mass-squared matrix at the given field configuration $\{\omega\}$ [18]. The variable c_i takes values

$$c_i = \begin{cases} \frac{5}{6} , & i = W^\pm, Z, \gamma , \\ \frac{3}{2} , & \text{otherwise} , \end{cases} \tag{5.17}$$

μ is the renormalization scale which we set to the vacuum expectation value v and the factors n_i are the degrees of freedom of the particle i. The Coleman-Weinberg potential receives contributions from all quarks u, c, t, d, s, b, massive leptons e, μ, τ, physical Higgs bosons $h, H, A, H^\pm$, vector bosons $W^\pm, Z, \gamma$ and Goldstone bosons $G^0, G^\pm$. Although at $T = 0$ the photon is massless, the longitudinal component acquires a mass at $T \neq 0$ (see Sec. 5.1.3). Similarly, the Goldstone bosons are massless at the tree-level VEVs at $T = 0$, but not at field configurations and temperatures different from that, which is required in the minimization of the effective potential. Hence these particles are taken into account when constructing V_{CW}. In anticipation of the temperature potential in Sec. 5.1.3 we distinguish between longitudinal and transverse degrees of freedom for the gauge bosons and set

$$n_\Phi = 1 \ ; \ \Phi = \{h, H, A, H^+, H^-, G^0, G^+, G^-\} , \qquad n_{Z_T} = 2 , \qquad n_{Z_L} = 1 , \tag{5.18a}$$

$$n_q = 12 \ ; \ q = \{u, c, t, d, s, b\} , \qquad n_{W_T} = 4 , \qquad n_{W_L} = 2 , \tag{5.18b}$$

$$n_l = 4 \ ; \ l = \{e, \mu, \tau\} , \qquad n_{\gamma_T} = 2 , \qquad n_{\gamma_L} = 1 , \tag{5.18c}$$

where W_L (Z_L, γ_L) and W_T (Z_T, γ_L) denote the longitudinal and transverse W (Z, γ) bosons, respectively. Then, the particles taken into account in the calculation are

$$P = \{h, H, A, H^+, H^-, G^0, G^+, G^-, Z_T, Z_L, W_T, W_L, \gamma_T, \gamma_L, u, c, t, d, s, b, e, \mu, \tau\} , \tag{5.19}$$

and the complete Coleman-Weinberg potential V_{CW} is given by

$$V_{CW} = \sum_{i \in P} V_{CW,i}(m_i^2(\{\omega\})) . \tag{5.20}$$

5.1.3. Temperature Potential

The temperature dependent part of the effective potential V_T for each particle $i \in P$ of Eq. (5.19) at temperature T reads [93, 175]

$$V_{T,i}(m_i^2(\{\omega\}), T) = n_i \frac{T^4}{2\pi^2} J_\pm^{(i)}\left(\frac{m_i^2(\{\omega\})}{T^2}\right) . \tag{5.21}$$

[17] In Landau gauge the ghosts decouple and do not need to be considered further. For a discussion of the gauge dependence of the effective potential, see e.g. [92, 174] and references therein.

[18] Note that depending on the implementation of temperature corrected masses, the Coleman-Weinberg potential can become temperature dependent (see 5.1.3).

Henceforth the eigenvalues of the mass matrices at the field configuration $\{\omega\}$, $m_i^2(\{\omega\})$, will be abbreviated by m_i^2. The complete temperature potential is given by

$$V_T = \sum_{i \in P} V_{T,i}(m_i^2, T) \ . \tag{5.22}$$

It is known that at very high temperatures perturbation theory breaks down [176, 177]. In order to overcome this problem, temperature dependent contributions from diagrams of higher order can be resummed, leading to thermally corrected masses $\overline{m}_i^2(\{\omega\}, T)$, abbreviated by $\overline{m}_i^2$. This procedure is known as ring-improvement of the masses. Not all particles acquire a thermally corrected mass, but only scalars and longitudinal vector bosons. There are two ways of implementing the thermally corrected masses in the effective potential: in one case, called Arnold-Espinosa (AE) method [178], the thermally corrected masses are only inserted in the cubic term in the high-temperature expansion of J_- (see Eq. (5.27) below) which is critical for the breakdown of perturbation theory, whereas in the other case, called Parwani (PA) method [110], the thermally corrected masses are inserted everywhere in the high-temperature expansion of J_- and also in the Coleman-Weinberg potential. Specifically this means that in case of AE holds

$$J_\pm^{(i)} = \begin{cases} J_-\left(\frac{m_i^2}{T^2}\right) - \frac{\pi}{6T^3}(\overline{m}_i^3 - m_i^3) & i = W_L, Z_L, \gamma_L, \Phi \\ J_-\left(\frac{m_i^2}{T^2}\right) & i = W_T, Z_T \\ J_+\left(\frac{m_i^2}{T^2}\right) & i = f \ , \end{cases} \tag{5.23}$$

where Φ generically denotes all scalars and f all fermions included in P Eq. (5.19). In the PA case holds instead

$$J_\pm^{(i)} = \begin{cases} J_-\left(\frac{\overline{m}_i^2}{T^2}\right) & i = W_L, Z_L, \gamma_L, \Phi \\ J_-\left(\frac{m_i^2}{T^2}\right) & i = W_T, Z_T \\ J_+\left(\frac{m_i^2}{T^2}\right) & i = f \end{cases} \tag{5.24}$$

and the thermally corrected masses also have to be inserted in V_{CW} Eq. (5.16)[19]. The functions $J_\pm$ are given by

$$J_\pm\left(\frac{m_i^2}{T^2}\right) = \mp \int_0^\infty \mathrm{d}x \, x^2 \log\left[1 \pm e^{-\sqrt{x^2 + m_i^2/T^2}}\right] \tag{5.25}$$

and are thermal loop functions for fermions (J_+) and bosons (J_-). We take up an existing comparison of the two methods in the 2HDM [103] and perform our calculation using both methods. Although formally the difference is of higher order the results can change considerably as we will see in Sec. 5.3.

The integral in Eq. (5.25) can in principle be calculated numerically. However, this is computationally expensive and therefore not well-suited for the minimization of the effective potential V_{eff} since at each temperature T the potential has to be evaluated at a multitude of field configurations $\{\omega\}$ to find the global minimum. Instead, it is more convenient to use

[19] Hence, only in the PA, but not in the AE case the Coleman-Weinberg potential Eq. (5.16) depends explicitly on the temperature.

expansions of the integrals in m_i^2/T^2 as for instance given in [103]. For small m_i^2/T^2 the expansions read

$$\begin{aligned} J_{+,\mathrm{s}}(m_i^2/T^2, n) = &-\frac{7\pi^4}{360} + \frac{\pi^2}{24}\frac{m_i^2}{T^2} + \frac{1}{32}\frac{m_i^4}{T^4}\left(\log\left(\frac{m_i^2}{T^2}\right) - c_+\right) \\ &- \pi^2\frac{m_i^2}{T^2}\sum_{l=2}^{n}\left(-\frac{1}{4\pi^2}\frac{m_i^2}{T^2}\right)^l \frac{(2l-3)!!\zeta(2l-1)}{(2l)!!(l+1)}\left(2^{2l-1}-1\right) , \end{aligned} \tag{5.26}$$

$$\begin{aligned} J_{-,\mathrm{s}}(m_i^2/T^2, n) = &-\frac{\pi^4}{45} + \frac{\pi^2}{12}\frac{m_i^2}{T^2} - \frac{\pi}{6}\left(\frac{m_i^2}{T^2}\right)^{3/2} - \frac{1}{32}\frac{m^4}{T^4}\left(\log\left(\frac{m_i^2}{T^2}\right) - c_-\right) \\ &+ \pi^2\frac{m_i^2}{T^2}\sum_{l=2}^{n}\left(-\frac{1}{4\pi^2}\frac{m_i^2}{T^2}\right)^l \frac{(2l-3)!!\zeta(2l-1)}{(2l)!!(l+1)} , \end{aligned} \tag{5.27}$$

with $c_+ = 3/2 + 2\log\pi - 2\gamma_E$ and $c_- = c_+ + 2\log 4$. The variable γ_E denotes the Euler-Mascheroni constant, $\zeta(x)$ is the Riemann ζ-function and $(x)!!$ denotes the double factorial. In case of large m_i^2/T^2 the expansion of the integrals is given by

$$J_{\pm,\mathrm{l}}(m_i^2/T^2, n) = -\exp\left(-\left(\frac{m_i^2}{T^2}\right)^{1/2}\right)\left(\frac{\pi}{2}\left(\frac{m_i^2}{T^2}\right)^{3/2}\right)^{1/2}\sum_{l=0}^{n}\frac{1}{2^l l!}\frac{\Gamma(5/2+l)}{\Gamma(5/2-l)}\left(\frac{m_i^2}{T^2}\right)^{-l/2} \tag{5.28}$$

for both bosons and fermions with $\Gamma(x)$ denoting the Euler Gamma function. For intermediate m_i^2/T^2 the two expansions either for bosons or fermions are connected continuously: the intersection of the derivatives of Eq. (5.26) and Eq. (5.28) and of Eq. (5.27) and Eq. (5.28), respectively, are determined and at the intersection a small constant shift is added to the expansions $J_{+,\mathrm{s}}$ and $J_{-,\mathrm{s}}$ in order to make the connection of the two expansions continuous. In the expansion $J_{+,\mathrm{s}}$ we use $n = 4$ whereas in $J_{-,\mathrm{s}}$ and $J_{\pm,\mathrm{l}}$ we use $n = 3$ in accordance with [103]. The locations of the intersections for fermions x_+ and bosons x_- and the corresponding shifts δ_+ and δ_- are found to be

$$x_+ = 2.2161 , \qquad \delta_+ = -0.015603 , \tag{5.29}$$

$$x_- = 9.4692 , \qquad \delta_- = 0.0063109 . \tag{5.30}$$

Adding the shifts to $J_{+,\mathrm{s}}$ and $J_{-,\mathrm{s}}$ or subtracting them from $J_{\pm,\mathrm{l}}$ is in general a matter of choice. However, for large m_i^2/T^2 the value of the integral approaches 0, such that if a finite shift as in Eqs. (5.29) and (5.30) is subtracted from $J_{\pm,\mathrm{l}}$, the result approaches the constant shift rather than 0 and thereby may alter the result. Hence we add the shifts Eq. (5.29) and Eq. (5.30) to the expansions $J_{+,\mathrm{s}}$ and $J_{-,\mathrm{s}}$, where this problem does not occur as the integral approaches a value much larger than the value of the shifts. Comparing this procedure of approximating the temperature integrals Eq. (5.25) to the numerical evaluation of the integrals we can quantify the error to be less than 1% in the bosonic case and less than 1.3% in the fermionic case. This also shows that the chosen orders of the expansions n are sufficient to reach a good enough accuracy.

For unphysical field configurations $\{\omega\}$ the scalars can obtain negative masses squared, in which case the above expansions for the integrals do not hold anymore. In general this is not an issue, since in the global minimum the mass-squared matrix is positive semi-definite and accordingly in the global minimum negative m_i^2 can never occur. However, in the course of the numerical minimization of the potential the integrals Eq. (5.25) also have to be evaluated at these configurations. In this case, the real part of the numerical evaluation of J_- is taken

as result, which is the relevant quantity for finding the global minimum [179]. Practically, the integral has been evaluated numerically once and for all at many points in a sufficient range of m_i^2/T^2 and a linear interpolation between these points has been used for the continuous evaluation.

5.2. Renormalization of the Effective Potential

Following the explanation in Sec. 5.1.1 we would like to use the physical parameters Eq. (5.15) for the scan over the parameter space of the 2HDM to look for viable parameter points compatible with theoretical and experimental constraints. Using these parameters in the one-loop effective potential, however, leads to a mismatch of the input parameters which are used for all constraints in the scan, and the parameters calculated from the one-loop potential. In this sense, the input parameters can be understood as tree-level parameters, while the masses and angles calculated from the one-loop potential can be understood as one-loop parameters. Since we would like to perform all constraints with the most precise parameters, we should use the one-loop parameters for the checks. Practically this renders the scan over the parameter space inefficient and the advantage of choosing the set Eq. (5.15) as inputs is lost for two reasons: first, the calculation of the one-loop parameters from the effective potential is time consuming and second, the one-loop corrections can be very large such that the scan efficiency with respect to theoretical and experimental constraints is reduced[20]. In order to restore the advantages of scanning over physical parameters Eq. (5.15) we perform a specific renormalization: the Coleman-Weinberg potential Eq. (5.16) is already renormalized in the $\overline{\text{MS}}$-scheme, so no divergences have to be absorbed by renormalization any more. However, we are still free to fix the finite terms to comply with renormalization conditions of our choice. By suitable conditions, the finite terms are chosen such that the one-loop masses and mixing angles remain at their tree-level values.
To this end a counterterm for each parameter of the tree-level potential Eq. (5.4) is introduced, leading to

$$\begin{aligned} V_{CT} = {} & \delta m_{11}^2 \Phi_1^\dagger \Phi_1 + \delta m_{22}^2 \Phi_2^\dagger \Phi_2 - \left[\delta m_{12}^2 \Phi_1^\dagger \Phi_2 + \text{h.c.}\right] + \frac{1}{2}\delta\lambda_1 (\Phi_1^\dagger \Phi_1)^2 \\ & + \frac{1}{2}\delta\lambda_2 (\Phi_2^\dagger \Phi_2)^2 + \delta\lambda_3 (\Phi_1^\dagger \Phi_1)(\Phi_2^\dagger \Phi_2) + \delta\lambda_4 (\Phi_1^\dagger \Phi_2)(\Phi_2^\dagger \Phi_1) \\ & + \left[\frac{1}{2}\delta\lambda_5 (\Phi_1^\dagger \Phi_2)^2 + \text{h.c.}\right] . \end{aligned} \tag{5.31}$$

The counterterms are determined by the conditions presented in the next section.

5.2.1. Renormalization Conditions

The renormalization conditions relate the counterterm potential V_{CT} of Eq. (5.31) to the Coleman-Weinberg potential V_{CW}. By contrast, the temperature potential V_T does not contribute because the parameter scan and the check for all constraints are done at $T = 0$ [21]. The desired properties can be achieved by conditions involving the first and second derivative of the potential, since they determine the position of the minimum and the mass matrix of the Higgs bosons which leads to the mass eigenvalues and mixing angles α and β. The conditions for the first derivative are given by

$$\partial_{\phi_i} V_{CT}(\phi)|_{\phi=\langle\phi\rangle_{T=0}} = -\partial_{\phi_i} V_{CW}(\phi)|_{\phi=\langle\phi\rangle_{T=0}} \ , \ i = 1...8 \tag{5.32}$$

[20] Also the hierarchies of the Higgs bosons can change due to one-loop contributions.
[21] The current temperature of the cosmic microwave background $T \approx 2.7$ K ≈ 0.23 meV is negligible compared to the electroweak scale and can be ignored for studying the electroweak phase transition.

where ϕ comprises all component fields of the Higgs doublets according to Eq. (5.5), i.e.

$$\phi = \{\rho_1, \eta_1, \rho_2, \eta_2, \zeta_1, \psi_1, \zeta_2, \psi_2\} \tag{5.33}$$

and $\langle\phi\rangle_{T=0}$ are the corresponding VEVs of the component fields at $T = 0$ according to Eqs. (5.9)-(5.11). The conditions for the second derivative read

$$\partial_{\phi_i}\partial_{\phi_j} V_{CT}(\phi)|_{\phi=\langle\phi\rangle_{T=0}} = -\partial_{\phi_i}\partial_{\phi_j} V_{CW}(\phi)|_{\phi=\langle\phi\rangle_{T=0}} \ , \ i,j = 1...8 \ . \tag{5.34}$$

In principle, Eq. (5.32) poses eight conditions, while Eq. (5.34) embodies an 8×8 matrix-equation. Even though many of the resulting equations are not independent and drop out, the eight counterterms of Eq. (5.31) are not sufficient to solve the system. Consequently in the literature alternatives have been studied, involving only the first derivatives and masses of the Higgs bosons, or subsets of them [103, 106, 107, 180, 181]. Here, a new approach involving the first derivatives, masses and for the first time also mixing angles of the Higgs sector is pursued and explained in the following. As an approximation, we do not demand the conditions Eq. (5.34) for the complete matrix, but only for those entries corresponding to the physical Higgs bosons $h, H, A, H^\pm$. However, Eq. (5.34) is formulated in the gauge basis, where it is not possible to assign an entry to a certain physical Higgs boson. This problem can be overcome, by rotating Eq. (5.34) with the tree-level rotation matrix from gauge- to mass-eigenstates. In the rotated system we can then identify certain entries with mass eigenstates and demand the renormalization condition only for the physical Higgs bosons: a 2×2 matrix for the charged Higgs bosons $H^\pm$

$$\partial_{\phi_i}\partial_{\phi_j} V_{\mathrm{CT}}(\phi)|_{\phi=\langle\phi\rangle_{T=0}}|^{H^\pm}_{\mathrm{mass}} = -\partial_{\phi_i}\partial_{\phi_j} V_{\mathrm{CW}}(\phi)|_{\phi=\langle\phi\rangle_{T=0}}|^{H^\pm}_{\mathrm{mass}} \tag{5.35}$$

and a 3×3 matrix for the neutral Higgs bosons, which further decomposes into a 2×2 matrix for the CP-even Higgs bosons h, H and an entry for the CP-odd Higgs A

$$\partial_{\phi_i}\partial_{\phi_j} V_{\mathrm{CT}}(\phi)|_{\phi=\langle\phi\rangle_{T=0}}|^{h,H,A}_{\mathrm{mass}} = -\partial_{\phi_i}\partial_{\phi_j} V_{\mathrm{CW}}(\phi)|_{\phi=\langle\phi\rangle_{T=0}}|^{h,H,A}_{\mathrm{mass}} \ . \tag{5.36}$$

In the above equations the subscript 'mass' indicates that the equations are posed in the system rotated to mass eigenstates and the superscripts $H^\pm$ and h, H, A illustrate that only the entries corresponding to these physical states are considered.
From these conditions for first and second derivatives, Eqs. (5.32), (5.35) and (5.36), one obtains seven independent renormalization conditions, fixing seven of the eight counterterms in V_{CT} Eq. (5.31). Inserting the field configurations Eqs. (5.6)-(5.8) and setting all fields ϕ to zero as required for the numerical minimization, it is apparent that the counterterms $\delta\lambda_3$ and $\delta\lambda_4$ only appear in a sum. Hence we choose to set $\delta\lambda_4 = 0$ as further condition.
Eventually, by our renormalization prescription we are able to keep a local minimum at $T = 0$ at $v \pm 2$ GeV, which is checked to be the global minimum numerically, and the masses and mixing angles of the Higgs sector are preserved at their tree-level values up to numerical fluctuations.

5.2.2. First and Second Derivative of the Coleman-Weinberg Potential

For the renormalization conditions Eqs. (5.32), (5.35) and (5.36) the first and second derivative of the Coleman-Weinberg potential in the gauge basis are required. Starting from the potential for scalars and interaction Lagrangians for gauge bosons and fermions involving scalar fields, explicit formulae for the derivatives of V_{CW} have been derived recently in [182]. This is a non-trivial task since it involves derivatives of the field-dependent matrix logarithm

in Eq. (5.16). Here only the starting points for the calculation implementing the procedure of [182] are explained.
The scalar potential required is the tree-level potential given in Eq. (5.4). The interaction of electroweak gauge bosons and the scalar fields is embodied in the covariant derivative

$$\mathrm{i}D_\mu = \mathrm{i}\partial_\mu - \frac{g}{2}\vec{\sigma}\vec{W}_\mu - \frac{g'}{2}B_\mu \tag{5.37}$$

for the kinetic term of the scalar fields, where the couplings g and g' (W_μ and B_μ) are the $SU(2)_L$ and $U(1)_Y$ gauge couplings (fields) and $\vec{\sigma}$ is the vector of Pauli matrices. The interaction Lagrangian of the scalars with fermions has to be provided in Weyl notation. Exemplarily, the term in the interaction Lagrangian for fermions $\mathcal{L}_F$ giving rise to the masses of up-type quarks reads

$$\mathcal{L}_F \propto u_{iR} Y^u_{ij} (\Phi_2^c)^\dagger \begin{pmatrix} u_{jL} \\ V^{\mathrm{CKM}}_{jk} d_{kL} \end{pmatrix} , \tag{5.38}$$

where $i, j, k = 1...3$ are generation indices for up- and down-type quarks, u_{iR} is a right-handed up-type quark in Weyl notation of generation i, u_{jL} and d_{kL} are left-handed up- and down-type quarks in Weyl fermion notation of generation j and k, respectively. The matrix Y^u_{ij} is the Yukawa coupling matrix and is given by

$$Y^u_{ij} = y^{u_i}\delta_{ij} , \tag{5.39}$$

where y^{u_i} is the Yukawa coupling of the quark u_i. V^{CKM} denotes the CKM matrix and Φ_2 is the second Higgs doublet of Eq. (5.5) with

$$(\Phi_2^c)^\dagger = \left[\begin{pmatrix} 0 & 1 \\ -1 & 0 \end{pmatrix} \Phi_2^* \right]^\dagger = \left[\frac{1}{\sqrt{2}} \begin{pmatrix} \zeta_2 - \mathrm{i}\psi_2 \\ -\rho_2 + \mathrm{i}\eta_2 \end{pmatrix} \right]^\dagger . \tag{5.40}$$

The terms for down-type quarks and leptons are obtained similarly, but the Higgs doublet coupling to them has to be chosen according to the 2HDM type as shown in Tab. 5.1. With the second derivative of V_{CW} at hand, the one-loop corrections to masses and mixing angles in the approximation of vanishing external momenta can be determined. We find that the corrections can be substantial, including a change of the hierarchy of the Higgs bosons. This demonstrates the need for a proper renormalization prescription for an efficient scan over the parameter space.

5.2.3. Goldstone Problem

The second derivative of the Coleman-Weinberg potential required for fixing the counterterms by the renormalization conditions Eqs. (5.35) and (5.36) yields infrared divergences connected to the Goldstone bosons being massless in Landau gauge. These divergences can be understood as follows: the second derivative of V_{CW} corresponds to one-loop corrections to the scalar masses and hence to self-energies in the diagrammatic terminology. The source of the divergences can then be understood by looking at Fig. 5.1. Neglecting constant terms and the ultraviolet divergent part which is canceled by the $\overline{\mathrm{MS}}$ renormalization the contribution of this self-energy Σ_h scales as

$$\Sigma_h(p^2) \propto \log\left(\frac{p^2}{\mu^2}\right) , \tag{5.41}$$

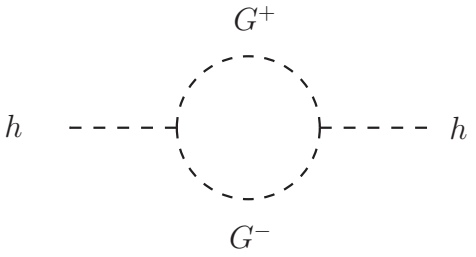

Figure 5.1: Feynman diagram for a Higgs boson self-energy leading to an infrared divergence in the limit of vanishing external momenta in Landau gauge.

where p^2 is the momentum of the external Higgs boson squared and μ^2 is the renormalization scale. The effective potential approach corresponds to the calculation with vanishing external momenta. In this limit, however, the logarithm in Eq. (5.41) diverges

$$\log\left(\frac{p^2}{\mu^2}\right) \xrightarrow{p^2\to 0} -\infty \ , \tag{5.42}$$

which is a well-known problem [103, 106, 107, 182–184]. In the effective potential this divergence is encoded in the logarithm of the Coleman-Weinberg potential Eq. (5.16). In previous works either the logarithm was redefined to capture on-shell contributions [103], or an infrared regulator mass for the Goldstone boson m_G was introduced [106, 107, 180], motivated by the observation, that the self-energy $\Sigma_h(m_G)$ for a massive Goldstone boson and for vanishing external momenta scales as

$$\Sigma_h(m_G) \propto \log\left(\frac{m_G^2}{\mu^2}\right) \ . \tag{5.43}$$

In this work, we follow another approach: solely in the effective potential approach it is not possible to eliminate this divergence. However, it has been shown in [185] and argued in [182, 184] that the divergence is spurious and cancels, when building up the self-energy with full momentum dependence out of the second derivative of the Coleman-Weinberg potential and the diagrammatically calculated self-energies for the momentum dependent part. Schematically this means

$$\Sigma_h(p^2) = \partial^2 V_{CW} + \Big(\Sigma_h(p^2) - \Sigma_h(0)\Big) \ , \tag{5.44}$$

where $\partial^2 V_{CW}$ abbreviates the second derivative of the Coleman-Weinberg potential. After the cancelation of the divergence on the right-hand side of Eq. (5.44), the limit of vanishing external momenta can be taken safely and one obtains a finite result for the second derivative of the Coleman-Weinberg potential. The validity of this approach in our case has been checked explicitly with the calculations of [186, 187]. In the actual implementation, this amounts to leaving away only the singular part of the second derivative for the Goldstone bosons [182][22].

5.3. Implementation and Results

5.3.1. Implementation, Experimental Constraints and Parameter Settings

The entire calculation has been implemented in `Mathematica`. Starting from the potential and interaction Lagrangians as explained in Sec. 5.2.2 first the derivatives of the Coleman-

[22] The non-singular part of Eq. (5.16), namely the term proportional to c_i must not be ignored.

# points	m_h	m_H	m_A	$m_{H^\pm}$	m_{12}^2	$\tan(\beta)$
	in GeV				in GeV^2	
10^5	$30-120$	$m_{h_{125}}$	$30-1000$	$65-1000$	$0-5\times10^5$	$1-35$

Table 5.2: Parameter ranges for the scan performed in the 2HDM Type I. The first column specifies the number of points generated. This scan has been performed in [108].

# points	m_h	m_H	m_A	$m_{H^\pm}$	m_{12}^2	$\tan(\beta)$
	in GeV				in GeV^2	
10^6	$m_{h_{125}}$	$130-1000$	$30-1000$	$480-1000$	$0-5\times10^5$	$0.1-35$

Table 5.3: Parameter ranges for the scan in the 2HDM Type II. The first column specifies the number of points generated. This scan has been performed in [108].

Weinberg potential are calculated for a given set of input parameters Eq. (5.15) in order to determine the counterterms for the counterterm potential Eq. (5.31). In a second step, the effective potential Eq. (5.2) is constructed and minimized for a given temperature T [23]. In the minimization procedure, the global minimum is determined by variations in the field configuration space $\{\omega\}$ for all fields which we allow to acquire a VEV (Eqs. (5.6)-(5.8)). This is done for temperatures from $T = 0$ to $T = 300$ GeV [24] in order to extract the critical temperature by the procedure explained in Sec. 5.3.2.
The calculation has been checked by an independent calculation (see [108]) that is also used for the phenomenological investigation of the 2HDM with respect to a strong EWPT.

The parameter scan has been performed at $T = 0$ by `ScannerS` [188, 189], which directly checks for boundedness of the potential from below and for tree-level perturbative unitarity by relations from [190] and [191], respectively. It is then verified, that the global minimum at tree-level is CP-even [192]. Moreover, we have checked the S, T and U parameters [193] via relations given in [194, 195] and demanded compatibility with the results from [196] within two standard deviations. Furthermore, constraints resulting from the measurement of R_b [197, 198] and $B \longrightarrow X_s\gamma$ [198–200] were imposed, together with the reported limit [201]

$$m_{H^\pm} > 480 \text{ GeV} \tag{5.45}$$

for the 2HDM Type II[25]. For Type I, the limit is weaker and depends on $\tan\beta$. Although generally much weaker, also the corresponding limits from LEP [203] and LHC [204, 205] were taken into account. In order to comply with the Higgs data predictions for production cross sections and branching ratios have been obtained by `SusHi` [133, 206] and `HDECAY` [131–133] and were checked using `HiggsBounds` [127–130] for the exclusion limits. For the observed signal, the signal strengths were calculated and requested to be within the two times one sigma bound of [207]. More details are given in [108].
The range of the input parameters chosen for the phenomenological analysis can be inferred from Tabs. 5.2 and 5.3 for the 2HDM Type I and Type II, respectively. Here, in the Type

[23] It is sufficient to consider only the real part of the potential for the minimization [179].
[24] With our choice for the criterion for a strong first order PT Eq. (2.39) no strong PTs can occur for $T > v$ and hence our choice covers the entire allowed range.
[25] The recently reported bounds [202] were published after the work has been finished and are not included.

II scan the light CP-even Higgs boson was chosen to be the observed Higgs h_{125} with a mass of $m_{h_{125}} = 125.09$ GeV [47], whereas in the Type I scan the heavy CP-even Higgs was chosen to be h_{125}. A spacing of 5 GeV between the SM-like Higgs h_{125} and other Higgs bosons was required to avoid overlapping signals. Moreover, the ranges for the masses have been chosen according to phenomenological relevance and observability at current colliders. The range for the charged Higgs boson in Type II starts at the bound Eq. (5.45). In order to ensure that the tree-level minimum is the global one the parameter m_{12}^2 was required to be positive [192], and the lower bound for $\tan\beta$ in Type I was chosen such, that it leaves away a part of the parameter space which is already excluded. The upper bound on $\tan\beta$ has been set by choice, but does not influence our results noticeably since parameter points with a strong phase transition tend to cluster at low values of $\tan\beta$. The angle α has been varied in

$$-\frac{\pi}{2} \leq \alpha \leq \frac{\pi}{2} \tag{5.46}$$

and the VEV v was set to $v = 246.22$ GeV. For the fine structure constant α_{EM} at zero momentum transfer and at the scale M_Z^2 and for the W and Z boson masses M_W and M_Z we have used [125, 208]

$$\alpha_{\text{EM}}^{-1}(0) = 137.0359997\ , \qquad \alpha_{\text{EM}}^{-1}(M_Z^2) = 128.962\ , \tag{5.47a}$$

$$M_W = 80.385\ \text{GeV}\ , \qquad M_Z = 91.1876\ \text{GeV}\ . \tag{5.47b}$$

The quark masses were taken to be [208, 209]

$$m_u = 100\ \text{MeV}\ , \quad m_c = 1.51\ \text{GeV}\ , \quad m_t = 172.5\ \text{GeV}\ , \tag{5.48a}$$

$$m_d = 100\ \text{MeV}\ , \quad m_s = 100\ \text{MeV}\ , \quad m_b = 4.92\ \text{GeV}\ , \tag{5.48b}$$

the lepton masses were chosen as [125, 208]

$$m_e = 0.510998928\ \text{MeV}\ , \quad m_\mu = 105.6583715\ \text{MeV}\ , \quad m_\tau = 1.77682\ \text{GeV}\ , \tag{5.49}$$

and the CKM matrix has been set to [125]

$$V^{\text{CKM}} = \begin{pmatrix} 0.97427 & 0.22536 & 0.00355 \\ -0.22522 & 0.97343 & 0.0414 \\ 0.00886 & -0.0405 & 0.99914 \end{pmatrix}\ . \tag{5.50}$$

For determining the counterterms, we set $V^{\text{CKM}} = \mathbb{1}$ for simplicity.
All parameter points shown in the results in the next section fulfill all theoretical and experimental constraints explained above.

5.3.2. Results

In Sec. 2.3 the criterion for a phase transition to be classified as strong first order was introduced in Eq. (2.39). By inspecting Fig. 5.2 we explain how the value of

$$\xi_c := \frac{v_c}{T_c} \tag{5.51}$$

is extracted from the result of the calculation explained above. The result of the calculation for one parameter point of the Type II scan is shown on the left-hand side of Fig. 5.2. For a

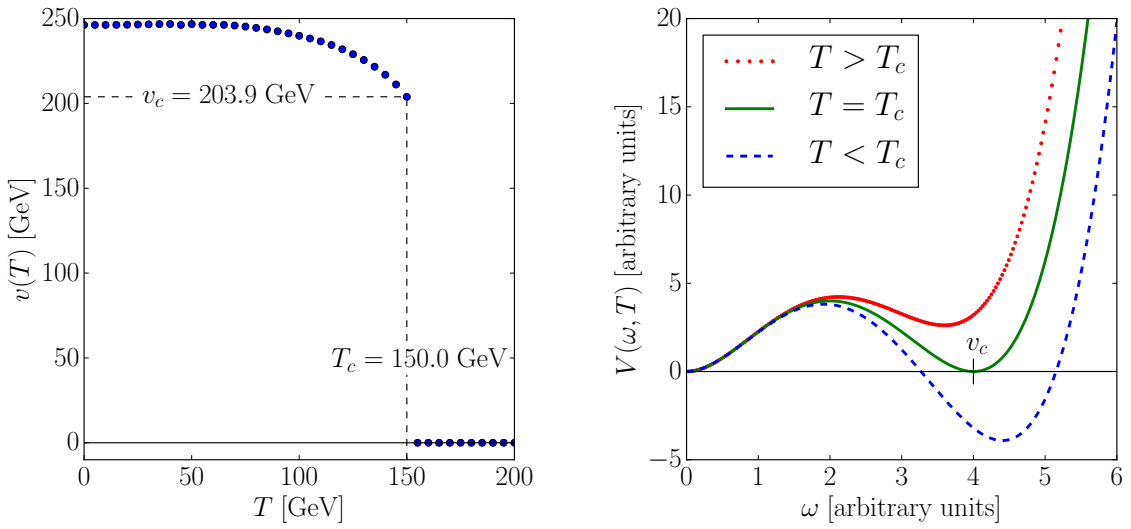

Figure 5.2: Vacuum expectation value $v(T)$ with respect to the temperature resulting from the calculation using the AE method (left) and the one-dimensional potential for different temperatures explained in the introduction 2.4.

sufficient range of the temperature the effective potential Eq. (5.2) is minimized globally and the VEV $v(T)$ is determined by

$$v^2(T) = \overline{\omega}_1^2(T) + \overline{\omega}_2^2(T) + \overline{\omega}_3^2(T) \tag{5.52}$$

and plotted with respect to the temperature. On the right-hand side of Fig. 5.2 the plot of a one-dimensional potential shown in Sec. 2.3 is repeated for convenience. The curve on the right-hand side representing the situation at $T > T_c$ where the global minimum is at $v(T) = 0$ corresponds to the points in our results for temperatures above 150 GeV where the VEV is found to be zero. At these temperatures, the electroweak symmetry is not broken. As explained in Sec. 2.3 the temperature where two degenerate minima occur is the critical temperature T_c (green curve). This temperature can be extracted from our results by the position of the jump, which is at $T_c = 150.0$ GeV for this parameter point, since at the critical temperature the global minimum jumps from zero to a non-zero value. The critical VEV v_c is then given by the height of the jump, found to be $v_c = 203.9$ GeV. This height corresponds to the distance from zero to v_c in the green curve for the potential on the right-hand side of Fig. 5.2. For temperatures lower than 150 GeV the VEV continuously moves to higher values until it reaches $v = 246.22$ GeV at $T = 0$. Such temperatures correspond to situations like the blue curve on the right-hand side. Hence at these temperatures the electroweak symmetry is broken. To summarize, for each parameter point the critical temperature T_c is determined to be the highest temperature where the VEV is found to be non-zero, and the v_c is set to the VEV at this temperature[26]. From these two quantities the condition for a strong first order phase transition is determined. In this case we have

$$\xi_c = \frac{203.9}{150.0} \approx 1.36 \ , \tag{5.53}$$

so with our criterion Eq. (2.39) this parameter point leads to a strong first order phase transition. In general, in the analysis no parameter point generated a non-zero CP-breaking

[26]Note that the spacing in temperature between two evaluations in Fig. 5.2 (left) was chosen to be 5 GeV for simplicity. In the version used for the phenomenological analysis below a bisection procedure was used until T_c is determined up to a precision of 0.01 GeV.

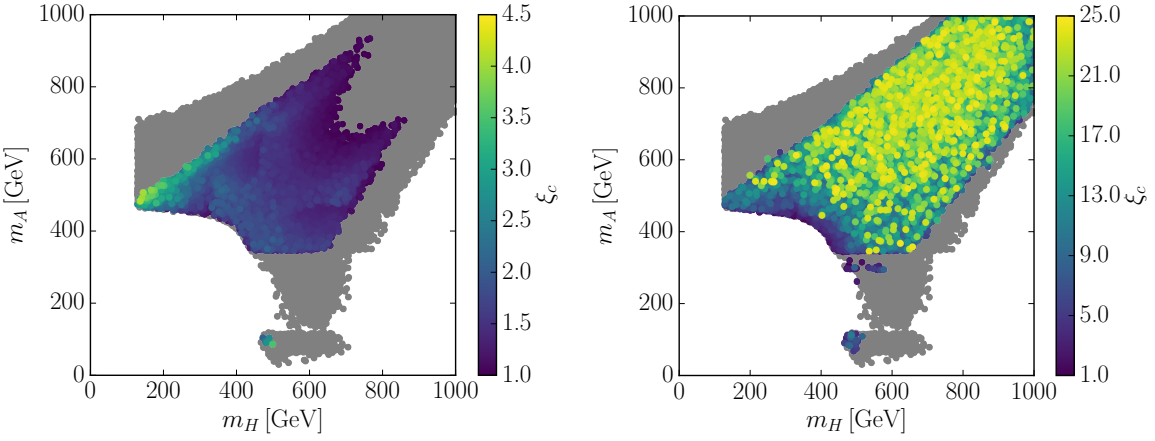

(a) Results obtained with the AE method. This figure has been published in [108].

(b) Results obtained with the PA method.

Figure 5.3: Results for $h \equiv h_{125}$ for the 2HDM Type II (Tab. 5.3). All parameter points found in the scan are shown in grey, colored are those with additionally a strong first order PT, where the strength ξ_c according to Eq. (5.51) is given by the color code.

VEV ϖ_3 at finite temperature and we will not investigate the possibility of spontaneous CP violation further.
In the following phenomenological analysis first we focus on the light CP-even Higgs being the SM-like Higgs boson considering the Type II model in 5.3.2.1, and second investigate the Type I model with the heavy CP-even scalar as SM-like Higgs boson in 5.3.2.2. The complementary cases, i.e. $h \equiv h_{125}$ in the Type I model and $H \equiv h_{125}$ in the Type II model are included in [108].

5.3.2.1. Results for the 2HDM Type II

We start discussing the results for our parameter scan of Tab. 5.3 explained in Sec. 5.3.1 by comparing the AE and PA methods (see 5.1.3) in Fig. 5.3. On the left-(right-)hand side the results for the AE (PA) method are shown in the $m_H - m_A$ plane. All parameter points found in the scan that respect all theoretical and experimental constraints are drawn in grey and points that additionally have a strong first order PT are colored, with the strength of the PT indicated by the color code. First, we observe that the PA method leads to many more points with a strong PT than the AE method. Although for masses up to about 800 GeV the regions with strong PTs are similar, in the PA method also the region of masses up to 1 TeV is populated. Moreover, the PTs are much stronger in the results for the PA method, with values of ξ_c up to 25. Given that $v_c \leq v = 246.22$ GeV for $\xi_c \geq 1$ implies that the PTs with a strength of about 25 happen at very low temperatures of about ten GeV. This means that the potential Eq. (5.2) using the PA method is very sensitive to small deviations of the temperature from zero, although for small temperatures it is expected that the temperature independent part of the one-loop corrections V_{CW} is dominant and only for increasing temperature the temperature potential V_T gains importance because it scales as T^4 (*cf.* Fig. 5.2 (left), where the AE method was used). This means, that the temperature corrections introduced through the ring-improvement in V_T and in V_{CW} are such, that they dominate the evolution of the potential already at low temperatures. This is unexpected

since the ring-improvement amounts to adding corrections of higher order in perturbation theory relevant at high temperatures. Consequently the strength of the PTs found in the PA method indicates that the perturbative series has collapsed. This is an effect of truncating the perturbative series at the one-loop level and the problem is resolved at higher orders [178]. Since we are working at the one-loop level we henceforth focus on results obtained by the AE method which provides a consistent resummation in this case [108, 178][27]. A comparison of our results with [180] where the PA method was used can be found in [108].

We now focus on the shape of all points found in the parameter scan in the $m_H - m_A$ plane Fig. 5.3(a). The quadrant cut out for low masses is a consequence of the bound Eq. (5.45) in combination with the electroweak precision tests: due to the latter, one of A or H is forced to be close in mass to the charged Higgs, which is limited from below by Eq. (5.45). The upper bound of m_H for low m_A and the upper bound of m_A for low m_H result from the relations for the masses of the heavy Higgs bosons in the 2HDM and the bounds on the parameters from perturbative unitarity constraints. The masses of the heavy Higgs bosons are given by [187]

$$m_{\phi_{\text{heavy}}} = M^2 + f(\lambda_i)v^2 + \mathcal{O}(v^4/M^2) \ , \tag{5.54}$$

where $M^2 = m_{12}^2/(\sin\beta\cos\beta)$, $f(\lambda_i)$ denotes a function of λ_i, $i = 1...5$. Since in these two regions one of the heavy Higgs bosons is rather light, the M^2 term setting a common scale of the masses cannot be large while the splitting between the Higgs bosons is governed by the function $f(\lambda_i)$. Since the couplings λ_i are bound by perturbative unitarity however, the induced differences of the masses of the heavy Higgs bosons are also limited. This holds for both regions pointed out. In the region of high m_A and m_H, the overall scale M^2 can be large, opening up the region where all Higgs bosons are heavy.
Considering now the region leading to a strong PT, we observe a gap at 130 GeV $\leq m_A \leq$ 340 GeV. On the one hand this region of m_A is experimentally much more constrained than others due to the kinematic suppression of the decay $A \longrightarrow t\bar{t}$ in favor of the decay $A \longrightarrow Zh$ which is strongly constrained by searches at the LHC. On the other hand, in this region H is rather heavy, such that small deviations from the alignment limit which cause H to acquire a VEV suppress the strength of the PT. In consequence, by requiring a strong first order PT this range of m_A is excluded. As the constraints for $m_A \leq 120$ GeV are less stringent there are more valid parameter points in this region, including some with a strong PT.
In the plot Fig. 5.4(a) we show a heat map of all parameter points found to be compatible with the applied constraints in the $m_H - m_A$ plane. The color code indicates the relative frequency of points in a bin with respect to the maximum number of points in any of the bins. The shape is identical to the shape of the grey points of Fig. 5.3(a). However, the majority of the points is located where both m_H and m_A are about 500 GeV or larger, in particular in the diagonal regime. This is the region, where the common scale M^2 dominates the masses of the heavy Higgs bosons according to Eq. (5.54), which brings them closely together. This falls into the decoupling limit where the couplings of the light CP-even Higgs boson are similar to the ones of the SM Higgs, explaining why many points are found here. Requiring in addition a strong first order PT as shown in the right plot Fig. 5.4(b) this is not pronounced any more. The points shown here correspond to the colored ones in Fig. 5.3(a). Apparently the region of high masses for all heavy scalars is not favored by a strong PT.
The possibility of a preferred hierarchy of the heavy Higgs bosons can be studied in Fig. 5.5. In Fig. 5.5(a) all parameter points found in the scan are plotted as a heat map in the plane of the mass differences $m_H - m_{H^\pm}$ and $m_A - m_{H^\pm}$, where the relative frequency of points

[27] The smallest values of T_c found with the AE method are about 57 GeV.

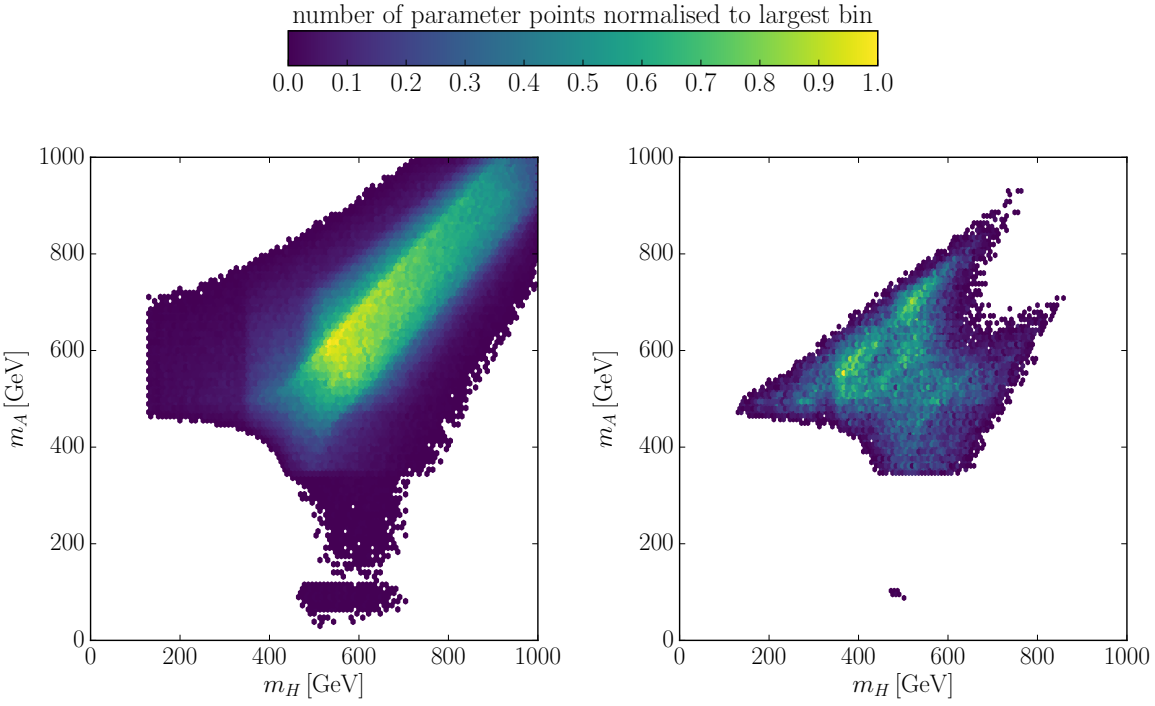

(a) All scenarios found in the scan.

(b) Scenarios additionally fulfilling $\xi_c > 1$ using the AE method.

Figure 5.4: Scenarios of the Type II scan with $h \equiv h_{125}$ in the $m_H - m_A$ plane. The relative frequency of the parameter points normalized to the bin containing most points is given by the color code.

normalized to the bin with most points is given by the coloring. The general shape impressively reflects the constraints imposed by the electroweak precision tests which caused the lower left quadrant of Fig. 5.3(a) to be cut out: in order to fulfill them at least one of the other heavy scalars must have a similar mass as the charged Higgs. The outliers are few parameter points, where cancelations allow to fulfill the constraints. The majority of the points is located in the center, implying that all heavy scalars are close in mass. In view of the bound on the charged Higgs Eq. (5.45) we conclude that also the other two heavy scalars preferably have high masses around the charged Higgs mass. This corresponds to the region around the diagonal in Fig. 5.4(a). The corresponding plot with only those parameter points which additionally lead to a strong PT is shown in Fig. 5.5(b). While the general shape remains unchanged, the focus has changed and hence reveals a preferred hierarchy among the heavy scalars: when A and $H^\pm$ have similar masses the heavy CP-even scalar H is preferred to be about 170 GeV lighter than the others. Nevertheless, other hierarchies are possible, though less frequent. Consequently there is no smoking gun signature for scenarios exhibiting a strong PT as claimed in [180].

In order to investigate signal strengths which can be measured at the LHC and which can deviate from SM predictions in the 2HDM, we investigate the ratio μ_V/μ_F and the signal strength modifiers $\mu_{\gamma\gamma}$, $\mu_{\tau\tau}$ and μ_{VV}. The cross section for producing the SM-like Higgs h_{125} via massive vector boson fusion and associated production with a massive vector boson normalized to the SM prediction is denoted by μ_V, μ_F represents the fermion initiated cross

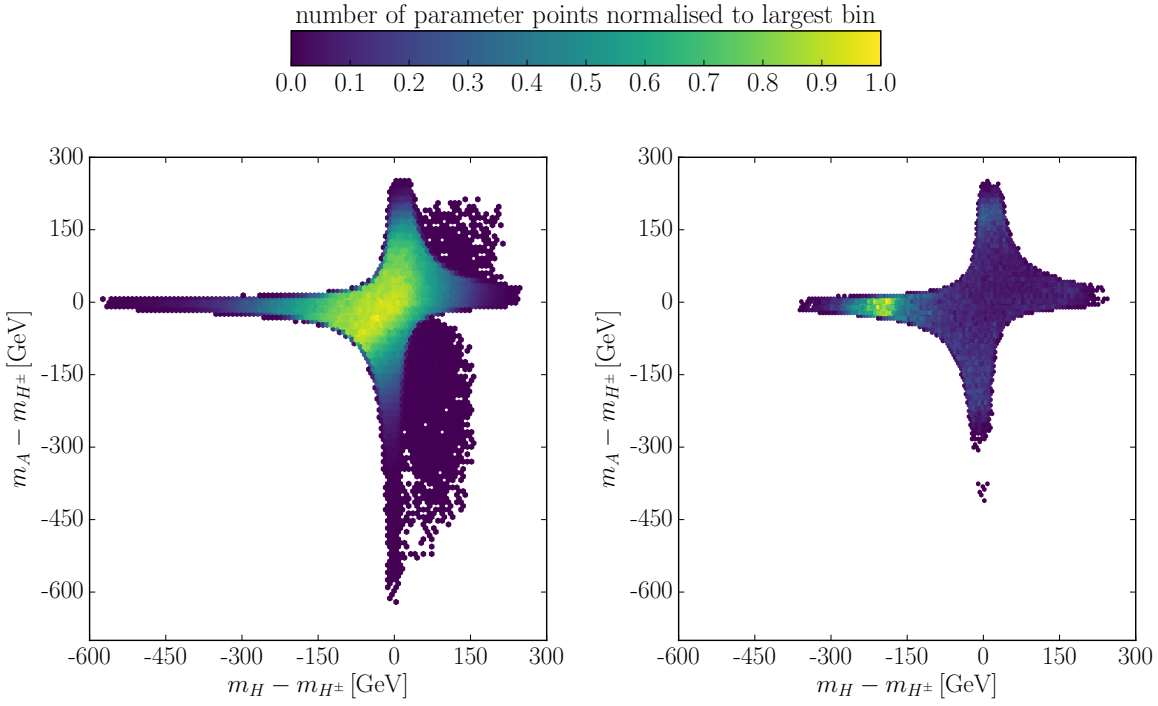

(a) All scenarios found in the scan.

(b) Scenarios additionally fulfilling $\xi_c > 1$ using the AE method.

Figure 5.5: Scenarios of the Type II scan with $h \equiv h_{125}$ in the plane of the differences $m_H - m_{H^\pm}$ and $m_A - m_{H^\pm}$. The relative frequency of the parameter points normalized to the bin containing most points is given by the color code. These plots have been published in [108].

section comprising gluon fusion and associated production with a pair of heavy quarks, also normalized to the SM cross section. Then, μ_{xx} , $x = \gamma, \tau, V$ is defined by

$$\mu_{xx} = \mu_F \frac{\mathrm{BR}_{\mathrm{2HDM}}(h_{125} \longrightarrow xx)}{\mathrm{BR}_{\mathrm{SM}}(H_{\mathrm{SM}} \longrightarrow xx)} , \tag{5.55}$$

where $\mathrm{BR}_{\mathrm{2HDM(SM)}}$ is the branching ratio of the SM-like Higgs boson h_{125} (SM Higgs boson H_{SM}) into the final state xx.
In Fig. 5.6(a) we show the ratio μ_V/μ_F over $\mu_{\gamma\gamma}$ and $\mu_{\tau\tau}$ over μ_{VV} in Fig. 5.6(b). A bow tie structure hosting most of the parameter points with a strong first order PT is obvious in both plots. Comparing the grey area to the colored one we furthermore conclude that requiring a strong first order PT constrains a possible enhancement or suppression of both $\mu_{\gamma\gamma}$ and μ_V/μ_F. For instance observing an enhancement of the photon rate of $\mu_{\gamma\gamma} = 1.3$ together with a ratio $\mu_V/\mu_F = 0.75$ is not compatible with $\xi_c > 1$. Similarly also the allowed range for $\mu_{\tau\tau}$ and μ_{VV} is restricted by demanding a strong PT. In both plots there are regions with parameter points which are not part of the bow tie structure. In Fig. 5.6(a) these are the parameter points in the lower left quadrant, in Fig. 5.6(b) they are located in the upper left area. These points are points in the so-called wrong-sign limit which can be explored in future experiments [189, 210–212]. For these parameter points, the sign of the couplings to down-type fermions is opposite to the couplings to massive vector bosons, which is only possible in the Type II model. From the plots we infer that the wrong-sign limit is strongly constrained and disfavored by a strong first order PT.

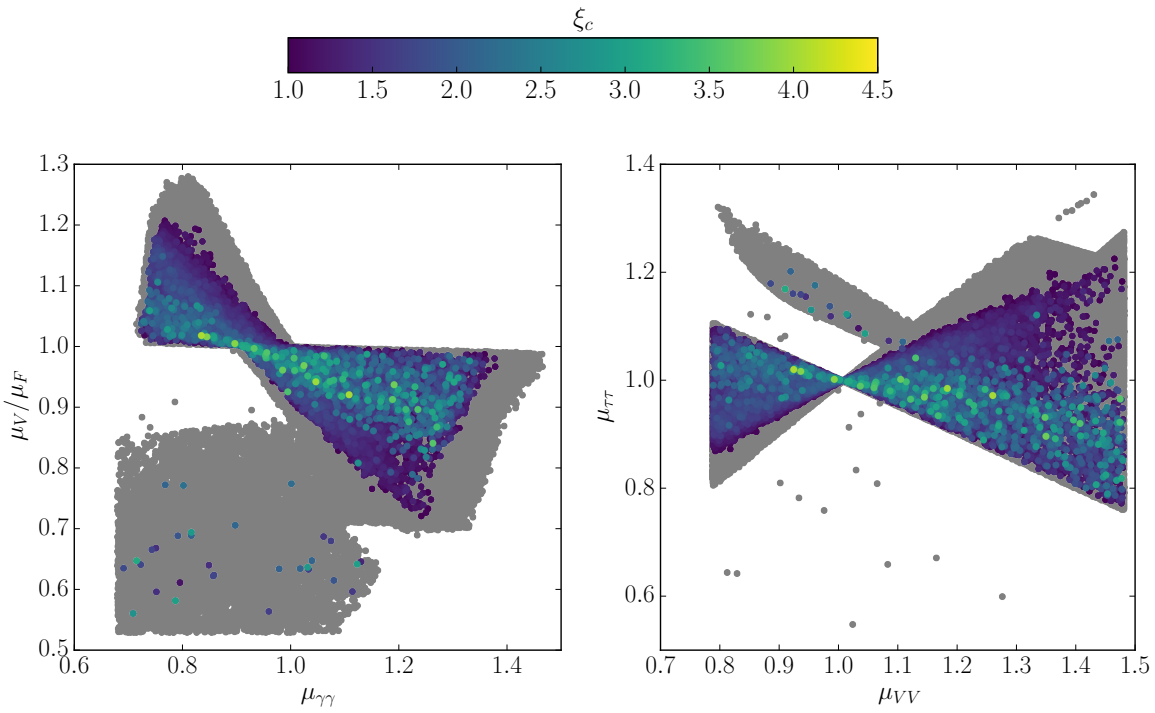

(a) Ratio μ_V/μ_F versus $\mu_{\gamma\gamma}$.

(b) Signal strength modifier $\mu_{\tau\tau}$ versus μ_{VV}.

Figure 5.6: Scenarios of the Type II scan with $h \equiv h_{125}$. In grey all parameter points found in the scan are shown, while for those with $\xi_c > 1$ the strength of the PT obtained with the AE method is given by the color code. These plots have been published in [108].

5.3.2.2. Results for the 2HDM Type I

We now turn to the discussion of results for the scan of Tab. 5.2, where the heavy CP-even scalar H is chosen to be h_{125} in the Type I model. In Fig. 5.7(a) we show all parameter points found in the scan of Tab. 5.2 in the $m_h - m_A$ plane. The line without points at $m_A \approx 125$ GeV is the window left open around the SM-like Higgs $H \equiv h_{125}$. If $m_h < 65$ GeV there are much less points due to the decay $H \longrightarrow hh$ that is kinematically open in this region and experimentally constrained. The upper bound of m_A is due to the relation Eq. (5.54), similarly to the situation explained for Fig. 5.3(a). The majority of the points found in this parameter scan is located around $m_A \approx 200$ GeV. If now in addition a strong PT is required as done in Fig. 5.7(b) many of the previously found parameter points drop out. There are barely any scenarios left with $m_h < 65$ GeV or $m_A < 280$ GeV. Masses of the pseudoscalar Higgs larger than 480 GeV are completely excluded. Hence, imposing a strong first order PT serves as a severe constraint on scenarios with the heavy CP-even Higgs being the observed Higgs h_{125}.
Investigating the actual strength of the PTs in Fig. 5.8 reveals another clear pattern. While all scenarios found in the scan that are compatible with the applied constraints are shown in grey, the colored scenarios lead to a strong first order PT. According to the color code the strongest PTs are reached for high values of m_A. As already explained above, the difference of m_A to the masses of the CP-even Higgs bosons is governed by the couplings λ_i, $i = 1...5$. At the same time these couplings enter the quartic and triple Higgs couplings (*cf.* V_0 in Eq. (5.4)) which are relevant for the strength of the phase transition. Hence higher m_A are

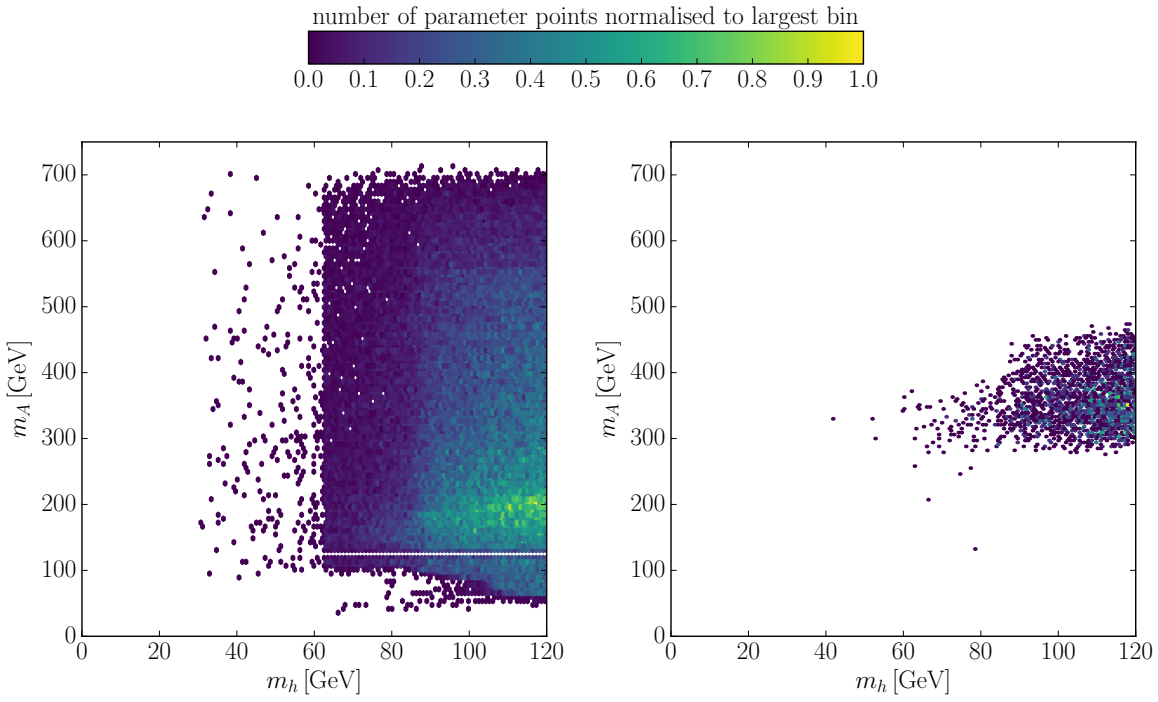

(a) All parameter points.

(b) Parameter points with $\xi_c > 1$ using the AE method.

Figure 5.7: Frequency of parameter points found in the Type I scan of Tab. 5.2, normalized to the number of scenarios in the largest bin in the $m_h - m_A$ plane.

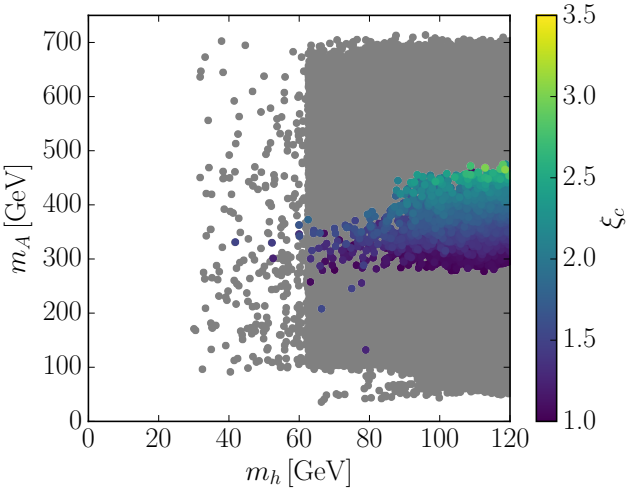

Figure 5.8: Scenarios found in the Type I scan of Tab. 5.2 shown in the $m_h - m_A$ plane. Scenarios in grey fulfill all experimental and theoretical constraints, colored ones additionally have a strong PT derived with the AE method with a strength ξ_c given by the color code. This plot is published in [108].

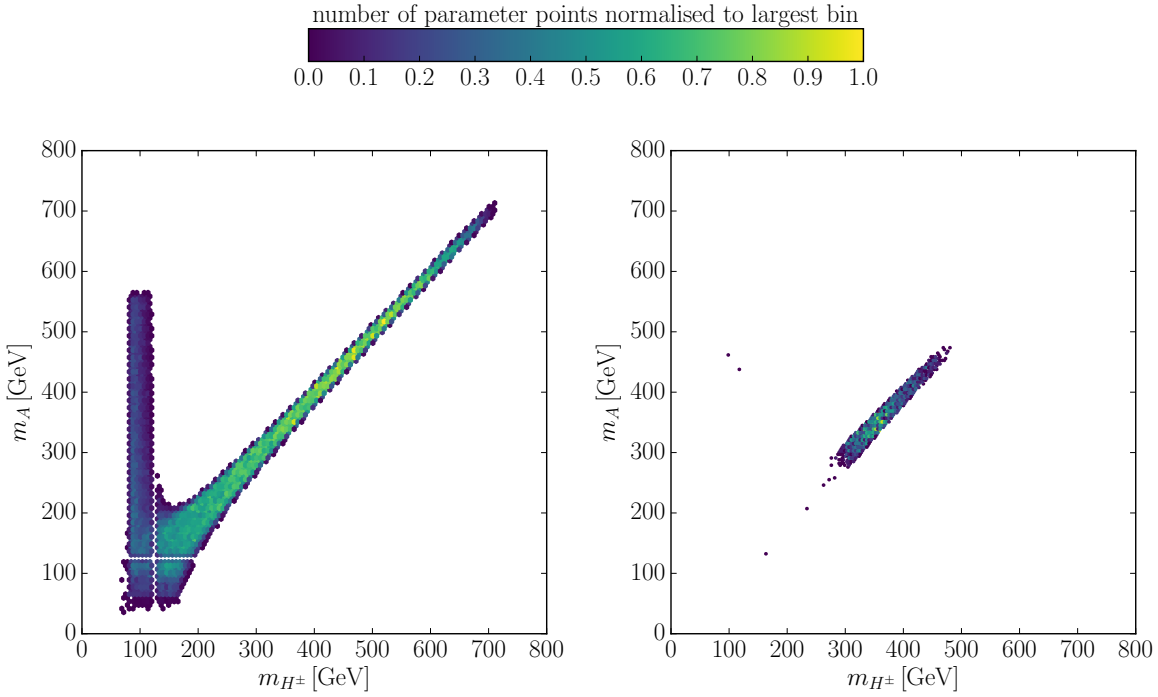

(a) All parameter points found in the scan.

(b) Parameter points with a strong PT obtained with the AE method.

Figure 5.9: Heat map of all valid points found in the Type I scan Tab. 5.2 in the $m_{H^\pm} - m_A$ plane. The color code indicates the frequency of scenarios in the bin, normalized to the largest bin. This figure has been published in [108].

accompanied by stronger PTs up to about 480 GeV, where the interplay of the Higgs masses and the couplings λ_i prevents a strong PT. For low values of $m_h < 80$ GeV requiring a strong PT further constrains the valid parameter space.

The distribution of the scenarios in the $m_{H^\pm} - m_A$ plane is depicted in Fig. 5.9(a) as a heat map. The empty cross where either of the two masses is 125 GeV stems from the span left out around h_{125}. The two branches are subject to the electroweak precision constraints: on the vertical branch the charged Higgs $H^\pm$ is in vicinity of the CP-even Higgs bosons, whereas on the diagonal branch m_A and $m_{H^\pm}$ are of similar size and large. Also the region where all Higgs bosons are lighter than 200 GeV is populated. The maximally allowed masses for the pseudoscalar and the charged Higgs bosons are about 720 GeV. In Fig. 5.9(b) only the points with $\xi_c > 1$ are shown. Here the allowed domain for the two masses is even more restricted: a strong first order PT strongly favors the charged and pseudoscalar Higgs bosons to have masses from 300 to 500 GeV. Enforcing a strong PT the complete spectrum of the Higgs bosons is lighter than ~ 500 GeV.

Similarly to Fig. 5.6 in the Type II model, we now turn to the signal strengths in the Type I model with $H \equiv h_{125}$. Figure 5.10(a) shows the ratio μ_V/μ_F plotted against $\mu_{\gamma\gamma}$. While the grey points that represent all scenarios found in the scan still allow for enhancements of $\mu_{\gamma\gamma}$ up to about 1.5, there is no scenario left above $\mu_{\gamma\gamma} = 0.9$, with one exception, when a strong first order PT is demanded (colored points). Also the central region in μ_V/μ_F for $\mu_{\gamma\gamma} < 0.9$ is strongly constrained by the demand for a strong PT. The plot in Fig. 5.10(b) shows all scenarios in the $\mu_{\tau\tau} - \mu_{VV}$ plane in grey and as before the colored ones additionally lead to a

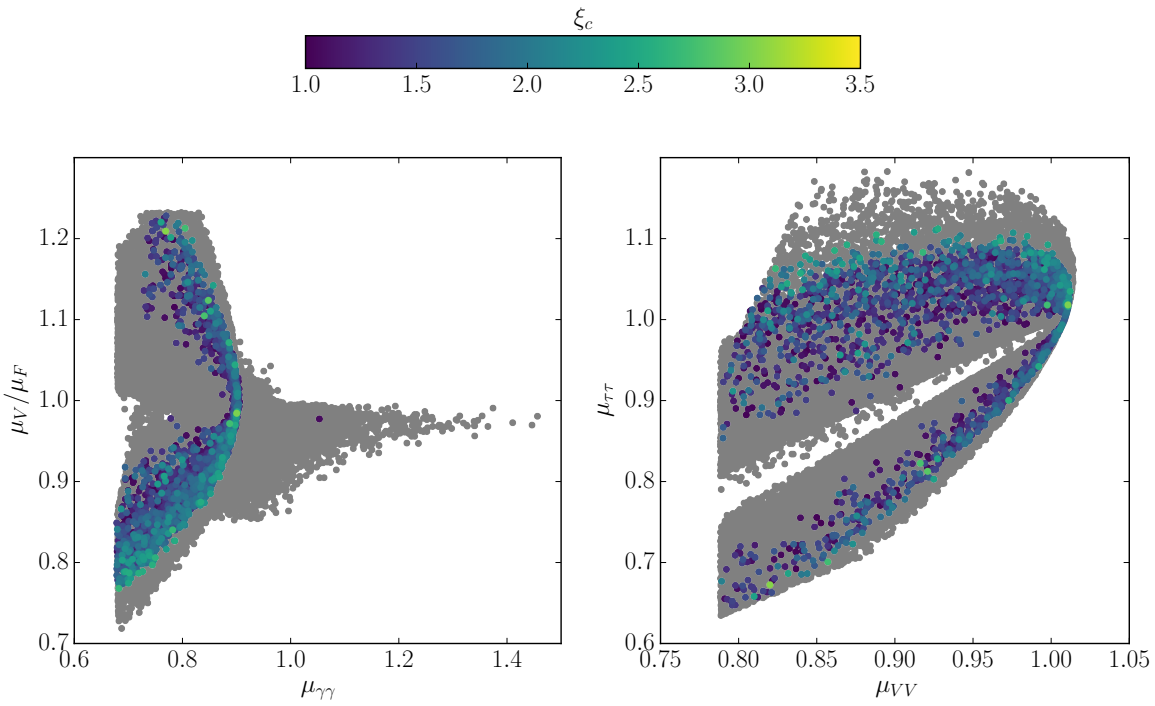

(a) Ratio μ_V/μ_F versus $\mu_{\gamma\gamma}$.

(b) Signal strength modifier $\mu_{\tau\tau}$ versus μ_{VV}.

Figure 5.10: Scenarios of the Type I scan with $H \equiv h_{125}$. All parameter points found in the scan are shown in grey, while for those with $\xi_c > 1$ the strength of the PT using the AE method is given by the color code. These plots have been published in [108].

strong PT. There are no strong PTs with values of $\mu_{\tau\tau} \gtrsim 1.1$. The gap at $\mu_{\tau\tau} = \mu_{VV}$ results from the structure of the couplings in trigonometric functions together with experimental constraints.

5.4. Conclusion

In this work the electroweak phase transition has been studied in the 2HDM Type I and Type II. In order to determine the critical temperature the effective potential has been calculated at the one-loop level at finite temperature including ring-resummation for the masses of bosons and a renormalization prescription which allows for an efficient scan over the parameter space of the model. The renormalization conditions applied for the first time also cover the Higgs mixing angles that enter collider observables through the Higgs couplings. Moreover, the infrared divergence occurring for the Goldstone bosons in the second derivative of the Coleman-Weinberg potential in Landau gauge has been treated by an approach applied to the 2HDM in this context for the first time. The applicability of this approach has been verified explicitly.

Results have been derived for two different implementations of the ring-resummed thermal masses and the results of the AE method have been found to be more reliable than the ones for the PA method. In general, the results show that if in addition to theoretical and experimental constraints a strong first order PT is required, the complete spectrum of the Higgs bosons has to be below 1 TeV in the case of the AE method. The results derived for the Type II model with $h \equiv h_{125}$ show that a strong first order PT favors low masses for the

heavy CP-even Higgs boson H. Moreover, a pseudoscalar Higgs with a mass between 130 and 340 GeV is excluded. It is not possible to identify a unique hierarchy among the heavy scalars, although there is a preference for $m_A \approx m_{H^\pm}$ and $m_A - m_H \approx 170$ GeV. The wrong sign limit is strongly constrained by demanding a strong first order PT. In the analysis for the Type I scan with $H \equiv h_{125}$, insisting on a strong first order PT reveals a typical spectrum of the Higgs masses: while the light CP-even Higgs boson preferably has a mass between 65 and 120 GeV, the charged Higgs and the pseudoscalar Higgs have similar masses between 300 and 500 GeV. The observation of a Higgs boson with a mass larger than 500 GeV is incompatible with a strong PT and possible modifications of signal strengths are restricted. In conclusion we showed that the CP-conserving 2HDM leads to viable scenarios compatible with theoretical and experimental constraints featuring a strong first order phase transition which is a key ingredient for successful baryogenesis. The link between a strong phase transition and collider observables established in this work may serve as guideline for experimental searches, but also as a further constraint on the models. This demonstrates that extending the Higgs sector of the SM is a sensible strategy to help investigating the origin of the observed baryon-antibaryon asymmetry.

6. Conclusion

In this thesis models of New Physics were investigated and predictions for collider observables were improved.
In the first part of the thesis the decay of the lightest up-type squark in the MSSM with general flavor mixings was investigated at the threshold where the W boson in the four-body decay defined in Eq. (3.2) can become on-shell. The finite width of the W boson was taken into account by means of a simple and gauge invariant method valid for the scenarios considered in this work. An extensive scan over relevant parameters of the MSSM was performed, respecting experimental constraints which were available when the work was done. The results showed that the impact of the finite width on the branching ratios of the four-body decay and the two-body decay defined by Eq. (3.1) is substantial. The branching ratios of both decay modes deviate significantly from one, which has important consequences for exclusion bounds in this region. Although the current exclusion bounds are stronger than the ones applied in the analysis here, the findings will still hold as the relevant quantity for the results is the mass difference of the lightest up-type squark and the lightest neutralino and not the absolute values of the masses.
In the second project squark gluino production was studied in the MSSM including the decays of the gluino and the squark. In order to derive precise predictions for the cross section, NLO corrections to all subprocesses are important as well as spin correlations between the production and the decay of the gluino. As a first step the NLO corrections to the production process were considered with a special focus on the real corrections, where on-shell singularities have to be subtracted properly. The basis for a gauge invariant subtraction of these singularities within the framework of the POWHEG − BOX was set up by a calculation by hand of the amplitudes squared for the real corrections to squark gluino production including the spin dependence for the gluino. In addition to all ingredients at LO the NLO corrections to the production process were implemented in the POWHEG − BOX together with the framework for incorporating spin correlations at NLO. As a proof of principles, results were shown for the LO calculation for two example scenarios. The effect of the spin correlations on the kinematic distributions was shown to be up to 20%. The foundation for the gauge invariant calculation of squark gluino production including spin correlations and decays at NLO laid in this work can be taken up in future works aiming at the implementation of the OS subtraction and the decays.
Finally, the electroweak phase transition has been explored within the 2HDM. The strength

of the phase transition has been determined by minimizing the effective potential at finite temperature at the one-loop level, including temperature corrected masses. A renormalization prescription has been developed which keeps the masses and mixing angles of the Higgs bosons at their tree-level values at one-loop and ensures that the vacuum expectation values at tree-level are still a minimum of the potential at the one-loop level. This allows for an efficient scan over the parameter space of the 2HDM. Furthermore, a novel treatment to overcome the Goldstone problem in the second derivative of the Coleman-Weinberg potential was employed. Results were derived for parameter points found in a scan over the parameter space of the 2HDM taking into account recent theoretical and experimental constraints. The results showed that in large parts of the parameter space a strong first order electroweak phase transition is possible, which is a key ingredient for electroweak baryogenesis. Moreover, demanding a first order phase transition in the 2HDM was shown to have important consequences on the allowed Higgs spectrum and possible signal rates at colliders. The renormalization scheme developed here could also be extended in order to investigate the EWPT in other BSM Higgs sectors.

The computations shown in this work improve our understanding of current exclusion bounds set by experiments at the LHC and provide precise predictions of collider observables for the specific models investigated in this thesis. The study in the last part of this work revealed an interesting interplay of Higgs masses and signal strengths and the EWPT in the 2HDM. The findings can help to interpret current and future results of searches for New Physics at the LHC.

7. Appendix

A. Doxygen Documentation and Input Variables

Instructed by keywords written in comments in the source code, the public tool Doxygen [159] automatically generates a documentation of the program. It can cope with various programming languages and provides several output formats. In particular, a website can be constructed, offering the possibility to guide through features relevant for users, but also for programmers. All subroutines and functions are documented with their input parameters and links are provided to the definition in the source code and also to other routines calling, or being called by the subroutine. Although in the documentation all information is provided, here the additional input parameters required for a run of the program are explained shortly. The general inputs of the POWHEG − BOX which have to be provided in the file powheg.input are explained in its user manual. For the implementation of the squark gluino production, the entries described in Tab. A.1 are appended to the input file.
The Doxygen documentation can be generated by the command

```
doxygen doxyfile ,
```

where doxyfile is a file configuring all in- and outputs. In addition to the documentation generated from the keywords in the source code the content of the documentation and website is provided in the file manual.dox.

Keyword	Description and Value
SLHA	Name of the SUSY spectrum file in the SLHA format.
part1	Squark produced in the squark-gluino production process. Possible values are qL, qR, qLbar, qRbar with q = u, d, c, s for left-handed, right-handed, left-handed anti- and right-handed antisquarks, respectively.
part2	Indicates the gluino and has to be set to go.
part3	Squark produced in the decay of the gluino, takes same values as part1.
hels1	Helicity code of part1, value is 0 in this case as it is always a scalar particle.
hels2	Helicity code of part2, value is determined according to the binary codes used by FormCalc.
scaleflag	Value 1 means that the scales are chosen by the inputs facscale and renscale, value 2 means that renormalization and factorization scale are set to the arithmetic mean of the masses of part1 and part2.
facscale	Value is the factorization scale if scaleflag = 1
renscale	Value is the renormalization scale if scaleflag = 1
facscfact	Factor multiplying the factorization scale, determined according to scaleflag.
renscfact	Factor multiplying the renormalization scale, determined according to scaleflag.
decays	0: No decays. 1: Include only the decay of the squark directly produced. 2: Include only the decay of the gluino. 3: Include the decay of the gluino and the squark directly produced. 4: Include the decay of the gluino and the squark produced in the gluino-decay. 5: Include all decays.
nlo_prod	Include NLO contributions for the production, 1 = yes
nlo_sq1dec	Include NLO contributions for the decay of part1, 1 = yes
nlo_sq2dec	Include NLO contributions for the decay of part3, 1 = yes
nlo_gldec	Include NLO contributions for the gluino decay, 1 =yes
gammasq	Value for Γ_{reg} for the OS subtraction for part1
gammagl	Value for Γ_{reg} for the OS subtraction for the gluino
gammaql	Value for Γ_{reg} for the OS subtraction for an internal left-handed squark
gammaqr	Value for Γ_{reg} for the OS subtraction for an internal right-handed squark
OSmethod	Value defines the method for the OS subtraction. 0 = no subtraction, 1 = DRI, 2 = DRII, 3 = DS

Table A.1: Process specific input variables required for the implementation of squark-gluino production in the POWHEG − BOX. The decays entry and the ones following behind are still in the development phase in case of the NLO calculation.

Bibliography

[1] **ATLAS** Collaboration, G. Aad *et al.*, "Observation of a new particle in the search for the Standard Model Higgs boson with the ATLAS detector at the LHC," *Phys.Lett.* **B716** (2012) 1–29, arXiv:1207.7214 [hep-ex].

[2] **CMS** Collaboration, S. Chatrchyan *et al.*, "Observation of a new boson at a mass of 125 GeV with the CMS experiment at the LHC," *Phys.Lett.* **B716** (2012) 30–61, arXiv:1207.7235 [hep-ex].

[3] **Planck** Collaboration, P. A. R. Ade *et al.*, "Planck 2013 results. XVI. Cosmological parameters," *Astron. Astrophys.* **571** (2014) A16, arXiv:1303.5076 [astro-ph.CO].

[4] **WMAP** Collaboration, C. Bennett *et al.*, "Nine-Year Wilkinson Microwave Anisotropy Probe (WMAP) Observations: Final Maps and Results," *The Astrophysical Journal Supplement Series* **208** no. 2, (2013) 20, arXiv:1212.5225 [astro-ph.CO].

[5] J. Wess and B. Zumino, "Supergauge transformations in four dimensions," *Nuclear Physics B* **70** no. 1, (1974) 39 – 50.

[6] D. Volkov and V. Akulov, "Is the neutrino a goldstone particle? ," *Physics Letters B* **46** no. 1, (1973) 109 – 110.

[7] P. Fayet, "Supergauge invariant extension of the Higgs mechanism and a model for the electron and its neutrino," *Nuclear Physics B* **90** no. 0, (1975) 104 – 124.

[8] P. Fayet, "Supersymmetry and weak, electromagnetic and strong interactions," *Physics Letters B* **64** no. 2, (1976) 159 – 162.

[9] P. Fayet, "Spontaneously broken supersymmetric theories of weak, electromagnetic and strong interactions," *Physics Letters B* **69** no. 4, (1977) 489 – 494.

[10] H. Nilles, "Supersymmetry, supergravity and particle physics," *Physics Reports* **110** no. 1–2, (1984) 1 – 162.

[11] H. Haber and G. Kane, "The search for supersymmetry: Probing physics beyond the standard model," *Physics Reports* **117** no. 2–4, (1985) 75 – 263.

[12] T. D. Lee, "A Theory of Spontaneous T Violation," *Phys. Rev.* **D8** (1973) 1226–1239.

[13] J. F. Gunion, H. E. Haber, G. L. Kane, and S. Dawson, "The Higgs Hunter's Guide," *Front. Phys.* **80** (2000) 1–404.

[14] G. C. Branco, P. M. Ferreira, L. Lavoura, M. N. Rebelo, M. Sher, and J. P. Silva, "Theory and phenomenology of two-Higgs-doublet models," *Phys. Rept.* **516** (2012) 1–102, arXiv:1106.0034 [hep-ph].

[15] K.-i. Hikasa and M. Kobayashi, "Light scalar top quark at e^+e^- colliders," *Phys. Rev. D* **36** (Aug, 1987) 724–732.

[16] M. Muhlleitner and E. Popenda, "Light Stop Decay in the MSSM with Minimal Flavour Violation," *JHEP* **1104** (2011) 095, arXiv:1102.5712 [hep-ph].

[17] R. Grober, M. M. Muhlleitner, E. Popenda, and A. Wlotzka, "Light Stop Decays: Implications for LHC Searches," *Eur. Phys. J.* **C75** (2015) 420, arXiv:1408.4662 [hep-ph].

[18] W. Porod and T. Wohrmann, "Higher order top squark decays," *Phys.Rev.* **D55** (1997) 2907–2917, arXiv:hep-ph/9608472 [hep-ph].

[19] C. Boehm, A. Djouadi, and Y. Mambrini, "Decays of the lightest top squark," *Phys.Rev.* **D61** (2000) 095006, arXiv:hep-ph/9907428 [hep-ph].

[20] A. Djouadi and Y. Mambrini, "Three body decays of top and bottom squarks," *Phys. Rev.* **D63** (2001) 115005, arXiv:hep-ph/0011364 [hep-ph].

[21] R. Grober, M. Muhlleitner, E. Popenda, and A. Wlotzka, "Light stop decays into $Wb\tilde{\chi}_1^0$ near the kinematic threshold," *Phys. Lett.* **B747** (2015) 144–151, arXiv:1502.05935 [hep-ph].

[22] P. Harrison and C. L. Smith, "Hadroproduction of supersymmetric particles," *Nuclear Physics B* **213** no. 2, (1983) 223 – 240.

[23] S. Dawson, E. Eichten, and C. Quigg, "Search for supersymmetric particles in hadron-hadron collisions," *Phys. Rev. D* **31** (Apr, 1985) 1581–1637.

[24] W. Beenakker, R. Hopker, and M. Spira, "PROSPINO: A Program for the production of supersymmetric particles in next-to-leading order QCD," arXiv:hep-ph/9611232 [hep-ph].

[25] W. Beenakker, R. Hopker, M. Spira, and P. Zerwas, "Squark and gluino production at hadron colliders," *Nucl.Phys.* **B492** (1997) 51–103, arXiv:hep-ph/9610490 [hep-ph].

[26] W. Hollik, E. Mirabella, and M. K. Trenkel, "Electroweak contributions to squark-gluino production at the LHC," *JHEP* **02** (2009) 002, arXiv:0810.1044 [hep-ph].

[27] W. Beenakker, S. Brensing, M. Kramer, A. Kulesza, E. Laenen, and I. Niessen, "Soft-gluon resummation for squark and gluino hadroproduction," *JHEP* **12** (2009) 041, arXiv:0909.4418 [hep-ph].

[28] W. Beenakker, S. Brensing, M. n. Kramer, A. Kulesza, E. Laenen, L. Motyka, and I. Niessen, "Squark and Gluino Hadroproduction," *Int. J. Mod. Phys.* **A26** (2011) 2637–2664, arXiv:1105.1110 [hep-ph].

[29] M. R. Kauth, A. Kress, and J. H. Kuhn, "Gluino-Squark Production at the LHC: The Threshold," *JHEP* **12** (2011) 104, arXiv:1108.0542 [hep-ph].

[30] P. Falgari, C. Schwinn, and C. Wever, "NLL soft and Coulomb resummation for squark and gluino production at the LHC," *JHEP* **06** (2012) 052, arXiv:1202.2260 [hep-ph].

[31] D. Gonçalves-Netto, D. López-Val, K. Mawatari, T. Plehn, and I. Wigmore, "Automated Squark and Gluino Production to Next-to-Leading Order," *Phys.Rev.* **D87** no. 1, (2013) 014002, arXiv:1211.0286 [hep-ph].

[32] P. Falgari, C. Schwinn, and C. Wever, "Finite-width effects on threshold corrections to squark and gluino production," *JHEP* **01** (2013) 085, arXiv:1211.3408 [hep-ph].

[33] W. Beenakker, T. Janssen, S. Lepoeter, M. Kramer, A. Kulesza, E. Laenen, I. Niessen, S. Thewes, and T. Van Daal, "Towards NNLL resummation: hard matching coefficients for squark and gluino hadroproduction," *JHEP* **10** (2013) 120, arXiv:1304.6354 [hep-ph].

[34] R. Gavin, C. Hangst, M. Kramer, M. Muhlleitner, M. Pellen, E. Popenda, and M. Spira, "Matching Squark Pair Production at NLO with Parton Showers," *JHEP* **10** (2013) 187, arXiv:1305.4061 [hep-ph].

[35] R. Gavin, C. Hangst, M. Kramer, M. Muhlleitner, M. Pellen, E. Popenda, and M. Spira, "Squark Production and Decay matched with Parton Showers at NLO," *Eur. Phys. J.* **C75** no. 1, (2015) 29, arXiv:1407.7971 [hep-ph].

[36] P. Nason, "A New method for combining NLO QCD with shower Monte Carlo algorithms," *JHEP* **0411** (2004) 040, arXiv:hep-ph/0409146 [hep-ph].

[37] S. Frixione, P. Nason, and C. Oleari, "Matching NLO QCD computations with Parton Shower simulations: the POWHEG method," *JHEP* **0711** (2007) 070, arXiv:0709.2092 [hep-ph].

[38] S. Alioli, P. Nason, C. Oleari, and E. Re, "A general framework for implementing NLO calculations in shower Monte Carlo programs: the POWHEG BOX," *JHEP* **1006** (2010) 043, arXiv:1002.2581 [hep-ph].

[39] V. Kuzmin, V. Rubakov, and M. Shaposhnikov, "On anomalous electroweak baryon-number non-conservation in the early universe," *Physics Letters B* **155** no. 1, (1985) 36 – 42.

[40] M. E. Shaposhnikov, "Possible Appearance of the Baryon Asymmetry of the Universe in an Electroweak Theory," *JETP Lett.* **44** (1986) 465–468. [Pisma Zh. Eksp. Teor. Fiz.44,364(1986)].

[41] M. E. Shaposhnikov, "Baryon Asymmetry of the Universe in Standard Electroweak Theory," *Nucl. Phys.* **B287** (1987) 757–775.

[42] A. D. Sakharov, "Violation of CP Invariance, c Asymmetry, and Baryon Asymmetry of the Universe," *Pisma Zh. Eksp. Teor. Fiz.* **5** (1967) 32–35. [Usp. Fiz. Nauk161,61(1991)].

[43] F. R. Klinkhamer and N. S. Manton, "A Saddle Point Solution in the Weinberg-Salam Theory," *Phys. Rev.* **D30** (1984) 2212.

[44] A. I. Bochkarev and M. E. Shaposhnikov, "Electroweak Production of Baryon Asymmetry and Upper Bounds on the Higgs and Top Masses," *Mod. Phys. Lett.* **A2** (1987) 417.

[45] K. Kajantie, M. Laine, K. Rummukainen, and M. E. Shaposhnikov, "The Electroweak phase transition: A Nonperturbative analysis," *Nucl. Phys.* **B466** (1996) 189–258, arXiv:hep-lat/9510020 [hep-lat].

[46] K. Jansen, "Status of the finite temperature electroweak phase transition on the lattice," *Nucl. Phys. Proc. Suppl.* **47** (1996) 196–211, arXiv:hep-lat/9509018 [hep-lat].

[47] **ATLAS, CMS** Collaboration, G. Aad *et al.*, "Combined Measurement of the Higgs Boson Mass in pp Collisions at $\sqrt{s} = 7$ and 8 TeV with the ATLAS and CMS Experiments," *Phys. Rev. Lett.* **114** (2015) 191803, arXiv:1503.07589 [hep-ex].

[48] N. Cabibbo, "Unitary Symmetry and Leptonic Decays," *Phys. Rev. Lett.* **10** (Jun, 1963) 531–533.

[49] M. Kobayashi and T. Maskawa, "CP-Violation in the Renormalizable Theory of Weak Interaction," *Progress of Theoretical Physics* **49** no. 2, (1973) 652–657.

[50] P. Huet and E. Sather, "Electroweak baryogenesis and standard model CP violation," *Phys. Rev.* **D51** (1995) 379–394, arXiv:hep-ph/9404302 [hep-ph].

[51] M. B. Gavela, P. Hernandez, J. Orloff, and O. Pene, "Standard model CP violation and baryon asymmetry," *Mod. Phys. Lett.* **A9** (1994) 795–810, arXiv:hep-ph/9312215 [hep-ph].

[52] M. B. Gavela, P. Hernandez, J. Orloff, O. Pene, and C. Quimbay, "Standard model CP violation and baryon asymmetry. Part 2: Finite temperature," *Nucl. Phys.* **B430** (1994) 382–426, arXiv:hep-ph/9406289 [hep-ph].

[53] M. Carena, G. Nardini, M. Quiros, and C. E. M. Wagner, "The Baryogenesis Window in the MSSM," *Nucl. Phys.* **B812** (2009) 243–263, arXiv:0809.3760 [hep-ph].

[54] **ATLAS** Collaboration, G. Aad *et al.*, "ATLAS Run 1 searches for direct pair production of third-generation squarks at the Large Hadron Collider," *Eur. Phys. J.* **C75** no. 10, (2015) 510, arXiv:1506.08616 [hep-ex]. [Erratum: Eur. Phys. J.C76,no.3,153(2016)].

[55] M. Drees, R. Godbole, and P. Roy, *Theory and phenomenology of sparticles : an account of four-dimensional N = 1 supersymmetry in high energy physics.* World Scientific, Singapore, 2005.

[56] H. Baer and X. Tata, *Weak Scale Supersymmetry.* Cambridge University Press, Cambridge, 2006.

[57] S. Coleman and J. Mandula, "All possible symmetries of the s matrix," *Phys. Rev.* **159** (Jul, 1967) 1251–1256.

[58] R. Haag, J. T. Łopuszański, and M. Sohnius, "All possible generators of supersymmetries of the s-matrix," *Nuclear Physics B* **88** no. 2, (1975) 257 – 274.

[59] H. K. Dreiner, H. E. Haber, and S. P. Martin, "Two-component spinor techniques and Feynman rules for quantum field theory and supersymmetry," *Phys. Rept.* **494** (2010) 1–196, arXiv:0812.1594 [hep-ph].

[60] P. Z. Skands, B. Allanach, H. Baer, C. Balazs, G. Belanger, *et al.*, "SUSY Les Houches accord: Interfacing SUSY spectrum calculators, decay packages, and event generators," *JHEP* **0407** (2004) 036, arXiv:hep-ph/0311123 [hep-ph].

[61] D. Z. Freedman, P. van Nieuwenhuizen, and S. Ferrara, "Progress Toward a Theory of Supergravity," *Phys. Rev.* **D13** (1976) 3214–3218.

[62] D. Z. Freedman and P. van Nieuwenhuizen, "Properties of supergravity theory," *Phys. Rev. D* **14** (Aug, 1976) 912–916.

[63] S. Deser and B. Zumino, "Consistent supergravity," *Physics Letters B* **62** no. 3, (1976) 335 – 337.

[64] P. van Nieuwenhuizen, "Supergravity," *Physics Reports* **68** no. 4, (1981) 189 – 398.

[65] A. H. Chamseddine, R. Arnowitt, and P. Nath, "Locally supersymmetric grand unification," *Phys. Rev. Lett.* **49** (Oct, 1982) 970–974.

[66] H. P. Nilles, "Dynamically broken supergravity and the hierarchy problem," *Physics Letters B* **115** no. 3, (1982) 193 – 196.

[67] H. Nilles, "Supergravity generates hierarchies," *Nuclear Physics B* **217** no. 2, (1983) 366 – 380.

[68] B. Allanach, C. Balazs, G. Belanger, M. Bernhardt, F. Boudjema, *et al.*, "SUSY Les Houches Accord 2," *Comput.Phys.Commun.* **180** (2009) 8–25, arXiv:0801.0045 [hep-ph].

[69] "ATLAS Supersymmetry (SUSY) searches." https://twiki.cern.ch/twiki/bin/view/AtlasPublic/SupersymmetryPublicResults. Accessed: 2017-04-05.

[70] "CMS Supersymmetry Physics Results." https://twiki.cern.ch/twiki/bin/view/CMSPublic/PhysicsResultsSUS. Accessed: 2017-04-05.

[71] **CMS** Collaboration, A. M. Sirunyan *et al.*, "Searches for pair production for third-generation squarks in sqrt(s)=13 TeV pp collisions," arXiv:1612.03877 [hep-ex].

[72] **CMS Collaboration** Collaboration, "Search for top squarks decaying to a charm quark and a neutralino in events with a jet and missing transverse momentum," Tech. Rep. CMS-PAS-SUS-13-009, CERN, Geneva, 2014.

[73] **CMS** Collaboration, S. Chatrchyan *et al.*, "Search for top-squark pair production in the single-lepton final state in pp collisions at $\sqrt{s} = 8$ TeV," *Eur. Phys. J.* **C73** no. 12, (2013) 2677, arXiv:1308.1586 [hep-ex].

[74] **ATLAS** Collaboration, T. A. collaboration, "Search for pair-produced top squarks decaying into a charm quark and the lightest neutralinos with 20.3 fb^{-1} of pp collisions at $\sqrt{s} = 8$ TeV with the ATLAS detector at the LHC,".

[75] **ATLAS** Collaboration, G. Aad *et al.*, "Search for pair-produced third-generation squarks decaying via charm quarks or in compressed supersymmetric scenarios in pp collisions at $\sqrt{s} = 8$ TeV with the ATLAS detector," *Phys. Rev.* **D90** no. 5, (2014) 052008, arXiv:1407.0608 [hep-ex].

[76] **ATLAS** Collaboration, G. Aad *et al.*, "Search for top squark pair production in final states with one isolated lepton, jets, and missing transverse momentum in $\sqrt{s}$ =8 TeV pp collisions with the ATLAS detector," *JHEP* **11** (2014) 118, arXiv:1407.0583 [hep-ex].

[77] **ATLAS** Collaboration, G. Aad *et al.*, "Search for direct top-squark pair production in final states with two leptons in pp collisions at $\sqrt{s} = 8$TeV with the ATLAS detector," *JHEP* **06** (2014) 124, arXiv:1403.4853 [hep-ex].

[78] **ATLAS** Collaboration, G. Aad *et al.*, "Summary of the searches for squarks and gluinos using $\sqrt{s} = 8$ TeV pp collisions with the ATLAS experiment at the LHC," *JHEP* **10** (2015) 054, arXiv:1507.05525 [hep-ex].

[79] G. Dissertori, I. Knowles, and M. Schmelling, *Quantum Chromodynamics: High energy experiments and theory.* Oxford University Press, 2003.

[80] **Particle Data Group** Collaboration, C. Patrignani *et al.*, "2016 Review of Particle Physics," *Chin. Phys.* **C40** (2016) 100001.

[81] T. Kinoshita, "Mass singularities of feynman amplitudes," *Journal of Mathematical Physics* **3** no. 4, (1962) 650–677.

[82] T. D. Lee and M. Nauenberg, "Degenerate systems and mass singularities," *Phys. Rev.* **133** (Mar, 1964) B1549–B1562.

[83] E. Fuchs, S. Thewes, and G. Weiglein, "Interference effects in BSM processes with a generalised narrow-width approximation," *Eur. Phys. J.* **C75** (2015) 254, arXiv:1411.4652 [hep-ph].

[84] V. S. Fadin, V. A. Khoze, and A. D. Martin, "Interference radiative phenomena in the production of heavy unstable particles," *Phys. Rev. D* **49** (Mar, 1994) 2247–2256.

[85] V. S. Fadin, V. A. Khoze, and A. D. Martin, "How suppressed are the radiative interference effects in heavy instable particle production?," *Phys. Lett.* **B320** (1994) 141–144, arXiv:hep-ph/9309234 [hep-ph].

[86] V. Khoze, W. Stirling, and L. H. Orr, "Soft gluon radiation in e+e− → tt," *Nuclear Physics B* **378** no. 3, (1992) 413 – 442.

[87] S. Frixione, Z. Kunszt, and A. Signer, "Three jet cross-sections to next-to-leading order," *Nucl.Phys.* **B467** (1996) 399–442, arXiv:hep-ph/9512328 [hep-ph].

[88] S. Frixione, "A General approach to jet cross-sections in QCD," *Nucl.Phys.* **B507** (1997) 295–314, arXiv:hep-ph/9706545 [hep-ph].

[89] S. Frixione and B. R. Webber, "Matching NLO QCD computations and parton shower simulations," *JHEP* **06** (2002) 029, arXiv:hep-ph/0204244 [hep-ph].

[90] J. Alwall *et al.*, "A Standard format for Les Houches event files," *Comput. Phys. Commun.* **176** (2007) 300–304, arXiv:hep-ph/0609017 [hep-ph].

[91] M. Trodden, "Electroweak baryogenesis," *Rev. Mod. Phys.* **71** (1999) 1463–1500, arXiv:hep-ph/9803479 [hep-ph].

[92] D. E. Morrissey and M. J. Ramsey-Musolf, "Electroweak baryogenesis," *New J. Phys.* **14** (2012) 125003, arXiv:1206.2942 [hep-ph].

[93] M. Quiros, "Finite temperature field theory and phase transitions," in *High energy physics and cosmology. Proceedings, Summer School, Trieste, Italy, June 29-July 17, 1998*, pp. 187–259. 1999. arXiv:hep-ph/9901312 [hep-ph].

[94] A. I. Bochkarev, S. V. Kuzmin, and M. E. Shaposhnikov, "Electroweak baryogenesis and the Higgs boson mass problem," *Phys. Lett.* **B244** (1990) 275–278.

[95] A. G. Cohen, D. B. Kaplan, and A. E. Nelson, "Spontaneous baryogenesis at the weak phase transition," *Phys. Lett.* **B263** (1991) 86–92.

[96] A. E. Nelson, D. B. Kaplan, and A. G. Cohen, "Why there is something rather than nothing: Matter from weak interactions," *Nucl. Phys.* **B373** (1992) 453–478.

[97] N. Turok and J. Zadrozny, "Phase transitions in the two-doublet model," *Nuclear Physics B* **369** no. 3, (1992) 729 – 742.

[98] N. Turok and J. Zadrozny, "Electroweak baryogenesis in the two-doublet model," *Nuclear Physics B* **358** no. 2, (1991) 471 – 493.

[99] L. McLerran, M. Shaposhnikov, N. Turok, and M. Voloshin, "Why the baryon asymmetry of the universe is $\propto 10^{-10}$," *Physics Letters B* **256** no. 3, (1991) 477 – 483.

[100] A. T. Davies, C. D. froggatt, G. Jenkins, and R. G. Moorhouse, "Baryogenesis constraints on two Higgs doublet models," *Phys. Lett.* **B336** (1994) 464–470.

[101] K. Funakubo, A. Kakuto, and K. Takenaga, "The Effective potential of electroweak theory with two massless Higgs doublets at finite temperature," *Prog. Theor. Phys.* **91** (1994) 341–352, arXiv:hep-ph/9310267 [hep-ph].

[102] J. M. Cline, K. Kainulainen, and A. P. Vischer, "Dynamics of two Higgs doublet CP violation and baryogenesis at the electroweak phase transition," *Phys. Rev.* **D54** (1996) 2451–2472, arXiv:hep-ph/9506284 [hep-ph].

[103] J. M. Cline and P.-A. Lemieux, "Electroweak phase transition in two Higgs doublet models," *Phys. Rev.* **D55** (1997) 3873–3881, arXiv:hep-ph/9609240 [hep-ph].

[104] J. M. Cline, K. Kainulainen, and A. P. Vischer, "Dynamics of two Higgs doublet CP violation and baryogenesis at the electroweak phase transition," *Phys. Rev.* **D54** (1996) 2451–2472, arXiv:hep-ph/9506284 [hep-ph].

[105] L. Fromme, S. J. Huber, and M. Seniuch, "Baryogenesis in the two-Higgs doublet model," *JHEP* **11** (2006) 038, arXiv:hep-ph/0605242 [hep-ph].

[106] J. M. Cline, K. Kainulainen, and M. Trott, "Electroweak Baryogenesis in Two Higgs Doublet Models and B meson anomalies," *JHEP* **11** (2011) 089, arXiv:1107.3559 [hep-ph].

[107] G. C. Dorsch, S. J. Huber, and J. M. No, "A strong electroweak phase transition in the 2HDM after LHC8," *JHEP* **10** (2013) 029, arXiv:1305.6610 [hep-ph].

[108] P. Basler, M. Krause, M. Muhlleitner, J. Wittbrodt, and A. Wlotzka, "Strong First Order Electroweak Phase Transition in the CP-Conserving 2HDM Revisited," *Journal of High Energy Physics* **2017** no. 2, (2017) 121, arXiv:1612.04086 [hep-ph].

[109] M. E. Carrington, "The Effective potential at finite temperature in the Standard Model," *Phys. Rev.* **D45** (1992) 2933–2944.

[110] R. R. Parwani, "Resummation in a hot scalar field theory," *Phys. Rev.* **D45** (1992) 4695, arXiv:hep-ph/9204216 [hep-ph]. [Erratum: Phys. Rev.D48,5965(1993)].

[111] P. B. Arnold and O. Espinosa, "The Effective potential and first order phase transitions: Beyond leading-order," *Phys. Rev.* **D47** (1993) 3546, arXiv:hep-ph/9212235 [hep-ph]. [Erratum: Phys. Rev.D50,6662(1994)].

[112] R. S. Chivukula, H. Georgi, and L. Randall, "A composite technicolor standard model of quarks," *Nuclear Physics B* **292** no. 0, (1987) 93 – 108.

[113] L. J. Hall and L. Randall, "Weak-scale effective supersymmetry," *Phys. Rev. Lett.* **65** (Dec, 1990) 2939–2942.

[114] A. Buras, P. Gambino, M. Gorbahn, S. Jager, and L. Silvestrini, "Universal unitarity triangle and physics beyond the standard model," *Phys.Lett.* **B500** (2001) 161–167, arXiv:hep-ph/0007085 [hep-ph].

[115] G. D'Ambrosio, G. Giudice, G. Isidori, and A. Strumia, "Minimal flavor violation: An Effective field theory approach," *Nucl.Phys.* **B645** (2002) 155–187, arXiv:hep-ph/0207036 [hep-ph].

[116] A. Wlotzka, "Decays of the Lightest Squark in the MSSM with Flavor Violation," Master's thesis, ITP, KIT, Karlsruhe, Germany, 2014.

[117] R. Grober, *Aspects of Higgs Physics and New Physics at the LHC*. PhD thesis, ITP, KIT, Karlsruhe, Germany, 2014.

[118] W. Porod and T. Wohrmann, "Higher order top squark decays," *Phys.Rev.* **D55** (1997) 2907–2917, arXiv:hep-ph/9608472 [hep-ph].

[119] A. Denner and S. Dittmaier, "The Complex-mass scheme for perturbative calculations with unstable particles," *Nucl.Phys.Proc.Suppl.* **160** (2006) 22–26, arXiv:hep-ph/0605312 [hep-ph].

[120] U. Baur, J. A. M. Vermaseren, and D. Zeppenfeld, "Electroweak vector boson production in high-energy *ep* collisions," *Nucl. Phys.* **B375** (1992) 3–44.

[121] **Particle Data Group** Collaboration, J. Beringer *et al.*, "2012 Review of Particle Physics," *Phys. Rev.* **D86** (2012) 010001.

[122] A. Djouadi, M. Muhlleitner, and M. Spira, "Decays of supersymmetric particles: The Program SUSY-HIT (SUspect-SdecaY-Hdecay-InTerface)," *Acta Phys.Polon.* **B38** (2007) 635–644, arXiv:hep-ph/0609292 [hep-ph].

[123] W. Porod, "SPheno, a program for calculating supersymmetric spectra, SUSY particle decays and SUSY particle production at e+ e- colliders," *Comput.Phys.Commun.* **153** (2003) 275–315, arXiv:hep-ph/0301101 [hep-ph].

[124] W. Porod and F. Staub, "SPheno 3.1: Extensions including flavour, CP-phases and models beyond the MSSM," *Comput.Phys.Commun.* **183** (2012) 2458–2469, arXiv:1104.1573 [hep-ph].

[125] **Particle Data Group** Collaboration, K. A. Olive *et al.*, "Review of Particle Physics," *Chin. Phys.* **C38** (2014) 090001.

[126] P. Bechtle, S. Heinemeyer, O. Stål, T. Stefaniak, and G. Weiglein, "*HiggsSignals*: Confronting arbitrary Higgs sectors with measurements at the Tevatron and the LHC," *Eur. Phys. J.* **C74** no. 2, (2014) 2711, arXiv:1305.1933 [hep-ph].

[127] P. Bechtle, O. Brein, S. Heinemeyer, G. Weiglein, and K. E. Williams, "HiggsBounds: Confronting Arbitrary Higgs Sectors with Exclusion Bounds from LEP and the Tevatron," *Comput.Phys.Commun.* **181** (2010) 138–167, arXiv:0811.4169 [hep-ph].

[128] P. Bechtle, O. Brein, S. Heinemeyer, G. Weiglein, and K. E. Williams, "HiggsBounds 2.0.0: Confronting Neutral and Charged Higgs Sector Predictions with Exclusion Bounds from LEP and the Tevatron," *Comput.Phys.Commun.* **182** (2011) 2605–2631, arXiv:1102.1898 [hep-ph].

[129] P. Bechtle, O. Brein, S. Heinemeyer, O. Stal, T. Stefaniak, *et al.*, "Recent Developments in HiggsBounds and a Preview of HiggsSignals," *PoS* (2012) 024, arXiv:1301.2345 [hep-ph].

[130] P. Bechtle, O. Brein, S. Heinemeyer, O. Stål, T. Stefaniak, G. Weiglein, and K. E. Williams, "HiggsBounds – 4: Improved Tests of Extended Higgs Sectors against Exclusion Bounds from LEP, the Tevatron and the LHC," *Eur. Phys. J.* **C74** no. 3, (2014) 2693, arXiv:1311.0055 [hep-ph].

[131] A. Djouadi, J. Kalinowski, and M. Spira, "HDECAY: a program for Higgs boson decays in the Standard Model and its supersymmetric extension," *Computer Physics Communications* **108** (Jan., 1998) 56–74, arXiv:hep-ph/9704448.

[132] J. M. Butterworth *et al.*, "THE TOOLS AND MONTE CARLO WORKING GROUP Summary Report from the Les Houches 2009 Workshop on TeV Colliders," in *Physics at TeV colliders. Proceedings, 6th Workshop, dedicated to Thomas Binoth, Les Houches, France, June 8-26, 2009.* 2010. arXiv:1003.1643 [hep-ph].

[133] R. Harlander, M. Muhlleitner, J. Rathsman, M. Spira, and O. Stål, "Interim recommendations for the evaluation of Higgs production cross sections and branching ratios at the LHC in the Two-Higgs-Doublet Model," arXiv:1312.5571 [hep-ph].

[134] **LHCb, CMS** Collaboration, V. Khachatryan *et al.*, "Observation of the rare $B_s^0 \to \mu^+\mu^-$ decay from the combined analysis of CMS and LHCb data," *Nature* **522** (2015) 68–72, arXiv:1411.4413 [hep-ex].

[135] **ATLAS, CDF, LHCb, CMS, D0** Collaboration, P. Eerola, CDF, CMS, and D0, "Rare $B_{(s)}^0 \to \mu^+\mu^-$ decays," *AIP Conf. Proc.* **1560** (2013) 394–398, arXiv:1209.3440 [hep-ex].

[136] **Heavy Flavor Averaging Group** Collaboration, Y. Amhis *et al.*, "Averages of B-Hadron, C-Hadron, and tau-lepton properties as of early 2012," arXiv:1207.1158 [hep-ex].

[137] F. Mahmoudi, "SuperIso: A Program for calculating the isospin asymmetry of B to K* γ in the MSSM," *Comput.Phys.Commun.* **178** (2008) 745–754, arXiv:0710.2067 [hep-ph].

[138] F. Mahmoudi, "SuperIso v2.3: A Program for calculating flavor physics observables in Supersymmetry," *Comput.Phys.Commun.* **180** (2009) 1579–1613, arXiv:0808.3144 [hep-ph].

[139] A. Arbey and F. Mahmoudi, "SuperIso Relic: A Program for calculating relic density and flavor physics observables in Supersymmetry," *Comput.Phys.Commun.* **181** (2010) 1277–1292, arXiv:0906.0369 [hep-ph].

[140] A. Arbey and F. Mahmoudi, "SuperIso Relic v3.0: A program for calculating relic density and flavour physics observables: Extension to NMSSM," *Computer Physics Communications* **182** no. 7, (2011) 1582 – 1583.

[141] **ATLAS** Collaboration, G. Aad *et al.*, "Search for squarks and gluinos with the ATLAS detector in final states with jets and missing transverse momentum using $\sqrt{s} = 8$ TeV proton–proton collision data," *JHEP* **09** (2014) 176, arXiv:1405.7875 [hep-ex].

[142] **CMS Collaboration** Collaboration, "Search for supersymmetry in hadronic final states using MT2 with the CMS detector at sqrt(s) = 8 TeV," Tech. Rep. CMS-PAS-SUS-13-019, CERN, Geneva, 2014.

[143] S. Kraml, S. Kulkarni, U. Laa, A. Lessa, W. Magerl, *et al.*, "SModelS: a tool for interpreting simplified-model results from the LHC and its application to supersymmetry," *Eur.Phys.J.* **C74** (2014) 2868, arXiv:1312.4175 [hep-ph].

[144] S. Kraml, S. Kulkarni, U. Laa, A. Lessa, V. Magerl, *et al.*, "SModelS v1.0: a short user guide," arXiv:1412.1745 [hep-ph].

[145] H. E. Haber, "Spin formalism and applications to new physics searches," arXiv:hep-ph/9405376 [hep-ph].

[146] A. Djouadi, W. Hollik, and C. Junger, "QCD corrections to scalar quark decays," *Phys.Rev.* **D55** (1997) 6975–6985, arXiv:hep-ph/9609419 [hep-ph].

[147] T. Hahn, "Generating Feynman diagrams and amplitudes with FeynArts 3," *Comput.Phys.Commun.* **140** (2001) 418–431, arXiv:hep-ph/0012260 [hep-ph].

[148] T. Hahn and M. Perez-Victoria, "Automatized one loop calculations in four-dimensions and D-dimensions," *Comput.Phys.Commun.* **118** (1999) 153–165, arXiv:hep-ph/9807565 [hep-ph].

[149] C. Hangst, *Matching Squark Production and Decay at Next-to-leading Order Accuracy with Parton Showers.* PhD thesis, KIT, 2014.

[150] S. Frixione, E. Laenen, P. Motylinski, B. R. Webber, and C. D. White, "Single-top hadroproduction in association with a W boson," *JHEP* **07** (2008) 029, arXiv:0805.3067 [hep-ph].

[151] E. Re, "Single-top Wt-channel production matched with parton showers using the POWHEG method," *Eur. Phys. J.* **C71** (2011) 1547, arXiv:1009.2450 [hep-ph].

[152] J. Baglio, B. Jager, and M. Kesenheimer, "Electroweakino pair production at the LHC: NLO SUSY-QCD corrections and parton-shower effects," *JHEP* **07** (2016) 083, `arXiv:1605.06509 [hep-ph]`.

[153] S. Catani, S. Dittmaier, M. H. Seymour, and Z. Trocsanyi, "The Dipole formalism for next-to-leading order QCD calculations with massive partons," *Nucl. Phys.* **B627** (2002) 189–265, `arXiv:hep-ph/0201036 [hep-ph]`.

[154] R. Mertig, M. Bohm, and A. Denner, "Feyn calc - computer-algebraic calculation of feynman amplitudes," *Computer Physics Communications* **64** no. 3, (1991) 345 – 359.

[155] A. Denner, H. Eck, O. Hahn, and J. Kublbeck, "Feynman rules for fermion-number-violating interactions," *Nuclear Physics B* **387** no. 2, (1992) 467 – 481.

[156] A. Denner, H. Eck, O. Hahn, and J. Kublbeck, "Compact feynman rules for majorana fermions," *Physics Letters B* **291** no. 3, (1992) 278 – 280.

[157] T.-P. Cheng and L.-F. Li, *Gauge Theory of Elementary Particle Physics*. Oxford University Press, Oxford, 1984.

[158] M. Muhlleitner, A. Djouadi, and Y. Mambrini, "SDECAY: A Fortran code for the decays of the supersymmetric particles in the MSSM," *Comput.Phys.Commun.* **168** (2005) 46–70, `arXiv:hep-ph/0311167 [hep-ph]`.

[159] "Doxygen." `https://sourceforge.net/projects/doxygen/`. Accessed: 2017-04-05.

[160] **ATLAS Collaboration** Collaboration, "Search for supersymmetry with two same-sign leptons or three leptons using 13.2 fb^{-1} of $\sqrt{s} = 13$ TeV pp collision data collected by the ATLAS detector," Tech. Rep. ATLAS-CONF-2016-037, CERN, Geneva, Aug, 2016.

[161] **ATLAS Collaboration** Collaboration, "Search for pair production of gluinos decaying via top or bottom squarks in events with b-jets and large missing transverse momentum in pp collisions at $\sqrt{s} = 13$ TeV with the ATLAS detector," Tech. Rep. ATLAS-CONF-2016-052, CERN, Geneva, Aug, 2016.

[162] **ATLAS Collaboration** Collaboration, "Search for squarks and gluinos in events with an isolated lepton, jets and missing transverse momentum at $\sqrt{s} = 13$ TeV with the ATLAS detector," Tech. Rep. ATLAS-CONF-2016-054, CERN, Geneva, Aug, 2016.

[163] **ATLAS Collaboration** Collaboration, "Further searches for squarks and gluinos in final states with jets and missing transverse momentum at $\sqrt{s}$ =13 TeV with the ATLAS detector," Tech. Rep. ATLAS-CONF-2016-078, CERN, Geneva, Aug, 2016.

[164] **CMS Collaboration** Collaboration, "Search for new physics in the all-hadronic final state with the MT2 variable," Tech. Rep. CMS-PAS-SUS-16-015, CERN, Geneva, 2016.

[165] **CMS Collaboration** Collaboration, "An inclusive search for new phenomena in final states with one or more jets and missing transverse momentum at 13 TeV with the AlphaT variable," Tech. Rep. CMS-PAS-SUS-16-016, CERN, Geneva, 2016.

[166] **CMS Collaboration** Collaboration, "Search for supersymmetry in the all-hadronic final state using top quark tagging in pp collisions at sqrt(s) = 13 TeV," Tech. Rep. CMS-PAS-SUS-16-030, CERN, Geneva, 2016.

[167] **ATLAS Collaboration** Collaboration, "Search for top squarks in final states with one isolated lepton, jets, and missing transverse momentum in $\sqrt{s} = 13$ TeV pp collisions with the ATLAS detector," Tech. Rep. ATLAS-CONF-2016-050, CERN, Geneva, Aug, 2016.

[168] **ATLAS Collaboration** Collaboration, "Search for the Supersymmetric Partner of the Top Quark in the Jets+Emiss Final State at sqrt(s) = 13 TeV," Tech. Rep. ATLAS-CONF-2016-077, CERN, Geneva, Aug, 2016.

[169] B. Allanach, A. Djouadi, J. Kneur, W. Porod, and P. Slavich, "Precise determination of the neutral Higgs boson masses in the MSSM," *JHEP* **0409** (2004) 044, `arXiv:hep-ph/0406166 [hep-ph]`.

[170] J. Pumplin, D. R. Stump, J. Huston, H. L. Lai, P. M. Nadolsky, and W. K. Tung, "New generation of parton distributions with uncertainties from global QCD analysis," *JHEP* **07** (2002) 012, `arXiv:hep-ph/0201195 [hep-ph]`.

[171] A. Buckley, J. Ferrando, S. Lloyd, K. Nordstrom, B. Page, M. Rufenacht, M. Schonherr, and G. Watt, "LHAPDF6: parton density access in the LHC precision era," *Eur. Phys. J.* **C75** (2015) 132, `arXiv:1412.7420 [hep-ph]`.

[172] S. Coleman and E. Weinberg, "Radiative corrections as the origin of spontaneous symmetry breaking," *Phys. Rev. D* **7** (Mar, 1973) 1888–1910.

[173] R. Casalbuoni, D. Dominici, F. Feruglio, and R. Gatto, "Tree Level Unitarity Violation for Large Scalar Mass in Multi - Higgs Extensions of the Standard Model," *Nucl. Phys.* **B299** (1988) 117–150.

[174] C. Wainwright, S. Profumo, and M. J. Ramsey-Musolf, "Gravity Waves from a Cosmological Phase Transition: Gauge Artifacts and Daisy Resummations," *Phys. Rev.* **D84** (2011) 023521, `arXiv:1104.5487 [hep-ph]`.

[175] L. Dolan and R. Jackiw, "Symmetry Behavior at Finite Temperature," *Phys. Rev.* **D9** (1974) 3320–3341.

[176] S. Weinberg, "Gauge and global symmetries at high temperature," *Phys. Rev. D* **9** (Jun, 1974) 3357–3378.

[177] D. J. Gross, R. D. Pisarski, and L. G. Yaffe, "Qcd and instantons at finite temperature," *Rev. Mod. Phys.* **53** (Jan, 1981) 43–80.

[178] P. Arnold and O. Espinosa, "Effective potential and first-order phase transitions: Beyond leading order," *Phys. Rev. D* **47** (Apr, 1993) 3546–3579.

[179] E. J. Weinberg and A. Wu, "Understanding complex perturbative effective potentials," *Phys. Rev. D* **36** (Oct, 1987) 2474–2480.

[180] G. C. Dorsch, S. J. Huber, K. Mimasu, and J. M. No, "Echoes of the Electroweak Phase Transition: Discovering a second Higgs doublet through $A_0 \to ZH_0$," *Phys. Rev. Lett.* **113** no. 21, (2014) 211802, `arXiv:1405.5537 [hep-ph]`.

[181] L. Fromme, S. J. Huber, and M. Seniuch, "Baryogenesis in the two-Higgs doublet model," *JHEP* **11** (2006) 038, arXiv:hep-ph/0605242 [hep-ph].

[182] J. E. Camargo-Molina, A. P. Morais, R. Pasechnik, M. O. P. Sampaio, and J. Wessén, "All one-loop scalar vertices in the effective potential approach," *JHEP* **08** (2016) 073, arXiv:1606.07069 [hep-ph].

[183] S. P. Martin, "Taming the Goldstone contributions to the effective potential," *Phys. Rev.* **D90** no. 1, (2014) 016013, arXiv:1406.2355 [hep-ph].

[184] J. Elias-Miro, J. R. Espinosa, and T. Konstandin, "Taming Infrared Divergences in the Effective Potential," *JHEP* **08** (2014) 034, arXiv:1406.2652 [hep-ph].

[185] J. A. Casas, J. R. Espinosa, M. Quiros, and A. Riotto, "The Lightest Higgs boson mass in the minimal supersymmetric standard model," *Nucl. Phys.* **B436** (1995) 3–29, arXiv:hep-ph/9407389 [hep-ph]. [Erratum: Nucl. Phys.B439,466(1995)].

[186] M. Krause, R. Lorenz, M. Muhlleitner, R. Santos, and H. Ziesche, "Gauge-independent Renormalization of the 2-Higgs-Doublet Model," *JHEP* **09** (2016) 143, arXiv:1605.04853 [hep-ph].

[187] M. Krause, M. Muhlleitner, R. Santos, and H. Ziesche, "2HDM Higgs-to-Higgs Decays at Next-to-Leading Order," arXiv:1609.04185 [hep-ph].

[188] R. Coimbra, M. O. P. Sampaio, and R. Santos, "ScannerS: Constraining the phase diagram of a complex scalar singlet at the LHC," *Eur. Phys. J.* **C73** (2013) 2428, arXiv:1301.2599 [hep-ph].

[189] P. M. Ferreira, R. Guedes, M. O. P. Sampaio, and R. Santos, "Wrong sign and symmetric limits and non-decoupling in 2HDMs," *JHEP* **12** (2014) 067, arXiv:1409.6723 [hep-ph].

[190] K. G. Klimenko, "On Necessary and Sufficient Conditions for Some Higgs Potentials to Be Bounded From Below," *Theor. Math. Phys.* **62** (1985) 58–65. [Teor. Mat. Fiz.62,87(1985)].

[191] I. F. Ginzburg and I. P. Ivanov, "Tree level unitarity constraints in the 2HDM with CP violation," arXiv:hep-ph/0312374 [hep-ph].

[192] A. Barroso, P. M. Ferreira, I. P. Ivanov, and R. Santos, "Metastability bounds on the two Higgs doublet model," *JHEP* **06** (2013) 045, arXiv:1303.5098 [hep-ph].

[193] M. E. Peskin and T. Takeuchi, "Estimation of oblique electroweak corrections," *Phys. Rev. D* **46** (Jul, 1992) 381–409.

[194] W. Grimus, L. Lavoura, O. M. Ogreid, and P. Osland, "The Oblique parameters in multi-Higgs-doublet models," *Nucl. Phys.* **B801** (2008) 81–96, arXiv:0802.4353 [hep-ph].

[195] W. Grimus, L. Lavoura, O. M. Ogreid, and P. Osland, "A Precision constraint on multi-Higgs-doublet models," *J. Phys.* **G35** (2008) 075001, arXiv:0711.4022 [hep-ph].

[196] **Gfitter Group** Collaboration, M. Baak, J. Cúth, J. Haller, A. Hoecker, R. Kogler, K. Monig, M. Schott, and J. Stelzer, "The global electroweak fit at NNLO and prospects for the LHC and ILC," *Eur. Phys. J.* **C74** (2014) 3046, arXiv:1407.3792 [hep-ph].

[197] H. E. Haber and H. E. Logan, "Radiative corrections to the Z b anti-b vertex and constraints on extended Higgs sectors," *Phys. Rev.* **D62** (2000) 015011, arXiv:hep-ph/9909335 [hep-ph].

[198] O. Deschamps, S. Descotes-Genon, S. Monteil, V. Niess, S. T'Jampens, and V. Tisserand, "The Two Higgs Doublet of Type II facing flavour physics data," *Phys. Rev.* **D82** (2010) 073012, arXiv:0907.5135 [hep-ph].

[199] F. Mahmoudi and O. Stal, "Flavor constraints on the two-Higgs-doublet model with general Yukawa couplings," *Phys. Rev.* **D81** (2010) 035016, arXiv:0907.1791 [hep-ph].

[200] T. Hermann, M. Misiak, and M. Steinhauser, "$\bar{B} \to X_s\gamma$ in the Two Higgs Doublet Model up to Next-to-Next-to-Leading Order in QCD," *JHEP* **11** (2012) 036, arXiv:1208.2788 [hep-ph].

[201] M. Misiak *et al.*, "Updated NNLO QCD predictions for the weak radiative B-meson decays," *Phys. Rev. Lett.* **114** no. 22, (2015) 221801, arXiv:1503.01789 [hep-ph].

[202] M. Misiak and M. Steinhauser, "Weak Radiative Decays of the B Meson and Bounds on $M_{H^\pm}$ in the Two-Higgs-Doublet Model," arXiv:1702.04571 [hep-ph].

[203] **LEP, DELPHI, OPAL, ALEPH, L3** Collaboration, G. Abbiendi *et al.*, "Search for Charged Higgs bosons: Combined Results Using LEP Data," *Eur. Phys. J.* **C73** (2013) 2463, arXiv:1301.6065 [hep-ex].

[204] **ATLAS** Collaboration, G. Aad *et al.*, "Search for charged Higgs bosons decaying via $H^\pm \to \tau^\pm\nu$ in fully hadronic final states using pp collision data at $\sqrt{s} = 8$ TeV with the ATLAS detector," *JHEP* **03** (2015) 088, arXiv:1412.6663 [hep-ex].

[205] **CMS** Collaboration, V. Khachatryan *et al.*, "Search for a charged Higgs boson in pp collisions at $\sqrt{s} = 8$ TeV," *JHEP* **11** (2015) 018, arXiv:1508.07774 [hep-ex].

[206] R. V. Harlander, S. Liebler, and H. Mantler, "SusHi: A program for the calculation of Higgs production in gluon fusion and bottom-quark annihilation in the Standard Model and the MSSM," *Comput. Phys. Commun.* **184** (2013) 1605–1617, arXiv:1212.3249 [hep-ph].

[207] **ATLAS, CMS** Collaboration, G. Aad *et al.*, "Measurements of the Higgs boson production and decay rates and constraints on its couplings from a combined ATLAS and CMS analysis of the LHC pp collision data at $\sqrt{s} = 7$ and 8 TeV," *JHEP* **08** (2016) 045, arXiv:1606.02266 [hep-ex].

[208] A. Denner, S. Dittmaier, M. Grazzini, R. V. Harlander, R. S. Thorne, M. Spira, and M. Steinhauser, "Standard Model input parameters for Higgs physics,". https://cds.cern.ch/record/2047636.

[209] **LHC Higgs Cross Section Working Group** Collaboration, S. Dittmaier *et al.*, "Handbook of LHC Higgs Cross Sections: 1. Inclusive Observables," arXiv:1101.0593 [hep-ph].

[210] P. M. Ferreira, J. F. Gunion, H. E. Haber, and R. Santos, "Probing wrong-sign Yukawa couplings at the LHC and a future linear collider," *Phys. Rev.* **D89** no. 11, (2014) 115003, arXiv:1403.4736 [hep-ph].

[211] D. Fontes, J. C. Romão, and J. P. Silva, "A reappraisal of the wrong-sign $hb\bar{b}$ coupling and the study of $h \to Z\gamma$," *Phys. Rev.* **D90** no. 1, (2014) 015021, arXiv:1406.6080 [hep-ph].

[212] M. Muhlleitner, M. O. P. Sampaio, R. Santos, and J. Wittbrodt, "The N2HDM under Theoretical and Experimental Scrutiny," *Journal of High Energy Physics* **2017** no. 3, (2017) 94, arXiv:1612.01309 [hep-ph].

Danksagung

An erster Stelle danke ich Prof. Dr. Milada Margarete Mühlleitner herzlich dafür, dass sie mir ermöglicht hat, diese spannenden Themen in meiner Promotion erforschen zu können und mich hierbei stets in allen Belangen voll unterstützt hat. Es war eine große Freude für mich, Teil ihrer Arbeitsgruppe zu sein.
Ich danke weiterhin PD Dr. Stefan Gieseke für das Korreferat und sein zu jeder Zeit offenes Ohr, falls ich Fragen hatte.
Ein herzliches Dankeschön an Philipp Basler, Eva Feigl, Margherita Ghezzi, Ramona Gröber, Marcel Krause, Mathieu Pellen, Michael Spira und Jonas Wittbrodt, mit denen ich während meiner Promotion zusammenarbeiten durfte. Für das Korrekturlesen dieser Arbeit danke ich Philipp Basler, Margherita Ghezzi, Robin Roth und Florian Staub.
Ich habe eine sehr schöne Zeit am ITP verbracht. An dem tollen Arbeitsklima hat nicht zuletzt das gesamte Kollegium, inklusive aller ehemaligen Kollegen, einen großen Anteil – vielen Dank hierfür. Dies gilt ganz besonders für meinen Zimmerkollegen Robin Roth, mit dem ich während der gesamten Promotion neben dem gemeinsamen Arbeitszimmer auch viele weitere Erfahrungen und Erlebnisse geteilt habe.
Für die finanzielle Unterstützung in den vergangenen drei Jahren danke ich der „Karlsruher Schule für Elementarteilchen- und Astroteilchenphysik: Wissenschaft und Technologie (KSETA)".

Mein größtes Dankeschön von Herzen an Lena und meine Familie für den stetigen Rückhalt und die Unterstützung!